

Università degli Studi di Bologna
Dipartimento di Chimica Fisica e Inorganica

Dottorato di Ricerca in Scienze Chimiche
XIX Ciclo

STUDI ESR DI SISTEMI COMPLESSI BASATI SU
CRISTALLI LIQUIDI

Tesi di Dottorato
Settore Scientifico Disciplinare CHIM02

Presentata da:
ILARIA VECCHI

Relatore:
Prof. CLAUDIO ZANNONI

Coordinatore:
Prof. VINCENZO BALZANI

Correlatori:
Prof. ALBERTO ARCIONI
Dr. CORRADO BACCHIOCCHI

2004–2006

Università degli Studi di Bologna
Dipartimento di Chimica Fisica e Inorganica

ESR STUDIES OF LIQUID CRYSTAL BASED
COMPLEX SYSTEMS

PhD Thesis of:
ILARIA VECCHI

Supervisor:
CLAUDIO ZANNONI

Thesis Coordinator:
Prof. VINCENZO BALZANI

Co-supervisors:
Prof. ALBERTO ARCIONI
Dr. CORRADO BACCHIOCCHI

2004–2006

Contents

Table of content	2
1 Introduction	3
1.1 Liquid Crystals	3
1.2 Order Parameter	8
2 Electron Spin Resonance Spectroscopy	11
2.1 Principles of Electron Spin Resonance	12
2.1.1 Zeeman Interaction	12
2.1.2 Hyperfine Coupling	14
2.1.3 Relaxation phenomena	16
2.1.4 Magnetic interactions in nitroxide radicals	18
2.2 Slow tumbling	21
2.2.1 Theory	21
2.2.2 Rotational modulation in isotropic liquids	25
2.2.3 Anisotropic liquids	27
2.2.4 Nitroxides	29
2.3 Spin Probe Technique	30
2.3.1 Experimental Spectra	30
2.3.2 Simulated Spectra	31
3 5CB LC doped with Azobenzene Derivatives	35
3.1 Azobenzene properties and applications	35
3.2 Photoisomerization in guest/host systems	38
3.3 <i>p</i> -substituted Azobenzene Derivatives	40
3.3.1 Experimental Section	40
3.3.2 Fitting Procedure for ESR Spectra	42
3.3.3 Results: T_{NI} , order and dynamics	44
3.3.4 Discussion	47
3.3.5 Conclusions	52
3.4 <i>p,p'</i> -disubstituted Azobenzene Derivatives	54
3.4.1 Results and Discussion: T_{NI} , order and dynamics	56
3.4.2 Conclusions	58

4 Filled Nematics	61
4.1 Aerosil properties and applications	61
4.2 Glass-like behavior	63
4.3 Hydrophobic and Hydrophilic Aerosil in 5CB	65
4.3.1 Experimental Section	65
4.3.2 Fitting Procedure for ESR Spectra	67
4.3.3 Results and Discussion: Order and Dynamics	70
4.3.4 Conclusions	78
5 Holographic Polymer-Dispersed LCs	81
5.1 Introduction to HPDLC	81
5.2 Experimental Section	82
5.2.1 HPDLC film preparation	82
5.2.2 ESR measurements of the HPDLC film	82
5.3 Fitting Procedure for ESR Spectra	84
5.4 Results: T_{NI} , order and dynamics	87
5.5 Conclusion	88
Appendix	89
A Euler Angles	89
B Synthesis of 4-<i>Ot</i>-Bu-phenylazobenzene	91
List of Figures	97
List of Tables	99
Bibliography	106

Chapter 1

Introduction

1.1 Liquid Crystals

Liquid crystals are a thermodynamic stable phase of matter with properties intermediate between that of a liquid and that of a crystal. In particular, they are characterized by the anisotropy of electrical, optical and mechanical properties, like the crystalline solids, without the existence of a three-dimensional crystal lattice, like the isotropic liquids [1–3]. Crystalline solids have positional and orientational order, while conventional liquids have neither. A liquid crystal (LC), on the other hand, might have no positional order, but some orientational order. A given molecule's orientation is not constant, and all the LC molecules, called mesogens, do not point in exactly the same direction, meaning that although there is an average order, the mesogens are constantly flowing and moving, changing position and orientation. The orientational order gives, however, different optical, dielectric, magnetic and mechanical properties in different directions, i.e. the material is anisotropic.

Depending upon the molecular organization, in terms of positional and orientational order of the LC molecules, one can distinguish the various liquid crystal phases.

1. Nematic phase

Nematic LC have long-range orientational order but no long-range positional order. The mesogens tend, on average, to orient along a preferred direction, called director, essentially expressing the molecular anisotropy as a phase anisotropy. Figure 1.1 shows conceptually what the molecular organization of a nematic LC is like: the mesogens, schematically represented as ellipsoids reflecting their typical rod-like shape, point vertically along the director (\mathbf{n}) but are arranged with no particular order.

2. Smectic phase

Smectic phases have orientational order and some degree of positional order. They are distinguished by a layered structure which is periodic in one dimension. On the basis of the molecular organization within each layer, we can identify families of smectics with different structures. In the smectic A phase, the mesogen preferred direction is on average perpendicular to the layer and

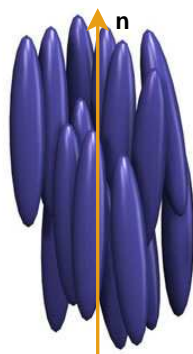


Figure 1.1: Molecular organization of a nematic liquid crystal. The mesogens molecules are on average parallel one to each other and they tend to align with respect to a preferred direction (\mathbf{n}), called the director.

there is no positional order in the plane itself (Figure 1.2 (a)); smectic B phases are characterized by an additional hexagonal order within the layers; the smectic C (Figure 1.2 (b)) phase corresponds to a tilted version of smectic A, with the director forming an angle, called the tilt angle, with respect to the layer normal.

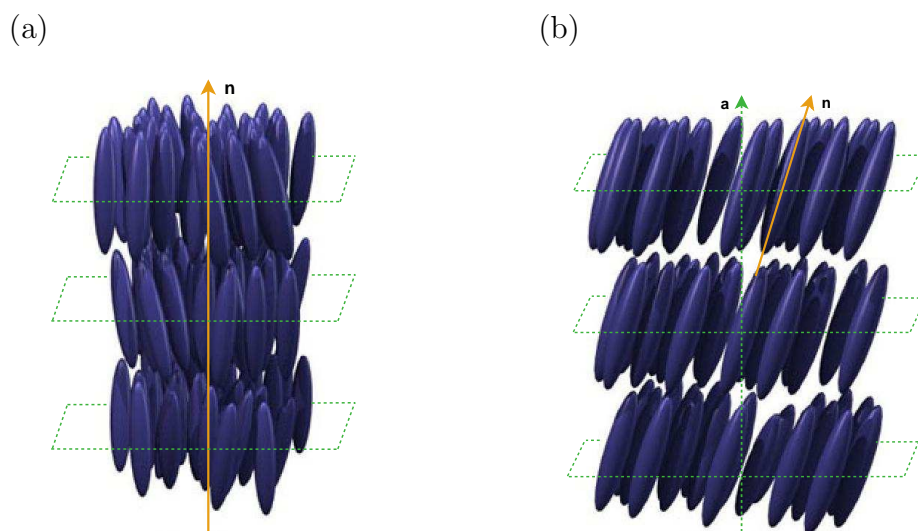


Figure 1.2: Molecular organization of (a) smectic A phase with every layer lying perpendicular to the director (\mathbf{n}) and (b) smectic C phase with the director (\mathbf{n}) tilted with respect to the layer normal (\mathbf{a}).

3. Cholesteric phase

Chiral liquid crystal molecules lead to chiral phases in which the director twists as it progresses through the phase. The chiral nematic phase is also called the cholesteric phase, since it was first discovered in cholesterols. The structure

of a cholesteric phase is shown in Figure 1.3 (a), where the different nematic layers have been coloured differently so as to differentiate them. The twisting of the nematic director from layer to layer is clearly shown in Figure 1.3 (b).

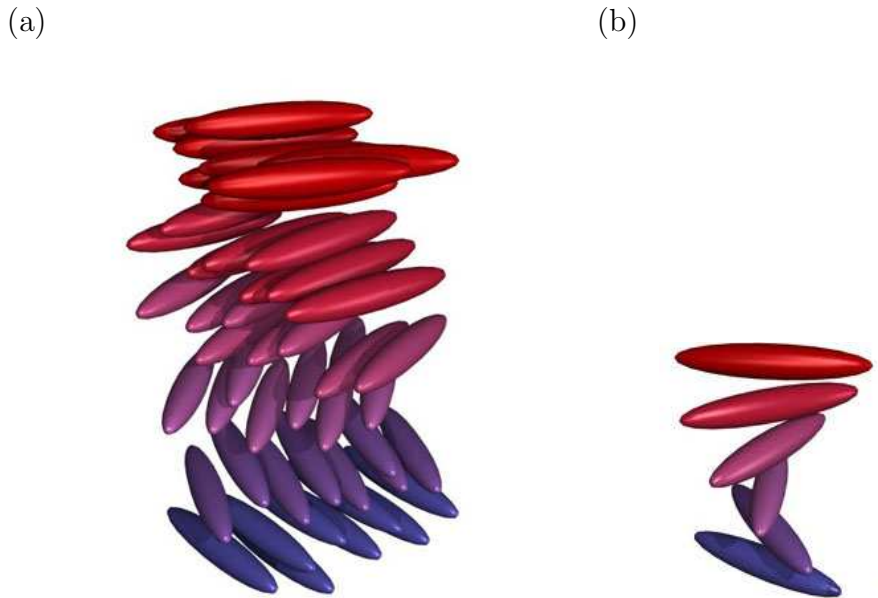


Figure 1.3: (a) Molecular organization of a cholesteric phase and (b) the chiral twisting of the director.

The liquid crystal phases generally lie in the temperature range between the solid and isotropic liquid phase, hence the term mesophases. Furthermore, LCs come in two basic classifications:

1. Thermotropics

The phase transitions of thermotropic LCs depend on the temperature. As shown in Figure 1.4 (a), by heating a crystalline solid, a liquid crystal phase can be obtained at the melting point. Many thermotropic LCs exhibit a variety of phases as temperature is changed. For instance, a particular mesogen may exhibit various smectic and nematic phases as temperature is increased. Finally, at even higher temperature, the thermal motion destroys the ordering of the LC phase leading to an isotropic liquid phase.

2. Lyotropics

These mesophases can be obtained by mixing various components (usually amphiphilic molecules and water) in a suitable concentration range, therefore the phase transformation depends on temperature as well as composition.

The molecules that can make up lyotropic phases are surfactants consisting of a polar head, often ionic, and a nonpolar tail, often hydrocarbon. To better understand how the molecular organization changes as the temperature

and the concentration are varied, let us consider the generic phase diagram reported in Figure 1.4 (b). At low concentration the surfactant is randomly distributed throughout the solvent, while as the concentration increases the molecules take on different arrangements or phases. They first begin to arrange themselves in hollow spheres, rods, and disks called micelles. Increasing the surfactant concentration, the micelles tend, in turn, to arrange themselves into loose patterns: rod-shaped micelles often give rise to hexagonal arrays made out of six rods grouped around a central one (hexagonal LC). At even higher concentrations the molecules move into another liquid crystalline phase, the lyotropic LC bilayer.

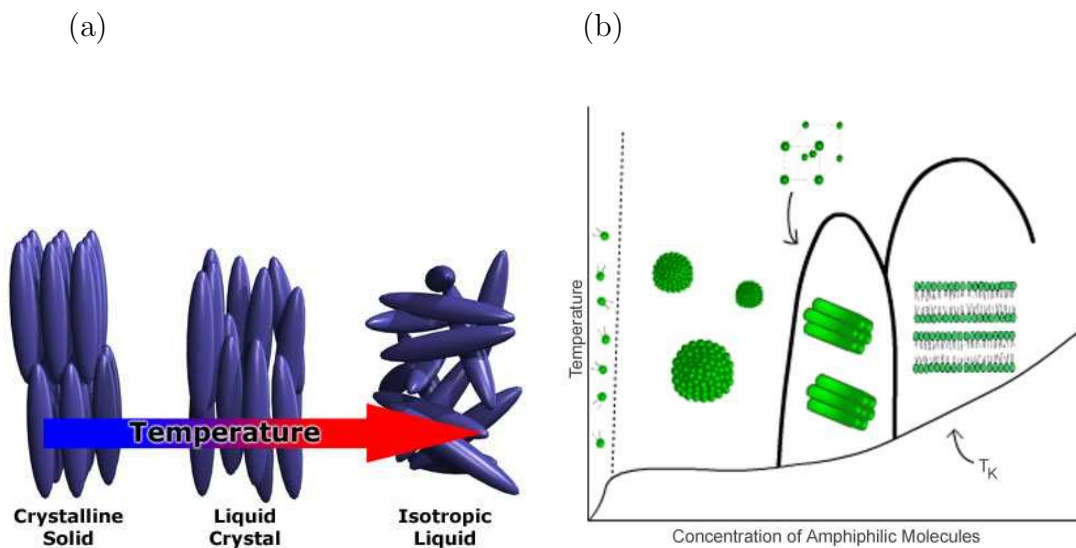


Figure 1.4: Phase transitions of (a) thermotropic and (b) lyotropic liquid crystals.

Liquid crystals (LCs) are unique materials that show such characteristic properties as a self-organizing nature, fluidity with long-range order, cooperative motion, anisotropy in various physical properties (optical, electrical and magnetic) and alignment change due to external fields at surfaces and interfaces. Because of their peculiar properties, LCs are nowadays successfully used in many technological applications.

The nematics find wide use in displays. In a typical device, a "twisted nematic cell" (Figure 1.5), a thin film of a LC mixture, which is twisted through 90° , is contained between two glass plates. Polarization filters are applied on the exteriors of the plates. Inside the plates are color filters, transparent electrodes, and orientation layers to produce the twist. With no voltage applied and the polarizers attached with their polarization axes mutually perpendicular, the cell appears bright: the twisted phase reorients the light that has passed through the first polarizer, allowing it to be transmitted through the second polarizer and reflected back to the observer. If a voltage, slightly greater than the threshold value, is applied, the twisted structure

of the liquid crystal molecules will be destroyed since they will turn perpendicularly to the glass plates. In this aligned state, the mesogens do not reorient light, so the light polarized at the first polarizer is absorbed at the second polarizer, and the entire device appears dark. In this way, the electric field can be used to make a pixel switch between clear or dark on command and an image is formed on the display. Since very little current flows in these cells, this type of display is extremely energy-efficient.

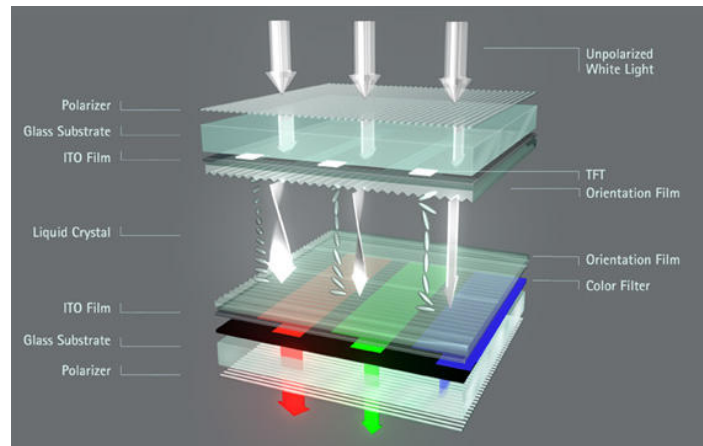


Figure 1.5: Example of technological application in the field of liquid crystals: scheme of a twisted nematic cell.

Thermotropic chiral LCs whose pitch (Figure 1.3 (b)) varies strongly with temperature can be used as thermometers, as shown in Figure 1.6, since the color of the material will change as the pitch is changed.

Other liquid crystal materials change color when stretched or stressed. Thus, liquid crystal sheets are often used in industry to look for hot spots, map heat flow, measure stress distribution patterns, and so on. In the next future it is expected that LCs could be used in microelectronics (organic transistors, molecular electric cables, optical computers), nonlinear optics (wave guides) and eventually decorative and visual arts.



Figure 1.6: Example of technological application in the field of liquid crystals: picture of a cholesteric thermoeter.

1.2 Order Parameter

As previously mentioned, the anisotropy observed in the properties of LC materials is due to the arrangement of the mesogens, in other words to the orientational order. While in Section 1.1 the qualitative description of the order in the various mesophases has been given, here the quantitative analysis of the orientational order, through the definition of the order parameter, is presented.

The probability of finding a mesogen at a particular orientation ω with respect to the director \mathbf{n} can be described through the Euler angles α, β, γ (see Appendix A) [4]:

$$P(\omega) = P(\alpha, \beta, \gamma) \quad (1.1)$$

If we restrict our discussion to mesogens having rod-like shape, then the probability $P(\omega)$ depends only on α and β angles:

$$P(\omega) = P(\alpha, \beta)/2\pi \quad (1.2)$$

Let us assume the Z axis of the laboratory frame is parallel to the director \mathbf{n} , then:

$$P(\omega) = P(\beta)/2\pi \quad (1.3)$$

In addition, for uniaxial phases:

$$P(\beta) = P(\pi - \beta) \quad (1.4)$$

The distribution function which describes the angular orientation of the LC molecules is generally unknown, but it can be approximated by a series expansion whose basis set functions are the Legendre polynomials $P_L(\cos\beta)$:

$$\begin{aligned} P_1(\cos\beta) &= \cos\beta \\ P_2(\cos\beta) &= \frac{3}{2}\cos^2\beta - \frac{1}{2} \\ P_3(\cos\beta) &= \frac{5}{2}\cos^3\beta - \frac{3}{2}\cos\beta \\ P_4(\cos\beta) &= \frac{35}{8}\cos^4\beta - \frac{30}{8}\cos^2\beta + \frac{3}{8} \\ P_5(\cos\beta) &= \frac{63}{8}\cos^5\beta - \frac{70}{8}\cos^3\beta + \frac{15}{8}\cos\beta \end{aligned} \quad (1.5)$$

$P(\beta)$ then becomes:

$$P(\beta) = \sum_{L=0}^{\infty} p_L P_L(\cos\beta) \quad L = \text{even} \quad (1.6)$$

The J th term of the expansion can be found if each term of Eq. 1.6 is multiplied by $P_J(\cos\beta)$ and then integrated:

$$\int_0^\pi d\beta \sin\beta P(\beta) P_J(\cos\beta) = \langle P_J \rangle = \int_0^\pi d\beta \sin\beta \sum_{L=0}^{\infty} p_L P_L(\cos\beta) P_J(\cos\beta) \quad (1.7)$$

$$\langle P_J \rangle = p_J \frac{2}{(2J+1)} \quad (1.8)$$

The distribution function then becomes:

$$P(\beta) = \frac{1}{2} + \frac{5}{2} \langle P_2 \rangle P_2(\cos\beta) + \frac{9}{2} \langle P_4 \rangle P_4(\cos\beta) + \dots \quad (1.9)$$

When dealing with the orientational order of a mesophase, this distribution is often truncated at the second term of the expansion and $\langle P_2 \rangle$ represents the orientational order parameter:

$$\langle P_2 \rangle = \int_0^\pi d\beta \sin\beta P(\beta) P_2(\cos\beta) = \frac{3}{2} \langle \cos^2\beta \rangle - \frac{1}{2} \quad (1.10)$$

This parameter clearly expresses the order of the mesogens with respect to the director, being β the angle between the mesogen molecule axis and the local director \mathbf{n} . If the molecules are perfectly aligned along the director, then $\langle P_2 \rangle = 1$, whereas if the mesogens are randomly oriented, then $\langle P_2 \rangle = 0$. For a typical liquid crystal sample, $\langle P_2 \rangle$ is on the order of 0.3 to 0.8 and generally decreases as the temperature is raised. In particular, a sharp drop of the order parameter to zero is observed when the phase transition from an LC phase into the isotropic phase takes place.

The order parameter can be measured experimentally in a number of ways. For instance, diamagnetism, birefringence, Raman scattering, and NMR can also be used to determine $\langle P_2 \rangle$.

Chapter 2

Electron Spin Resonance Spectroscopy

This chapter is focused on the Electron Spin Resonance (ESR), with the aim of giving an introduction to the basic theory of ESR spectroscopy and understanding how this technique can provide information, on a microscopic scale, about the molecular arrangement and the dynamical state of LC systems.

ESR is a spectroscopic technique that detects species having unpaired electrons [5–7]. Its contribution has been determinant in clarifying the structures of free radicals, paramagnetic metal complexes and molecules in excited triplet states. In a continuous search of new applications, it has proven to be a powerful tool in investigations such as the kinetics of radical reactions [8], polymerization mechanisms [9], energy transfer in molecular crystals [10], conformational changes in biological systems [11, 12] and liquid crystal structures [7, 13].

Even if the occurrence of paramagnetism is relatively low, the ESR spectroscopy can be however applied to diamagnetic systems, like biological systems and LCs, by using the so called spin probe technique [14], i.e. introducing into the sample a versatile probe having a free radical center.

The spin probe technique allows obtaining information relative to the probe environment. The spectral features (resonance frequency, multiplet splittings and line shapes) are, in fact, extremely sensitive to several aspects of the probe physico-chemical environment. Obviously, in order to properly report the changes in its environment, the paramagnetic probe must satisfy a series of requirements:

1. An ideal spin probe is a stable free radical, e.g. paramagnetic transition metal ion or organic nitroxide radical
2. The physical properties of the reporter group that are detected must be either unique or distinct from the properties of the system under investigation
3. The system suffer little or better no perturbation in its structure as a result of the incorporation of the probe

In this study the spin probe technique has been used to investigate the properties of different LC matrices. In particular, from the analysis of the spectral profiles,

which requires sophisticated theoretical techniques (see Section 2.2), information relative to the phase transition temperatures, the orientational order and the mobility of the mesogens has been obtained.

2.1 Principles of Electron Spin Resonance

In the following, the main interactions occurring in a paramagnetic system are described and their role in determining the ESR spectra features is discussed.

2.1.1 Zeeman Interaction

ESR spectroscopy deals with the transitions induced between the Zeeman levels of a paramagnetic system in a magnetic field [5–7]. An atom or molecule possess a permanent magnetic dipole moment $\boldsymbol{\mu}$ only if it has nonzero electronic angular momentum \mathbf{J}

$$\boldsymbol{\mu} = -g\beta_e \mathbf{J} \quad (2.1)$$

where g is the spectroscopic splitting factor and β_e is the Bohr magneton, $|e|\hbar/2mc$. The contribution to the angular momentum \mathbf{J} comes from the spin angular momentum \mathbf{S} as well as the orbital angular momentum \mathbf{L} . In most cases, however, the contribution relative to the orbital angular momentum can be neglected [6] because the magnetic properties are essentially due to the spin angular momentum \mathbf{S} . Thus the Eq. 2.1 turns into

$$\boldsymbol{\mu} = -g\beta_e \mathbf{S} \quad (2.2)$$

The Zeeman interaction energy of the magnetic moment with an external magnetic field \mathbf{H} of uniform intensity H_0 , $\mathbf{H} = (0, 0, H_0)$, is described by the following Hamiltonian

$$\mathcal{H}_z = -\boldsymbol{\mu} \cdot \mathbf{H} = g\beta_e \mathbf{S} \cdot \mathbf{H} = g\beta_e S_z H_0 \quad (2.3)$$

where S_z is the operator corresponding to the projection of \mathbf{S} along the magnetic field direction. The expectation values of S_z , denoted with m_S , range between $-S$ and $+S$ by integer steps, therefore the effect of the magnetic field is to produce $2S + 1$ levels, each with energy

$$E_{m_S} = g\beta_e m_S H_0 \quad (2.4)$$

and a population given by the Boltzmann distribution law

$$P_{m_S} = \frac{\exp(-E_{m_S}/kT)}{\sum_{m_S} \exp(-E_{m_S}/kT)} \quad (2.5)$$

Let us concentrate mainly on species having only an unpaired electron, because this kind of system is normally used in the spin probe technique in which we are interested in. For a system with only an unpaired electron $S = 1/2$ and two energy

levels, with $m_S = -1/2, 1/2$, are allowable. As shown in Figure 2.1, these levels are degenerate when no magnetic field is applied, otherwise they are split and the energy difference between the two levels is proportional to the magnetic field intensity

$$\Delta E = E_{1/2} - E_{-1/2} = g\beta_e H_0 \quad (2.6)$$

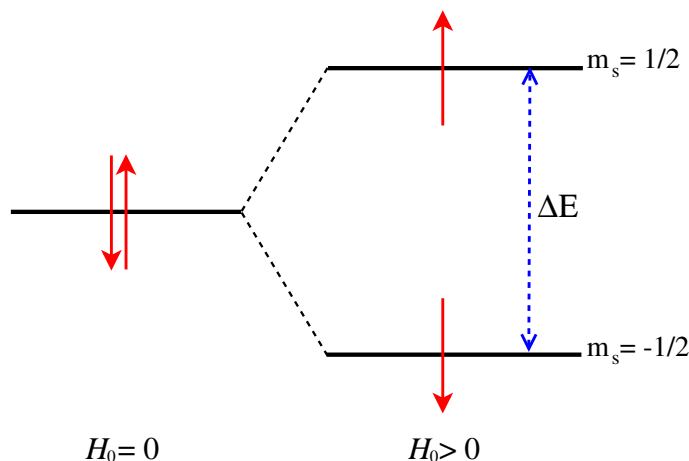


Figure 2.1: Zeeman splitting of an $S = 1/2$ state.

Transitions can occur between the two levels if the sample is irradiated with an electromagnetic field of proper frequency ν that matches the energy gap ΔE between the levels. The resonance condition leading to energy absorption from the sample is the met when

$$h\nu = \Delta E = g\beta_e H_0 \quad (2.7)$$

ESR experiments are usually carried out at a fixed frequency ν_0 and the resonance condition is found by varying the intensity of the magnetic field H

$$H = h\nu_0/g\beta_e \quad (2.8)$$

In this simplified theoretical treatment, we have considered the splitting factor g as an effective factor of the system, i. e. as a scalar parameter. Actually, the g factor of a molecule must be represented by a second rank tensor. This implies that the Zeeman Hamiltonian should be correctly written as

$$\mathcal{H}_z = \beta_e \mathbf{H} \cdot \mathbf{g} \cdot \mathbf{S} \quad (2.9)$$

The physical observable corresponding to \mathcal{H}_z is the energy. Since the energy does not depend on the orientation of the reference frame, it follows that its choice is arbitrary. In this regard, one of the most convenient possibilities is to consider the magnetic frame (x', y', z') , where the g tensor is diagonal. The Zeeman Hamiltonian, then, becomes

$$\mathcal{H}_z = \beta_e (H_{x'} g_{x'x'} S_{x'} + H_{y'} g_{y'y'} S_{y'} + H_{z'} g_{z'z'} S_{z'}) \quad (2.10)$$

where $H_{x'}$, $H_{y'}$, $H_{z'}$ are the components of \mathbf{H} in the molecular axis systems.

If a molecule is oriented with one of the principal axes parallel to the field direction, then the resonance condition will be met at the field values

$$h\nu_0/\beta_e g_{x'x'} \quad h\nu_0/\beta_e g_{y'y'} \quad h\nu_0/\beta_e g_{z'z'} \quad (2.11)$$

depending on which axis is directed along the field. For an arbitrary orientation, the resonance condition is given by Eq. 2.8, where

$$g = \sqrt{(g_{x'x'}^2 l^2 + g_{y'y'}^2 m^2 + g_{z'z'}^2 n^2)} \quad (2.12)$$

with (l, m, n) being the director cosines of \mathbf{H} in the molecular axis system.

Due to the anisotropy of the \mathbf{g} tensor, the resonance condition fall at different field values, depending on the molecular orientation.

2.1.2 Hyperfine Coupling

Up to this point only the interaction between an electron spin with an external magnetic field has been considered. What is more interesting in an ESR experiment is the further interaction between the electron spin and the internal magnetic fields, particularly those due to the magnetism of nuclei in the same molecule possessing nonvanishing nuclear spin angular momentum \mathbf{I} . The magnetic interactions between electron and nuclear spins cause the ESR spectrum to consist of a number of lines rather than a single line. The arrangement of the resulting multiplet structures is called hyperfine structure.

The magnetic interactions between electron and nuclear spins are represented by the Hamiltonian

$$\mathcal{H}_{hc} = -g\beta_e g_N \beta_N \left\{ \frac{(\mathbf{I} \cdot \mathbf{S})r^2 - 3(\mathbf{I} \cdot \mathbf{r})(\mathbf{S} \cdot \mathbf{r})}{r^5} - \frac{8\pi}{3}(\mathbf{I} \cdot \mathbf{S}) \delta(\mathbf{r}) \right\} \quad (2.13)$$

where \mathbf{r} is the electron-nucleus distance vector, $\delta(\mathbf{r})$ is the Dirac delta function, g_N and β_N are the nucleus splitting factor and magneton, respectively.

The first term in Eq. 2.13 represents the electron-nucleus dipolar interaction and can be rewritten as

$$\mathcal{H}_1 = \mathbf{I} \cdot \mathbf{A}' \cdot \mathbf{S} \quad (2.14)$$

\mathbf{A}' is a second-rank tensor, therefore the magnitude of the dipolar interaction depends on the molecular orientation with respect to the field direction. The elements of this tensor are given by

$$A'_{ij} = -g\beta_e g_N \beta_N \langle (r^2 \delta_{ij} - 3x_i x_j) r^{-5} \rangle \quad (2.15)$$

and the brackets denotes the integration over the electron distribution.

The second terms in Eq. 2.13 describes the Fermi contact coupling, i. e. the interaction between the magnetic moment of the nuclear spin and the electron spin density at the nucleus, and it is also indicated as

$$\mathcal{H}_2 = a \mathbf{I} \cdot \mathbf{S} \quad (2.16)$$

where the a is the isotropic scalar coupling constant

$$a = \frac{8\pi}{3} g\beta_e g_N \beta_N \psi^2(0) \quad (2.17)$$

with $\psi^2(0)$ indicating the probability of finding the electron at the nucleus.

Eq. 2.14 combined with Eq. 2.16 leads to the complete hyperfine Hamiltonian, written in the compact form

$$\mathcal{H}_{hc} = \mathbf{I} \cdot \mathbf{A} \cdot \mathbf{S} \quad (2.18)$$

where \mathbf{A} is the hyperfine tensor with components

$$A_{ij} = A'_{ij} + \delta_{ij}a \quad (2.19)$$

The complete spin Hamiltonian, which takes into account both the Zeeman and the hyperfine interaction, is then expressed as

$$\mathcal{H} = \mathcal{H}_z + \mathcal{H}_{hc} = \beta_e \mathbf{H} \cdot \mathbf{g} \cdot \mathbf{S} + \mathbf{I} \cdot \mathbf{A} \cdot \mathbf{S} \quad (2.20)$$

The effect of the interaction between the electron and nuclear spins is the splitting of the Zeeman levels: the electron spin moment \mathbf{S} , interacting with the nucleus, “feels” a different total field according to which of the $2I + 1$ allowable orientations is assumed by the nuclear spin in the static magnetic field. The energy of the hyperfine levels is then

$$E_{m_S, m_I} = g\beta_e m_S H_0 + A m_S m_I \quad (2.21)$$

where m_I is the expectation value of I which ranges between $-I$ and I by integer steps, g is given in Eq. 2.12 and A is similarly defined as

$$A^2 = A_{x'x'}^2 l^2 + A_{y'y'}^2 m^2 + A_{z'z'}^2 n^2 \quad (2.22)$$

Due to the effect of the hyperfine couplings, a number of sublevels are generated and the electromagnetic field used in the ESR experiment can induce transitions among the sublevels. However, not all the transitions are allowed: the selection rules $\Delta m_S = \pm 1$ and $\Delta m_I = 0$ must be satisfied. The resonance condition is therefore met when

$$h\nu_0 = \Delta E_{m_I} = g\beta_e H + A m_I \quad (2.23)$$

and, because of the anisotropy of the \mathbf{g} and \mathbf{A} tensors, it will depend on the molecular orientation with respect to the magnetic field direction. It is important to note that, when the paramagnetic species is dissolved in low-viscosity solvent, the fast

molecular reorientation due to the thermal motions average out the anisotropic terms of the Hamiltonian in Eq. 2.20 which, in this case, turns into

$$\mathcal{H} = g\beta_e \mathbf{H} \cdot \mathbf{S} + a \mathbf{I} \cdot \mathbf{S} \quad (2.24)$$

where

$$g = \frac{1}{3} \text{Tr}(\mathbf{g}) \quad a = \frac{1}{3} \text{Tr}(\mathbf{A}) \quad (2.25)$$

and Eq. 2.23 then becomes

$$h\nu_0 = \Delta E_{m_I} = g\beta_e H + am_I \quad (2.26)$$

2.1.3 Relaxation phenomena

The discussion above seems to imply that ESR absorptions occur at a precise value of the magnetic field applied and the resulting ESR lines are infinitely narrow. Actually, a relevant parameter in the characterization of the ESR spectrum shape is the linewidth of the absorption bands. To fully understand this aspect, it is necessary to deepen the ESR absorption-relaxation process.

ESR experiments are usually carried out at a fixed frequency and the resonance condition is found by varying the intensity of the magnetic field. Most ESR spectrometers operate with microwave fields at 9.5 GHz (X band) or 35 GHz (Q band) and the magnetic fields in these cases are about 3400 and 12500 G, respectively. The magnetic energy is $0.3\text{--}1 \text{ cm}^{-1}$, i.e. some hundred times smaller than kT at ordinary temperatures, so the difference in population of the Zeeman levels (see Eq. 2.5) is very minute. However this population difference is responsible for the detection of the ESR signal. In fact, when a sample is irradiated, it absorbs energy and therefore it is excited to higher levels. At the same time, the inverse transition occurs by stimulated emission but, since the rates of both processes are proportional to the population of the level, a net energy absorption results. Two relaxation processes avoid that the prevailing absorption leads to an equal population of the Zeeman levels, bringing back the system to the Boltzmann equilibrium:

1. Spin-lattice relaxation

Nonradiative transitions from the higher to the lower energy states restore the equilibrium, with the consequent transfer of energy to the environment, dissipated as thermal energy. The rate at which thermal equilibrium is restored is defined by a characteristic time called the spin-lattice relaxation time T_1 . This process can be described by a single exponential decay

$$\frac{dM_z}{dt} = -\frac{M_z - M_{eq}}{T_1} \quad (2.27)$$

where M_z is the macroscopic magnetization of the sample and M_{eq} is given by the Curie law

$$M_{eq} = Ng_e^2\beta_e^2S(S+1)H_0/3kT \quad (2.28)$$

where N is the number of spins, g_e is the free spin g value and T is the absolute temperature. The spin-lattice relaxation shortens the lifetime of the magnetic levels and, therefore, a broadening of the spectral lines can occur. According to the Heisenberg uncertainty principle, if the system maintains a particular state not longer than a time Δt , the uncertainty in the energy of the state can not be less than $h/\Delta t$. In other words, the spectral linewidth, in frequency units, is at least of the order of $1/T_1$.

2. Transverse time relaxation

Under condition of low microwave power, thus avoiding saturation effects, the linewidths are usually due to relaxation mechanisms which produce a modulation of the magnetic levels without causing transitions between them. This process, in contrast with the spin-lattice relaxation, keeps constant the total Zeeman energy and is characterized by a relaxation time T_2 , called transverse relaxation time. The perpendicular component of the magnetization, which in absence of relaxation would follow the oscillating microwave field, decays toward zero according to

$$\frac{dM_x}{dt} = -\frac{M_x}{T_2} \quad (2.29)$$

The relaxation time produces an absorption curve that is described by a Lorentzian function

$$f(H) = \frac{T_2}{\pi} \frac{1}{1 + T_2^2(H - H_0)^2} \quad (2.30)$$

Experimentally, T_2 may be obtained from the width of the curve at half height, which is $2/T_2$ (Figure 2.2). Actually, in the common ESR spectrometers a 100 kHz field modulation is used and this causes the displayed curve to be the derivative of the absorption curve (Figure 2.2). If the peak-to-peak distance of the derivative curve, corresponding to the width of the absorption curve at the points of maximum slope, is δ , then

$$\frac{1}{T_2} = \frac{\sqrt{3}}{2} \delta \quad (2.31)$$

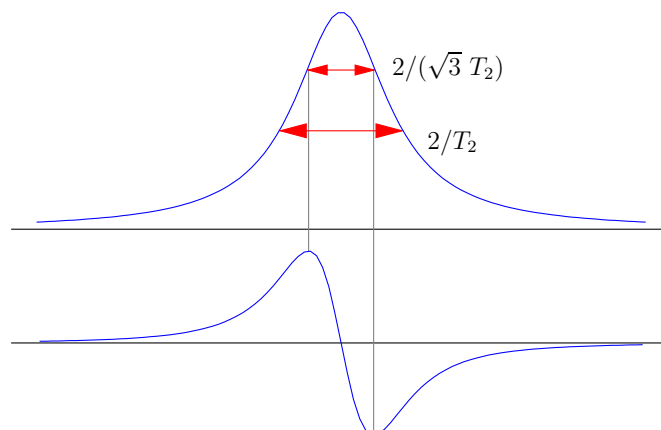


Figure 2.2: Plot of a Lorentzian curve and of its first derivative.

2.1.4 Magnetic interactions in nitroxide radicals

In order to clarify the role of the magnetic interactions, discussed in Sections 2.1.1 and 2.1.2, in determining the ESR spectrum shape, let us consider, as example, the nitroxide free radicals which are a class of molecules widely used as spin probes in ESR study [15–19]. These species, containing the moiety shown in Figure 2.3, are remarkably stable and inert because of the protective effect exerted by the four methyl groups.

For the nitroxide radicals, $S = 1/2$ and $I = 1$, thus there are two Zeeman levels, with $m_S = -1/2, 1/2$, each split into three sublevels with $m_I = -1, 0, 1$. The resulting energy level scheme in a static magnetic field is shown in Figure 2.4 together with the allowed ESR transitions ($\Delta m_S = \pm 1$ and $\Delta m_I = 0$).

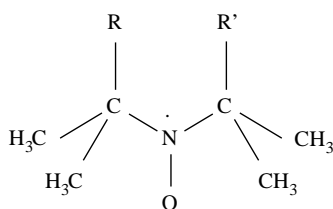


Figure 2.3: Chemical structure of a generic nitroxide free radical.

As mentioned in Section 2.1.3, in a typical ESR experiment the sample is irradiated with a fixed frequency ν_0 , while the intensity of the magnetic field H is varied. It follows that the energy gap between the Zeeman levels changes accordingly to the magnetic field intensity. For a nitroxide, the dependence of the energy levels on the field strength is shown in Figure 2.5. When the resonance condition (Eq. 2.23) is satisfied, the allowed transitions give rise to a three line spectrum (Figure 2.5).

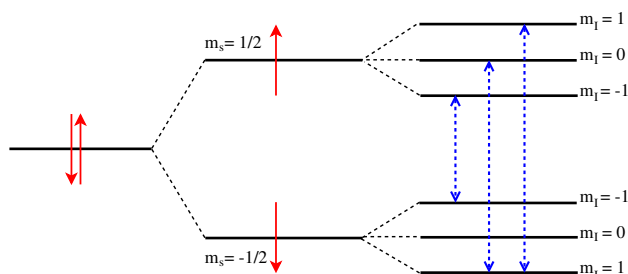


Figure 2.4: Energy level scheme for a nitroxide radical. The Zeeman splitting and the corresponding hyperfine levels are displayed together with the three allowed ESR transitions (dashed blue arrows).

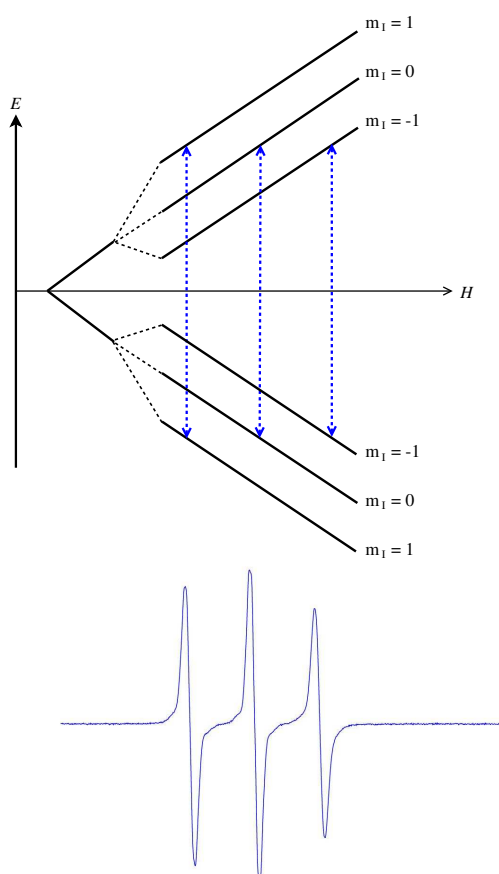


Figure 2.5: Dependence of the energy levels on the field strength for a nitroxide. The allowed transitions, indicated with blue arrows, give rise to a three line ESR spectrum.

Let us examine how the ESR spectral features are affected by the paramagnetic molecule orientation relative to the magnetic field direction. Figure 2.6 shows a series of spectra, obtained in different conditions, relative to a nitroxide spin probe whose magnetic parameters are listed in Table 2.1.

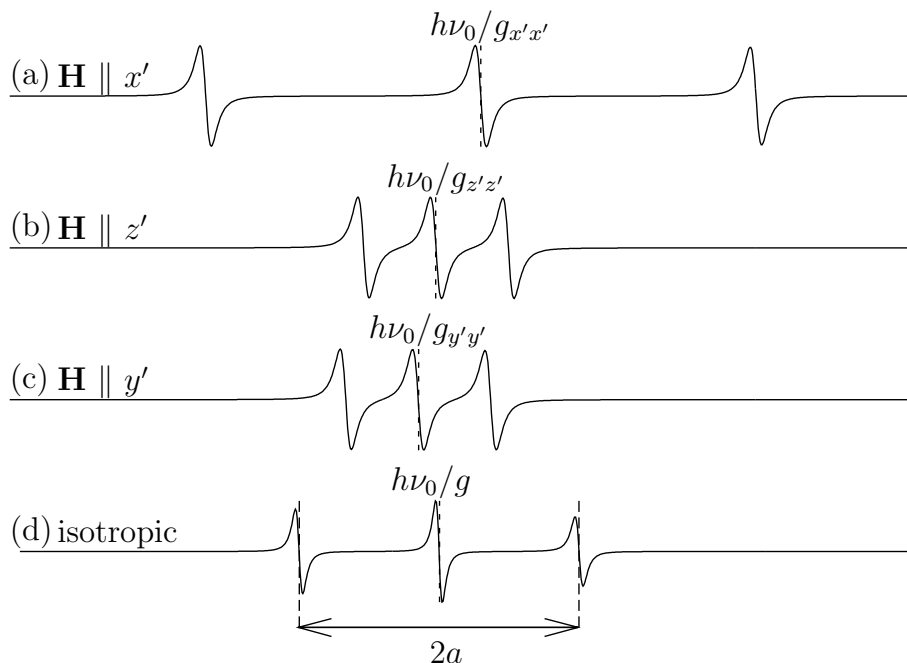


Figure 2.6: Angular dependence of the ESR spectrum features.

Spectra (a), (b) and (c) refer to probe molecules oriented in a crystal lattice, with the magnetic field parallel to each of the three principal directions of the magnetic tensors. Spectrum (d) refers to an isotropic solution, i.e. to a sample in which the spin probe is randomly oriented. Due to the g -factor anisotropy and depending on the molecular orientation, the centers of the spectra fall at different field values, according to Eq. 2.11. The three lines are symmetrically disposed about the center of the spectrum and they are equally spaced with a separation in field units of $A/g\beta_e$ or $a/g\beta_e$ for oriented or non-oriented molecules, respectively.

	g_{ij}	A_{ij} / G	a / G
$g_{x'x'}$	2.0027	$A_{x'x'}$ 30.8	a 14.13
$g_{y'y'}$	2.0088	$A_{y'y'}$ 5.8	
$g_{z'z'}$	2.0061	$A_{z'z'}$ 5.8	

Table 2.1: Magnetic parameters for a nitroxide free radical.

2.2 Slow tumbling

The complete Hamiltonian describing the magnetic interactions occurring in a paramagnetic system exposed to a static magnetic field can be considered as the sum of two contributions: an isotropic, orientationally invariant part \mathcal{H}_0

$$\mathcal{H}_0 = g\beta_e \mathbf{H} \cdot \mathbf{S} + a \mathbf{S} \cdot \mathbf{I} \quad (2.32)$$

and a purely anisotropic, angular dependent part \mathcal{H}_1

$$\mathcal{H}_1 = \beta_e \mathbf{H} \cdot \mathbf{g}' \cdot \mathbf{S} + \mathbf{S} \cdot \mathbf{A}' \cdot \mathbf{I} \quad (2.33)$$

where \mathbf{g}' and \mathbf{A}' are traceless tensors.

In a liquid phase, the molecular tumbling makes \mathcal{H}_1 a random function of time. As a consequence there is a random modulation of the energy levels and of the transition frequencies. In spite of the vanishing value of \mathcal{H}_1 , broadening of the absorption lines is expected to occur. The frequency fluctuations can be characterized through their amplitude and coherence. The amplitude Δ is defined by the mean square value of the anisotropic interactions (in angular frequency units) and the coherence is given by the correlation time τ_c , which is a measure of the time in which a molecule persists in a specific orientation. A random process is considered fast if $\Delta\tau_c < 1$, with $\tau_c = 10^{-10} - 10^{-11}$ sec. Under this condition the anisotropic terms are averaged to zero and the spectrum is composed of sharp Lorentzian lines, characterized by the isotropic values of the magnetic parameters. For $\Delta\tau_c > 1$, the motions are slow and the line shape reflects directly the random frequency distribution, approaching the limiting case of polycrystalline spectra. Typical reorientation times in the slow tumbling regime range from 10^{-9} to 10^{-6} sec and they are usually observed when a spin probe is dissolved in a viscous solvent, like for example a LC. In this motional regime, the dynamics of the spins strongly couple to the orientational degrees of freedom of the molecule, thus the ESR spectrum can no longer be described as a simple superposition of Lorentzian lines, as for the fast motional region, and the solution of the ESR line shape problem requires a specific theory [20, 21] which is treated in Section 2.2.1.

2.2.1 Theory

A quantum mechanical wave function Ψ can be expanded in a complete set of orthonormal functions V_n as

$$\Psi(t) = \sum_n c_n(t) V_n \quad (2.34)$$

The density matrix, which contains all the information for calculating the observable quantities, is defined to be

$$\rho_{nm}(t) = \overline{c_n(t) c_m^*(t)} \quad (2.35)$$

where the bar indicates an average over a statistical ensemble.

The time dependence of the coefficients $c_n(t)$ can be obtained from the time dependent Schrödinger equation and the density matrix equation motion is given by the quantum mechanical Liouville equation

$$\partial\rho/\partial t = -i[\hat{\mathcal{H}}(t), \rho] \quad (2.36)$$

Since solving the exact equations of motion for all the molecules in the sample would be an impossible task, some physically reasonable assumptions must be introduced. First, we assume that the equation of motion for the density matrix (Eq. 2.36) has the same Hamiltonian $\hat{\mathcal{H}}(t)$, expressed in angular frequency units, for all the members of the ensemble. Now, we assume that the time dependence of the spin Hamiltonian $\hat{\mathcal{H}}(t)$ for a spin probe arises from interactions with its environment, such that $\hat{\mathcal{H}}(t)$ is fully determined by a complete set of variables $\mathbf{\Omega}$. In practice, $\mathbf{\Omega} \equiv \alpha, \beta, \gamma$, the Euler angles needed to describe the instantaneous orientation of a molecule fixed frame (e. g. the diffusion frame) with respect to a laboratory fixed frame (the Z axis of which is traditionally chosen to lie along the static magnetic field or the mean director). We also assume that the $\mathbf{\Omega}$ time dependence is described by a stationary Markov process, so that the probability of being in a state $\mathbf{\Omega}_2$ at time t_2 , if in the state $\mathbf{\Omega}_1$ at time $t_1 = t_2 - \Delta t$, is independent of the value of $\mathbf{\Omega}$ at any time earlier than t_1 and it is related only to Δt and not to t_1 . A stationary Markov process can be described by a differential equation

$$\partial P(\mathbf{\Omega}, t)/\partial t = -\Gamma_{\Omega} P(\mathbf{\Omega}, t) \quad (2.37)$$

where $P(\mathbf{\Omega}, t)$ is the probability of the free radical being in a state $\mathbf{\Omega}$ at a time t and Γ_{Ω} is the rotational diffusion operator, which is independent of time and it is related only to the orientation of the diffusing molecule relative to the mean director.

It is also assumed that the stochastic process has a unique equilibrium distribution $P_0(\mathbf{\Omega})$ characterized by

$$\Gamma_{\Omega} P_0(\mathbf{\Omega}) = 0 \quad (2.38)$$

For LC this equilibrium distribution is given by

$$P_0(\mathbf{\Omega}) = \frac{\exp(-U(\mathbf{\Omega})/kT)}{\int d\mathbf{\Omega} \exp(-U(\mathbf{\Omega})/kT)} \quad (2.39)$$

The stochastic Liouville equation of motion is then

$$\partial\rho(\mathbf{\Omega}, t)/\partial t = -i[\hat{\mathcal{H}}(\mathbf{\Omega}), \rho(\mathbf{\Omega}, t)] - \Gamma_{\Omega} \rho(\mathbf{\Omega}, t) \quad (2.40)$$

where $\rho(\mathbf{\Omega}, t)$ is the value of the density matrix associated to a particular $\mathbf{\Omega}$, hence to $\hat{\mathcal{H}}(\mathbf{\Omega})$. Thus, instead of looking at the explicit time dependence of the spin Hamiltonian $\hat{\mathcal{H}}(t)$ involving the interaction with its environment, the spin Hamiltonian is written in terms of random variables and its modulation (due to rotational motion) is expressed by the time dependence of $\mathbf{\Omega}$.

In summary the fundamental problem in slow motional ESR spectroscopy is to

compare solutions of the stochastic Liouville operator equation with experimental spectra so as to extract the correct stochastic operator Γ and obtain the magnitude of the relevant physical parameters.

The steady-state spectrum in presence of a single rotating microwave frequency field, with angular frequency ω and magnitude H_1 , is determined by the power absorbed from this field. For the λ hyperfine line at an orientation specified by Ω , the power absorbed $P_\lambda(\Omega)$ is

$$P_\lambda(\Omega) = 2N\hbar\omega d_\lambda Z_\lambda^{(1)''}(\Omega) \quad (2.41)$$

where N is the concentration of the electron spins, d_λ is the transition moment given by $d_\lambda = 1/2 \gamma_e H_1 \langle \lambda^- | \hat{S}_- | \lambda^+ \rangle$ (where \hat{S}_- is the electron spin-lowering operator and λ^\pm are the $m_S = \pm 1/2$ states at the λ transition) and $Z_\lambda^{(1)''}$ is defined by the series of equations

$$(\rho - \rho_0)_\lambda = \chi_\lambda \quad (2.42)$$

$$\chi_\lambda = \sum_{n=-\infty}^{\infty} [\exp(in\omega t)] Z_\lambda^{(n)} \quad (2.43)$$

$$Z_\lambda^{(n)} = Z_\lambda^{(n)'} + iZ_\lambda^{(n)''} \quad (2.44)$$

In Eq. 2.42 ρ_0 is the equilibrium spin density matrix. It is important to note that in Eq. 2.43 only the $n = 1$ term is needed in absence of saturation and $Z_\lambda^{(1)'}$ and $Z_\lambda^{(1)''}$ represent the magnetization components M_x and M_y for the λ line.

The total absorption is then obtained as the equilibrium average of Eq. 2.41 over all the Ω

$$P_\lambda = 2N\hbar\omega d_\lambda \overline{Z_\lambda^{(1)''}} \quad (2.45)$$

with

$$\overline{Z_\lambda^{(n)}} = \int Z_\lambda^{(n)}(\Omega) P_0(\Omega) d\Omega \quad (2.46)$$

The total spin Hamiltonian expressed in angular frequency units is now separated into three components

$$\hat{\mathcal{H}}(\Omega) = \hat{\mathcal{H}}_0 + \hat{\mathcal{H}}_1(\Omega) + \hat{\epsilon}(t) \quad (2.47)$$

1. $\hat{\mathcal{H}}_0$ is orientation independent and

$$\hbar\hat{\mathcal{H}}_0 = g_s \beta_e H_0 S_z - \hbar\gamma_e \sum_i a_i S_z I_z \quad (2.48)$$

where g_s is the isotropic splitting factor value relative to motionally narrowed region, S_z and I_z are the electron and the nuclear spin operator corresponding to the projection of \mathbf{S} and \mathbf{I} along the magnetic field direction and a_i is the isotropic hyperfine coupling constant of the i -th nucleus.

2. $\hat{\mathcal{H}}_1(\mathbf{\Omega})$ is the perturbation operator on the reorientation angles $\mathbf{\Omega}$ and, being a scalar, can be expressed as the scalar product of two tensors

$$\hat{\mathcal{H}}_1(\mathbf{\Omega}) = \sum_{L, m, m'', \mu, i} D_{-m, m''}^{(L)}(\mathbf{\Omega}) F_{\mu, i}^{(L, m)} A_{\mu, i}^{(L, m'')} \quad (2.49)$$

where $F_{\mu, i}^{(L, m)}$ and $A_{\mu, i}^{(L, m'')}$ are irreducible tensor components of rank L and component m , with the F being spatial functions in molecule-fixed coordinates, while A consists only of spin operators quantized in the laboratory axis system. The subscript μ and i refer to the type of perturbation and nuclei, respectively. The Wigner rotation matrix $D_{-m, m''}^{(L)}(\mathbf{\Omega})$ include the transformation from the molecule-fixed axis system (x, y, z) into the laboratory system (X, Y, Z) . We shall be concerned with the \mathbf{A} and \mathbf{g} tensors for which $L = 2$.

3. $\hat{\epsilon}(t)$ describes the interaction between the electron spin with the oscillating microwave field

$$\hat{\epsilon}(t) = \frac{1}{2} \gamma_e H_1 [\hat{S}_+ \exp(-i\omega t) + \hat{S}_- \exp(i\omega t)] \quad (2.50)$$

When the $\langle \lambda^- | \lambda^+ \rangle$ matrix elements of Eq. 2.40 are considered and Eqs. 2.42 - 2.44 are used, the steady-state equation for $Z_\lambda^{(n)}$ is found to be

$$(n\omega - \omega_\lambda) Z_\lambda^{(n)}(\mathbf{\Omega}) + [\hat{\mathcal{H}}_1(\mathbf{\Omega}), Z^{(n)}(\mathbf{\Omega})]_\lambda - i[\Gamma_\Omega Z^{(n)}]_\lambda + d_\lambda [\chi_{\lambda^+}^{(n-1)} - \chi_{\lambda^-}^{(n-1)}] = q\omega_\lambda d_\lambda \quad (2.51)$$

For reasonable temperatures and typical ESR field strengths, $\rho_0 = N'^{-1} - q\mathcal{H}_0$, with N'^{-1} the number of spin eigenstates of \mathcal{H}_0 and $q = \hbar/N'^{-1}kT$. Also $\hbar\omega_\lambda = E_{\lambda^+} - E_{\lambda^-}$ and the E_{λ^\pm} are the eigenenergies of \mathcal{H}_0 for the λ^\pm states.

It is convenient at this point to introduce a symmetrizing transformation for the evolution operator

$$\tilde{\Gamma}_\Omega = P_0^{-1/2} \Gamma_\Omega P_0^{1/2} \quad (2.52)$$

and similarly

$$\tilde{Z}_\lambda^{(n)}(\mathbf{\Omega}) = P_0^{-1/2} [Z_\lambda^{(n)}(\mathbf{\Omega}) P_0] \quad (2.53)$$

Thus Eq. 2.46 turns into

$$\overline{Z_\lambda^{(n)}} = \int \tilde{Z}_\lambda^{(n)}(\mathbf{\Omega}) P_0^{1/2} d\mathbf{\Omega} \quad (2.54)$$

and Eq. 2.51 becomes

$$(n\omega - \omega_\lambda) \tilde{Z}_\lambda^{(n)}(\mathbf{\Omega}) + [\hat{\mathcal{H}}_1(\mathbf{\Omega}), \tilde{Z}^{(n)}(\mathbf{\Omega})]_\lambda - i[\tilde{\Gamma}_\Omega \tilde{Z}^{(n)}]_\lambda + d_\lambda [\tilde{\chi}_{\lambda^+}^{(n-1)} - \tilde{\chi}_{\lambda^-}^{(n-1)}]$$

$$= q\omega_\lambda d_\lambda P_0^{1/2} \quad (2.55)$$

In order to solve for the absorption, Eq. 2.54, it is necessary to solve first the diffusion equation (Eq. 2.37). The solution of such a partial differential equation can be expressed in terms of a complete set of orthonormal eigenfunctions $G_m(\mathbf{\Omega})$, such that

$$\tilde{\Gamma}_\Omega G_m(\mathbf{\Omega}) = -\tau_m^{-1} G_m(\mathbf{\Omega}) \quad (2.56)$$

where τ_m^{-1} is the m th eigenvalue.

The matrix elements in Eq. 2.53, expanded in the orthonormal set $G_m(\mathbf{\Omega})$, are

$$\tilde{Z}_\lambda^{(n)}(\mathbf{\Omega}) = \sum_m [C_m^{(n)}(\omega)]_\lambda G_m(\mathbf{\Omega}) \quad (2.57)$$

and the coefficient $C_m^{(n)}(\omega)$ is an operator in the spin space which is a function of ω , but independent of $\mathbf{\Omega}$.

Substituting Eq. 2.57 into Eq. 2.55, premultiplying the resulting equation by $G_m^*(\mathbf{\Omega})$ and then integrating over $\mathbf{\Omega}$, one obtains

$$\begin{aligned} [(n\omega - \omega_\lambda) - i\tau_m^{-1}] [C_m^{(n)}(\omega)]_\lambda + \sum_{m'} \int d\mathbf{\Omega} G_m^*(\mathbf{\Omega}) [\hat{\mathcal{H}}_1(\mathbf{\Omega}), C_{m'}^{(n)}]_\lambda C_{m'}^{(n)}(\mathbf{\Omega}) + \\ d_\lambda ([C_m^{(n-1)}]_{\lambda+} - [C_m^{(n-1)}]_{\lambda-}) = q\omega_\lambda d_\lambda \delta(m, 0) \delta(n, 1) \end{aligned} \quad (2.58)$$

Since the absorption (Eq. 2.45) depends only on $Z_\lambda^{(1)''}$, then solving Eq. 2.58 for $[C_0^{(1)}]_\lambda$ for all the allowed transitions will give the spectral line shapes. Furthermore, in the absence of saturation phenomena, $d_\lambda = 0$ in the left-hand side of Eq. 2.58 and then with $n = 1$ the needed expression is obtained.

2.2.2 Rotational modulation in isotropic liquids

When the general theory of Section 2.2.1 is applied to rotational modulation, $\mathbf{\Omega}$ refers to the Euler angles for a tumbling molecular axis with respect to a fixed laboratory axis system. For a molecule undergoing many collisions, causing small random angular reorientations, the resulting isotropic Brownian rotational motion is a Markov process, which can be described by the rotational diffusion equation

$$\partial P(\mathbf{\Omega}, t) / \partial t = R \nabla_\Omega^2 P(\mathbf{\Omega}, t) \quad (2.59)$$

where ∇^2 is the Laplacian operator on the surface of a unit sphere and R is the rotational diffusion coefficient [22].

In an isotropic liquid, the equilibrium probability $P(\mathbf{\Omega})$ will be equal for all the orientations, so that $P(\mathbf{\Omega}) = 1/8\pi^2$. Here the Markov operator Γ_Ω (2.37) for isotropic Brownian rotation (2.59) is $-R\nabla_\Omega^2$ and the eigenfunctions are the normalized Wigner rotation matrices

$$G_m \rightarrow \Phi_{KM}^L(\mathbf{\Omega}) = [(2L + 1)/8\pi^2]^{1/2} D_{K.M}^L(\mathbf{\Omega}) \quad (2.60)$$

with eigenvalues $RL(L + 1)$.

For axially symmetric Brownian rotation about a molecule-fixed z axis, the eigenvalues associated to the Wigner rotation matrices are given by

$$\Gamma_{\Omega} \Phi_{KM}^L = [R_{\perp} L(L + 1) + (R_{\parallel} - R_{\perp}) K^2] \Phi_{KM}^L \quad (2.61)$$

where R_{\perp} and R_{\parallel} are the rotational diffusion constants about the x, y axes and z axis, respectively [23]. The quantum number K and M of the Wigner matrices refer to the projections along the body-fixed symmetry axis and along a space-fixed axis, respectively.

A number of different models for rotational reorientation can be proposed. Some useful ones are the corresponding results are here summarized:

1. Brownian rotational diffusion
2. Free diffusion, in which a molecule freely rotates for a time τ and then reorients instantaneously
3. Jump diffusion, in which a molecule keeps a fixed orientation for a time τ and then jumps instantaneously to a new orientation

The results relative to the isotropic reorientation (Eq. 2.62) and to the anisotropic rotational diffusion (Eq. 2.63) can be summarized as

$$\tau_L^{-1} = B_L L(L + 1) R \quad (2.62)$$

$$\tau_{L,K}^{-1} = (B_L / R_{\perp}) [R_{\perp} L(L + 1) + (R_{\parallel} - R_{\perp}) K^2] \quad (2.63)$$

where B_L is a model dependent parameter

- $B_L = 1$ for Brownian motion
- $B_L = [1 + L(L + 1)]^{-1/2}$ for free diffusion
- $B_L = [1 + L(L + 1)]^{-1}$ for jump diffusion

Thus, in the slow motional region, where the ESR line shape is simulated in terms of an expansion in $D_{(K,M)}^L$ with eigenvalues $\tau_{L,K}^{-1}$, the ESR spectra will be model sensitive. In particular, the L dependence of the eigenvalues is due to the choice of the reorientational model, while the quantum number K play the same role in all the models.

2.2.3 Anisotropic liquids

Suppose now that the liquid has a preferred axis orientation, i. e. the director axis. We now write the perturbing Hamiltonian (Eq. 2.49) as

$$\hat{\mathcal{H}}_1(\boldsymbol{\Omega}, \boldsymbol{\Psi}) = \sum_{L, M, M', K, \mu, i} (-1)^K D_{-K, M'}^{(L)}(\boldsymbol{\Omega}) D_{-M', M}^{(L)}(\boldsymbol{\Psi}) F_{\mu, i}^{(L, K)} A_{\mu, i}^{(L, M)} \quad (2.64)$$

Eq. 2.64 is based on two sets of rotations of the coordinate systems: first from the molecular axis system (x, y, z) into the director axis system (x'', y'', z'') , with Euler angles $\boldsymbol{\Omega} \equiv \alpha, \beta, \gamma$, and then into the laboratory system (X, Y, Z) , with Euler angles $\boldsymbol{\Psi}$. The orientation of the director relative to the laboratory frame can be specified by the two polar angles θ' and ϕ' such that $\boldsymbol{\Psi} = (0, \theta', \phi')$. More precisely one means by the molecular coordinate system (x, y, z) the principal axis system for the orientation of the molecule in the mesophase. It may be also necessary to transform from the principal axis system of the magnetic interactions (x', y', z') to the (x, y, z) system with Euler angles $\boldsymbol{\Theta}$ according to

$$F_{\mu, i}^{(L, K)} = \sum_{K'} D_{K, K'}^L(\boldsymbol{\Theta}) F_{\mu, i}'^{(L, K')} \quad (2.65)$$

where $\boldsymbol{\Theta} \equiv \alpha', \beta', \gamma'$.

The diffusion equation for a particle undergoing Brownian rotational diffusion in the presence of a potential U is given by

$$\frac{\partial P(\boldsymbol{\Omega}, t)}{\partial t} = -\mathcal{M} \cdot \left[\mathbf{R} \cdot \frac{\mathcal{M}U(\boldsymbol{\Omega})}{kT} + \mathbf{R} \cdot \mathcal{M} \right] P(\boldsymbol{\Omega}, t) \equiv -\Gamma_{\boldsymbol{\Omega}} P(\boldsymbol{\Omega}, t) \quad (2.66)$$

where $U(\boldsymbol{\Omega})$ can be taken to be the pseudopotential for a liquid crystal, \mathcal{M} is the vector operator which generates an infinitesimal rotation and it is identified with the quantum mechanical angular momentum operator for a rigid rotator, and \mathbf{R} is the diffusion tensor of the molecule. Both \mathbf{R} and \mathcal{M} are defined in the (x, y, z) molecular coordinate system. The angular momentum operator \mathcal{M} is defined by

$$\mathcal{M}^2 \phi_{KM}^L(\boldsymbol{\Omega}) = L(L+1) \phi_{KM}^L(\boldsymbol{\Omega}) \quad (2.67)$$

$$\mathcal{M}_{\pm} \phi_{KM}^L(\boldsymbol{\Omega}) = [(L \mp K)(L \pm K + 1)]^{1/2} \phi_{K \pm 1, M}^L(\boldsymbol{\Omega}) \quad (2.68)$$

$$\mathcal{M}_z \phi_{KM}^L(\boldsymbol{\Omega}) = K \phi_{KM}^L(\boldsymbol{\Omega}) \quad (2.69)$$

where the $\phi_{KM}^L(\boldsymbol{\Omega})$ are the eigenfunctions of \mathcal{M}^2 and \mathcal{M}_z given by Eq. 2.60 and

$$\mathcal{M}_{\pm} = \mathcal{M}_x \pm i \mathcal{M}_y \quad (2.70)$$

When $U(\boldsymbol{\Omega}) = 0$, then Eq. 2.66 is simply the equation for the asymmetric Brownian rotational diffusion in isotropic liquids.

The restoring potential for LCs can be written in its most general form as

$$U(\mathbf{\Omega}) = \sum_{L,K,M} \epsilon_{KM}^L D_{KM}^L(\alpha, \beta, \gamma) \quad (2.71)$$

The assumption of cylindrical symmetry about the director axis \mathbf{n} implies that all average taken over the angles γ vanish unless $M = 0$.

The uniaxial property of a nematic LC, i. e. $\mathbf{n} = -\mathbf{n}$, implies that L must be even. In the linear combinations of the $U(\mathbf{\Omega})$ the terms with $L > 2$ are in general less important than those for $L = 2$, then

$$U(\mathbf{\Omega}) \sim \epsilon_0^2 D_{00}^2(\mathbf{\Omega}) + \sum_{K>0} \epsilon_{K\pm}^2 [D_{K0}^2(\mathbf{\Omega}) \pm D_{-K0}^2(\mathbf{\Omega})] \quad (2.72)$$

The ϵ_0^2 and $\epsilon_{K\pm}^2 = \epsilon_K^2 \pm \epsilon_{-K}^2$ (with the upper sign for $K > 0$ and the lower sign $K < 0$) are themselves second-rank irreducible tensor components, so that, in the principal axis of molecular orientation system (x, y, z) their Cartesian components $\epsilon_{i,j}$ are diagonalized, with $Tr_i \epsilon_{i,j} = 0$ and complete specification is given by ϵ_0^2 and ϵ_{2+}^2 . The ordering tensor is defined by

$$\langle D_{KM}^L(\mathbf{\Omega}) \rangle = \int d(\mathbf{\Omega}) P_0(\mathbf{\Omega}) D_{KM}^L(\mathbf{\Omega}) \quad (2.73)$$

where $L = 2$ and $M = 0$. It follows that only the terms $\langle D_{20}^2(\mathbf{\Omega}) + D_{-20}^2(\mathbf{\Omega}) \rangle$ and $\langle D_{00}^2(\mathbf{\Omega}) \rangle$ are nonzero, i. e. $\langle D_{KM}^2(\mathbf{\Omega}) \rangle$ is also diagonalized. Thus the diagonalized potential becomes

$$U(\mathbf{\Omega}) = \epsilon_0^2 D_{00}^2(\mathbf{\Omega}) + \epsilon_{2+}^2 [D_{20}^2(\mathbf{\Omega}) + D_{-20}^2(\mathbf{\Omega})] \quad (2.74)$$

or equivalently

$$U(\alpha, \beta) = \gamma_2 \cos^2 \beta + \epsilon \sin^2 \beta \cos(2\alpha) \quad (2.75)$$

where $\epsilon_0^2 = 2\gamma_2/3$ and $\epsilon_{2+}^2 = 2\epsilon(6)^{1/2}$. For molecules in which the molecular x and y axes are aligned to different extents, ϵ is nonzero. If we choose the orientation coordinate system such that the z axis tends to align to a greater degree either parallel or perpendicular to the director than does the x or the y axis, we have $|\gamma_2| > |\epsilon|$. The case $\epsilon < 0$ corresponds to the y axis being ordered preferential to the x axis along the direction of \mathbf{n} and/or to the x axis being ordered to a greater degree perpendicular to the \mathbf{n} than is the y axis.

We assume a axially symmetric rotation about z such that $R_{xx} = R_{yy} = R_{\perp}$ and $R_{zz} = R_{\parallel}$. Further, we introduce the definitions

$$\lambda \equiv -\gamma_2/kT \quad (2.76)$$

$$\rho \equiv -\epsilon/kT \quad (2.77)$$

then the symmetrized Markov operator defined becomes

$$\tilde{\Gamma} = \mathcal{M} \cdot \mathbf{R} \cdot \mathcal{M} - f(R_{\perp}, R_{\parallel}, \lambda, \rho, \Omega) \quad (2.78)$$

where

$$f(R_{\perp}, R_{\parallel}, \lambda, \rho, \Omega) = \sum_{L=0,2,4} [X_{00}^L D_{00}^L + \sum_{0 < K \leq L} X_{K0}^L (D_{K0}^L + D_{-K0}^L)] \quad (2.79)$$

with

$$\begin{aligned} X_{00}^0 &= -(2/15) [R_{\perp}(\lambda^2 + \rho^2) + 2R_{\parallel} \rho^2] \\ X_{00}^2 &= \{R_{\perp} \lambda - [R_{\perp}(\lambda^2 + \rho^2) - 4R_{\parallel} \rho^2]/21\} \\ X_{00}^4 &= 4 [2R_{\perp}(\lambda^2 + \rho^2) - R_{\parallel} \rho^2]/35 \\ X_{20}^2 &= 6^{1/2} \rho [(R_{\perp} + 2R_{\parallel})/3 + 2R_{\perp} \lambda/7] \\ X_{20}^4 &= 4 (10)^{1/2} R_{\perp} \rho \lambda / 35 \\ X_{40}^4 &= (8/35)^{1/2} R_{\parallel} \rho^2 \end{aligned}$$

2.2.4 Nitroxides

For nitroxides the \mathbf{g} and \mathbf{A} tensors yield to a perturbation operator $\hat{\mathcal{H}}_1$ given by

$$\begin{aligned} \hat{\mathcal{H}}_1(\Omega) &= D_{0,0}^2(\Omega) [F_0 + D' I_Z] S_Z + \\ & [D_{0,0}^2(\Omega) + D_{2,0}^2(\Omega)] \times (F_2 + D^{(2)'} I_Z) S_Z + \\ & [D_{0,1}^2(\Omega) I_+ - D_{0,-1}^2(\Omega) I_-] D S_Z + \\ & [D_{-2,-1}^2(\Omega) + D_{2,1}^2(\Omega)] D^{(2)} I_+ S_Z - \\ & [D_{-2,-1}^2(\Omega) + D_{2,-1}^2(\Omega)] D^{(2)} I_- S_Z \end{aligned} \quad (2.80)$$

where

$$F_i = \sqrt{\frac{2}{3}} g^{(i)} \hbar^{-1} \beta H_0 \quad (2.81)$$

$$g^{(0)} = \frac{1}{\sqrt{6}} [2g_{z'} - (g_{x'} + g_{y'})] \quad (2.82)$$

$$g^{(2)} = \frac{1}{2} [g_{x'} + g_{y'}] \quad (2.83)$$

$$D = \frac{(|\gamma_e|)}{2\sqrt{6}} (A_{x'} + A_{y'} - 2A_{z'}) \quad (2.84)$$

$$D^{(2)} = \frac{1}{4} |\gamma_e| (A_{y'} - 2A_{z'}) \quad (2.85)$$

with $D' = -(8/3)^{1/2} D$ and $D^{(2)'} = -(8/3)^{1/2} D^{(2)}$.

2.3 Spin Probe Technique

As mentioned before, we used the spin probe technique (see the beginning of Chapter 2) to investigate the orientational order and the dynamic behavior of various LC systems. While the detailed description of the different systems together with their relevance and the results obtained is found in the following chapters, here it is discussed the experimental method applied to acquire and analyze the ESR spectra.

2.3.1 Experimental Spectra

All the systems studied are based on an LC matrix of 4-cyano-4'-*n*-pentylbiphenyl (5CB), which was obtained from Merck KGaA (Darmstadt, Germany) and used without further purification. This compound, whose chemical structure is shown in Figure 2.7, exhibits, on heating, the nominal phase sequence:

- Crystal-Nematic: 295.7 K
- Nematic-Isotropic: 308.5 K

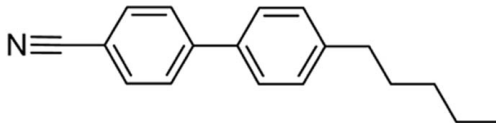


Figure 2.7: Molecular structure of 5CB LC.

To monitor the order and the dynamics of the LC system, we chose the nitroxide spin probe 3 β -DOXYL-5 α -cholestane (CSL), purchased from Aldrich. Its size, rigidity and rod-like shape similar to that of the 5CB result in a strong orientation by the LC host and thus make this molecule a suitable probe for our purposes [14, 24–30]. The CSL structure is shown in Figure 2.8 together with the chosen ordering (*xyz*, solid line) and magnetic (*x'y'z'*, dashed line) molecular frames and the principal components R_{\perp} (reorientation of the molecular long axis) and R_{\parallel} (rotation around the molecular long axis) of the rotational diffusion tensor. The convention adopted for the ordering and magnetic frames has been discussed in details [28]. In particular, we observe that the magnetic frame is tilted relative to the ordering frame and that the Euler angles taking the ordering into the magnetic frame are: $\alpha = 0^{\circ}$, $\beta \sim 15^{\circ}$ and $\gamma = 90^{\circ}$ [28]. For this compound, dissolved in the 5CB LC, the principal g factors and hyperfine splitting tensor components used are reported in Table 2.2 and correspond to the literature values [28] corrected for the polarity of the environment so as to recover the scalar hyperfine constant of 14.565 G experimentally observed.

A very small amount of probe, typically $\sim 10^{-4} g_{CSL}/g_{5CB}$, was sufficient to carry out the ESR experiments. Since the sample preparation and the method employed to introduce the spin probe into the LC matrix differs from system to system, the

	g_{ij}	A_{ij} /G	a /G
$g_{x'x'}$	2.0027	$A_{x'x'}$ 5.98	a 14.565
$g_{y'y'}$	2.0088	$A_{y'y'}$ 5.98	
$g_{z'z'}$	2.0061	$A_{z'z'}$ 31.74	

Table 2.2: Magnetic parameters for the CSL nitroxide radical.

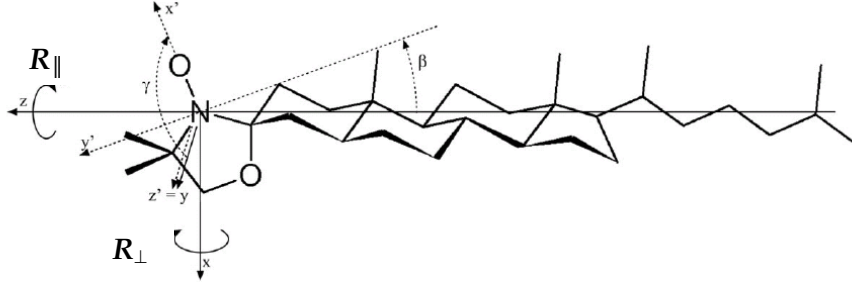


Figure 2.8: The CSL spin probe together with the chosen ordering and magnetic molecular frames (see text for details).

details are described in the next chapters.

ESR spectra were recorded with a Bruker ESP300E spectrometer equipped with an ER 041XG microwave X-band (9.5 GHz) Gunn diode bridge and a rectangular ER 4102ST cavity. The samples inserted into the cavity were thermostated with a nitrogen flux through a variable temperature unit Bruker B-VT 2000. The sample temperature was monitored with a calibrated type T thermocouple (Comark Ltd.) located in contact with the sample. The temperature of each sample was varied in a range sufficiently wide so as to explore both the nematic and the isotropic phase of the LC matrix.

2.3.2 Simulated Spectra

The simulation of the ESR spectra was carried out with an implementation of the Slow Tumbling theory (Section 2.2), developed by Freed and collaborators, and assuming rotational diffusion for the probe [20, 31, 32].

Depending on the properties of the system under investigation, two different models were used to simulate the ESR line shapes.

1. Monodomain Model

In this approach all the nematic directors are assumed to be perfectly aligned parallel to the magnetic field. The probe reorients in a local ordered domain with local director orientation $\mathbf{\Omega}_{dir}$ with respect to the laboratory frame. Assuming a uniaxial director distribution, $P(\mathbf{\Omega}_{dir}) \equiv P(\beta_{dir}) = \delta(\beta_{dir})$, where β_{dir} is the angle between the local domain director and the magnetic field. The monodomain spectrum, $I(\omega - \omega_0)$ at frequency ω , being $\omega_0 = g\beta_e H_0 / \hbar$, is given by the standard stochastic Liouville equation [20, 31, 32]

$$I(\omega - \omega_0; \beta_{dir}) = \frac{1}{\pi} \langle \langle v | [(\Gamma_{\Omega} - i\mathcal{L}) + i(\omega - \omega_0)I]^{-1} | v \rangle \rangle \quad (2.86)$$

where \mathcal{L} is the Liouville superoperator obtained from the orientation-dependent spin Hamiltonian (Eq. 2.40), Γ_{Ω} is the stochastic evolution operator describing the changes in the orientation of the probe in its local domain, $|v\rangle$ is a vector containing spin transition moments averaged over the equilibrium ensemble, and I is the identity. Assuming the probe reorientation to be diffusional

$$\langle \langle \sigma_1 | \Gamma_{\Omega} | \sigma_2 \rangle \rangle = \delta_{L_1, L_2} \delta_{M_1, M_2} \delta_{K_1, K_2} \delta_{p_1^S, p_2^S} \delta_{q_1^S, q_2^S} \delta_{p_1^I, p_2^I} \delta_{q_1^I, q_2^I} \{R_{\perp} L_1(L_1 + 1) + (R_{\parallel} - R_{\perp}) K_1^2\} \quad (2.87)$$

where

$$|\sigma_n\rangle = \left(\frac{2L+1}{8\pi^2} \right)^{1/2} D_{M,K}^L(\Omega) |p_n^S, q_n^S, p_n^I, q_n^I\rangle \quad (2.88)$$

is the spin-orientational space basis set and R_{\parallel} and R_{\perp} are the principal components of the rotational diffusion tensor of the probe for rotations around its long or short axis, respectively. In practice, the basis set is obtained from the direct product of the electron spin, S , with the nuclear spin, I , eigenfunctions

$$|p^S, q^S, p^I, q^I\rangle = (|S, m_S\rangle \langle S, m'_S|) (|I, m_I\rangle \langle I, m'_I|) \quad (2.89)$$

while $D_{M,K}^L$ are the orientational Wigner rotation matrixes (Eq. 2.49, 2.60, 2.64) with L , M , and K integers, $L \geq 0$ and $|M|, |K| \leq L$, forming the basis set for the orientations. The reorientational motion of the probe is assumed to take place in the local mean field ordering potential (Eq. 2.71)

$$U(\Omega) = -kT \{ \lambda_{00} D_{00}^2(\Omega) \} \quad (2.90)$$

which is also employed, when needed, to calculate local orientational order parameters

$$\langle P_L \rangle = \langle D_{00}^L(\Omega) \rangle = \frac{\int D_{00}^L(\Omega) \exp[\lambda_{00} D_{00}^2(\Omega)] d\Omega}{\int \exp[\lambda_{00} D_{00}^2(\Omega)] d\Omega} \quad (2.91)$$

where Ω gives the probe orientation with respect to the local director and λ_{00} is the strength of the potential.

2. Polydomain Model

If the spin probe reorients in local domains when the director distribution can be described by

$$P(\mathbf{\Omega}_{dir}) \equiv P(\beta_{dir}) \propto \exp[a P_2(\cos\beta_{dir})] \quad (2.92)$$

with P_2 a second rank Legendre polynomial 1.5 and a a positive constant, the resulting ESR spectrum is given by the superposition of the ones of the individual domains [28, 33]

$$I(\omega - \omega_0) = \int P(\mathbf{\Omega}_{dir}) I(\omega - \omega_0; \mathbf{\Omega}_{dir}) d(\mathbf{\Omega}_{dir}) \quad (2.93)$$

This approach clearly comprises the limiting cases of a completely random domain distribution, $P(\mathbf{\Omega}_{dir}) = 1/\pi$, and of a monodomain distribution. It is well-known that spectra for the two limiting cases are clearly different, indicating that the ESR technique is suitable for this kind of investigation of the system structure. In general, the order of the domains can be characterized by a second-rank orientational order parameter, $\langle P_2 \rangle_{dir}$, for the local director

$$\langle P_2 \rangle_{dir} = \frac{\int P_2(\cos\beta_{dir}) \exp[a P_2(\cos\beta_{dir})] \sin\beta_{dir} d\beta_{dir}}{\int \exp[a P_2(\cos\beta_{dir})] \sin\beta_{dir} d\beta_{dir}} \quad (2.94)$$

The simulation of the experimental spectra often requires the simultaneous variations of several parameters (i. e. R_{\parallel} , R_{\perp} , coefficients of the ordering potential and contributions due to the inhomogeneous broadening) in order to obtain reasonable fits of the spectra. In our analyses, the fit parameters were optimized using a modified Gauss-Newton-Marquardt non-linear least squares method [34, 35]. As the number of the parameters to be varied increases, we are confronted with the problem that several choices of parameters can lead to fits of similar quality, thus a quantitative criterion becomes necessary to discern the best fit. The non-linear least square fitting procedure that we adopted allows to vary the user specified parameters within selected ranges and to calculate successive ESR spectra until the convergence criterion specified by the user is satisfied. Furthermore, the quantitative goodness of the fit is given in terms of the sum of the squared differences between the experimental and fitted spectra.

The best method to manage the parameter set in the fitting procedure of the experimental spectra is specific for every system and, therefore, it is detailed reported from case to case together with the appropriate model.

Chapter 3

5CB LC doped with Azobenzene Derivatives

3.1 Azobenzene properties and applications

Azobenzene is a chemical compound consisting of two phenyl rings linked by a $-\text{N}=\text{N}-$ bond. The term azobenzene, or simply azo, is often used to indicate a wide class of molecules that share the azobenzene core structure, with different chemical functional groups extending from the phenyl rings (technically, these compounds should be referred to as diazenes). It is well-known that this class of molecules can exist in two configurations, the *trans* and the *cis* form [36]. The *trans* isomer is generally more stable than the *cis*: the energy difference between the ground state of the *trans* and *cis* isomers is about 50 kJ/mol.

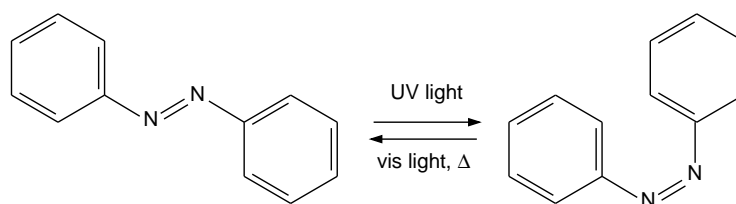


Figure 3.1: Azobenzene photoisomerization. The *trans* form (left) and the *cis* form (right) can be interconverted using light with an appropriate wavelength.

One of the most intriguing properties of the azo-group is the photochromic behavior, that is, it undergoes a change in its molecular structure upon photoirradiation (Figure 3.1). The stable *trans* form can be photoisomerized to the *cis* configuration by exposure to UV-light, which corresponds to the energy gap of the $\pi-\pi^*$ transition (Figure 3.2). The inverse reaction, i.e. *cis*-to-*trans* isomerization, can occur both thermally and photochemically; in the last case blue light, which matches the energy corresponding to the $n-\pi^*$ transition, is required (Figure 3.2). Furthermore, the photoisomerization reaction is extremely rapid, occurring on picosecond timescales, while the thermal back-relaxation usually requires hours.

The mechanism of isomerization has been the subject of some debate, with two

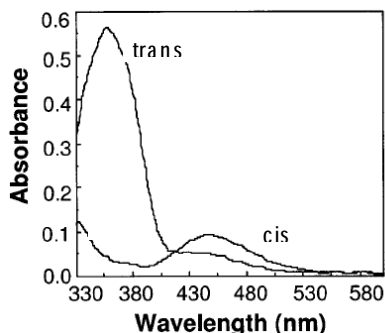


Figure 3.2: Typical absorption spectra of azocompounds showing the high-intensity π - π^* band in the UV region and the low-intensity n - π^* band in the visible region.

pathways identified as viable: a rotation about the $-\text{N}=\text{N}-$ bond, with disruption of the double bond, or via an inversion, with a semi-linear and hybridized transition state. This mechanism in the gas phase and to a minor extent in solution has been the object of a huge amount of basic studies [37–41].

Because of the fast and reversible photoisomerization, azobenzene (AB) has recently attracted a great deal of technological interest, especially for photonic applications in LC based systems [42–46]. In LC elastomers containing AB moieties, the photoisomerization can produce changes in elongation of samples up to 20% and also a precisely governable bending of the polymer film (see Figure 3.3), opening the way to the realization of photodriven actuators, valves and other devices.

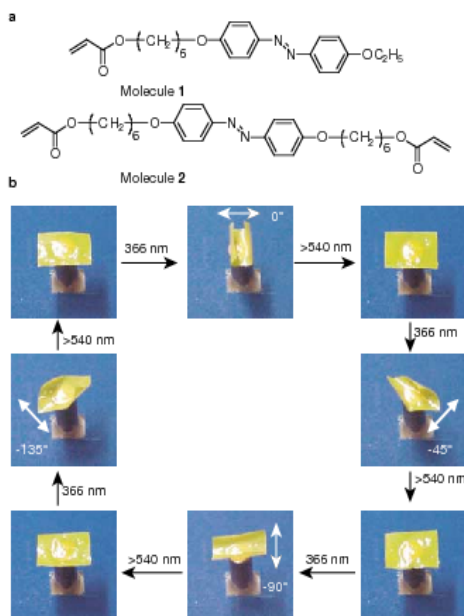


Figure 3.3: Directed bending of a polymer film by light [43]. a, Chemical structures of the liquid-crystal, monomer (molecule 1) and crosslinker (molecule 2) used for preparation of the film; b, Precise control of the bending direction of a film by linearly polarized light.

The transformation of AB in nematics induces the photomodulation of the LC orientation (Figure 3.4), thus this phenomenon can be used to obtain a photodriven bright-dark contrast in LC display. Two types of photomodulation of orientations of liquid crystals (LCs) are particularly interesting: order-order change of LCs, which modify the LC director orientation, and order-disorder change, which produce a phase transition.

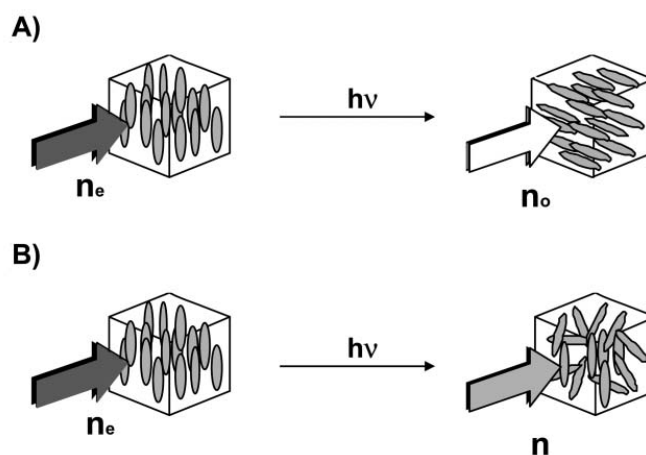


Figure 3.4: Two types of photomodulation of orientation of LC molecules [44]. A), Change in LC directors orientation (order-order change); B), Change in phases (phase transition, order-disorder change).

3.2 Photoisomerization in guest/host systems

Both from the point of view of the applications and from a more basic standpoint, it is crucial to understand how the AB isomerization acts on the surrounding medium affecting its properties. In particular, we are interested in the order-disorder changes occurring in guest/host systems, made of AB derivative molecules dissolved in a nematic LC matrix.

The change of nematic-isotropic temperature transition of an AB solution in nematics, following photoexcitation, has been demonstrated [44, 47] and interpreted in terms of a change of the ordered phase stability. The rod-like shape of the *trans* isomer, being similar to that of the LC host, can stabilize the ordered phase. On the other hand, the *cis* isomer destabilizes the LC phase because of its bent shape. Therefore, the *trans-cis* photoisomerization of the AB in the LC phase can induce disorganization of the phase structure. This is the basis of the photochemical phase transition of nematic LCs, represented in Figures 3.5 and 3.6. The nematic-isotropic phase transition temperature (T_{NI}) of the mixture with the *cis* form (T_{cc}) is much lower than that with the *trans* form (T_{ct}). If the temperature of the sample (T) is set so that $T_{ct} > T > T_{cc}$ and the sample is irradiated to cause *trans-cis* photoisomerization of the AB guest molecules, then T_{NI} decreases with an accumulation of the *cis* form, and, when T_{NI} becomes lower than the irradiation temperature T , an isothermal nematic-isotropic phase transition of the sample is induced. Photochromic reactions are usually reversible and, with *cis-trans* back-isomerization, the sample reverts to the initial LC phase. This means that phase transitions of LC systems can be induced reversibly by photochemical reactions of photoresponsive guest molecules.

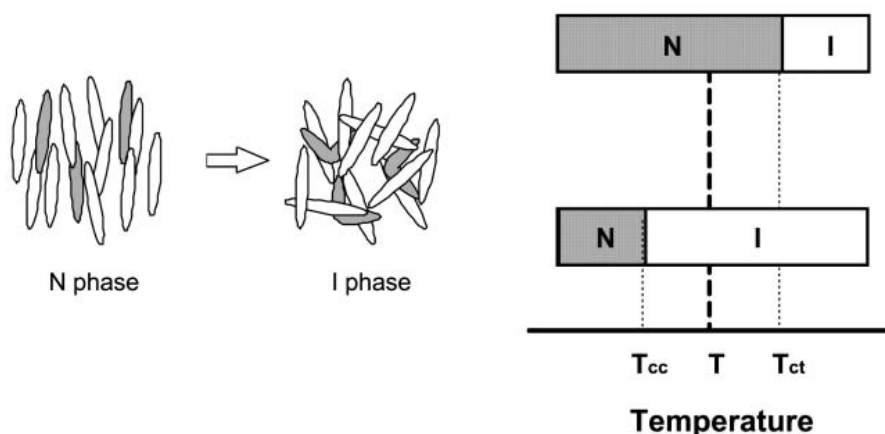


Figure 3.5: Order-disorder change: phase diagram of the photochemical phase transition of azobenzene/LC systems. N, nematic; I, isotropic.

These systems are widely investigated in order to improve their photoresponsive properties, i. e. the time necessary to switch the isothermal phase transition [47–50], while a study focused on the way the order and the local dynamics (“rotational microviscosity”) are influenced is, to our knowledge, still lacking.

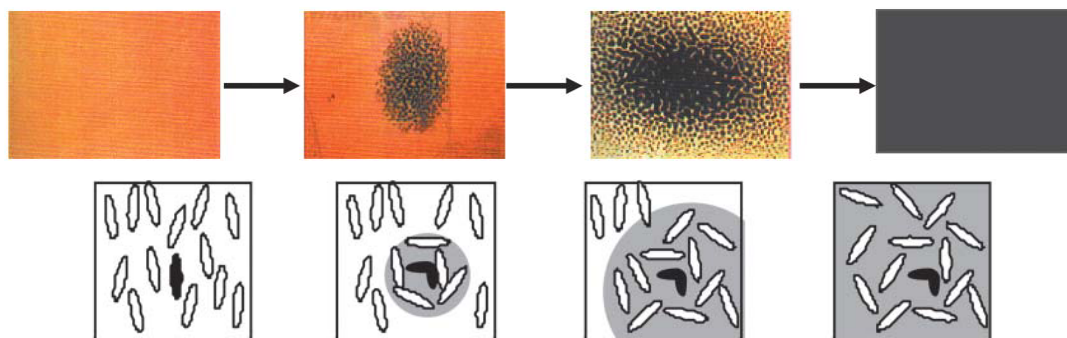


Figure 3.6: Order-disorder change: mechanism of photochemical phase transition in azobenzene/LC systems [44]. The mesogens and the azo-dyes are depicted as white and black ellipsoids, respectively.

The orientational order, the dynamics and in general the physical properties of nematic LCs are influenced by dissolved solutes [51–53]. The most obvious manifestation is the disruption of alignment induced by spherical solutes, leading to a lowering of the nematic-isotropic phase transition temperature [54]. The effects on the medium are, however, related to the molecular features of the solutes (shape, dipole moment, polarizability, etc.) and in a number of cases, e.g. for molecules with a relatively large length-to-width ratio, a stabilization of the solvent ordering and an increase of T_{NI} can occur [55]. Although the molecular mechanism for the solute-solvent interaction is far from clear, a relation to molecular shape is often invoked [56]; in this context, AB solutes represent a particularly interesting case, since by exposing the nematic solution to a near UV light, it is possible to drive a change in shape by photoexciting the *trans* to *cis* transformation.

In this study we have then decided to investigate these changes by considering a series of AB compounds of similar shape but with varying chemical properties. In particular, we have studied a set of eight *p*-substituted AB (Figure 3.7) and a set of two *p,p'*-disubstituted AB (Figure 3.15) in the nematic 4-cyano-4'-*n*-pentylbiphenyl (5CB, Figure 2.7). We have then considered solutions of *trans* isomers of these compounds at different concentrations and we have followed the changes with temperature of the order and the dynamics of the medium, as experienced by a nitroxide spin probe, using the well established ESR spin probe methodology (see Chapter 2). We have then generated in situ *cis* isomer solutions and we have repeated the temperature dependent measurements. In this chapter, we present our results and compare them, showing that the effect of solutes does not always reduce to a simple scaling of the order plot, as expected when only T_{NI} is affected. On the contrary, in some cases the effect on the order is more profound with a change of the functional dependence of $\langle P_2 \rangle$ on the temperature. Finally, we also try to relate the results to molecular features of the solutes studied.

3.3 *p*-substituted Azobenzene Derivatives

3.3.1 Experimental Section

The liquid crystal 5CB was used as host matrix (Figure 2.7) and the nitroxide spin probe was the 3 β -DOXYL-5 α -cholestane (CSL) (Figure 2.8). The structure of the photoactive monosubstituted units used was 4-R-phenylazobenzene (see Figure 3.7), where R = H, F, Br, CH₃, CF₃, OCH₃, *On*-Bu, *Ot*-Bu. None of the azo-derivatives considered showed a LC phase. Azobenzene was purchased from Aldrich and used without further purification. The azo-derivatives were synthesized according to the Mills reaction[57], in which nitrosobenzene combines with primary arylamines in glacial acetic acid to give unsymmetrical azo-derivatives. The synthesis and characterization of 4-*Ot*-Bu-phenylazobenzene (1-[4-(*tert*-butoxy)phenyl]-2-phenyldiazene) is original and is reported in the Appendix B.

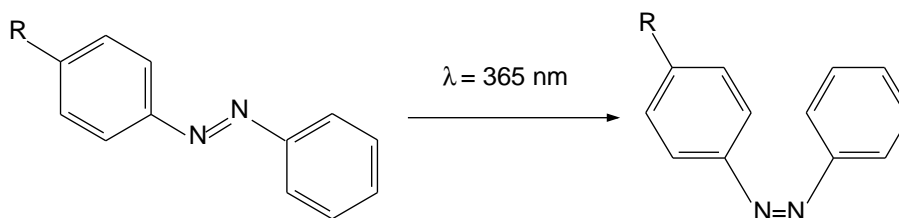


Figure 3.7: Chemical structure of the photoactive units 4-R-azobenzene (R = H, F, Br, CH₃, CF₃, OCH₃, *On*-Bu, *Ot*-Bu) together with the *trans-cis* photoisomerization scheme.

Azo-doped samples were prepared by adding in turn one of the eight azo-derivatives, at 1% and 7% mole fraction, to a solution of CSL spin probe in 5CB at a concentration of $6 \times 10^{-4} g_{CSL}/g_{5CB}$. Given the good solubility of the spin probe and of the azo-derivatives in 5CB at the concentrations studied, mechanical mixing at a temperature slightly above T_{NI} was sufficient to prepare uniform samples without adding any solvent.

Fresh samples not requiring photoisomerization (*trans* isomers) were inserted into glass capillaries of 1.8 mm internal diameter and stored in the dark at room temperature until ESR measurements. To obtain the *cis* isomers, samples were treated as described later in this section. Immediately after the isomerization, they were inserted into the capillaries and ESR spectra were recorded. We recorded ESR spectra on heating taking the samples from the nematic (N) to the isotropic (I) phase, in a range of about 20 K around T_{NI} , with the experimental set up described in Section 2.3.1.

The *trans-cis* photoisomerization reactions (see Figure 3.7) were carried out by exposing the samples in a quartz cuvette to UV-light ($\lambda = 365 \text{ nm}$) with a UVGL-58 MINERALIGHT Lamp (UVP). During the exposure, we recorded several UV-visible absorption spectra with a Cary 1E (Varian) spectrophotometer to follow the *trans-cis* photoisomerization. UV-visible spectra were taken before any irradiation and after different times of exposure, diluting each sample in cyclohexane to achieve a concentration of the azo-derivative of $2.5 \times 10^{-4} \text{ M}$. The *trans* isomer spectra

exhibited features characteristic of *trans*-azobenzene type molecules, i. e. a strong absorption band at about 340 nm, due to $\pi \rightarrow \pi^*$ transition, and a much weaker band centered at 450 nm, due to $n \rightarrow \pi^*$ transition. Irradiation at 365 nm caused a decrease of the $\pi \rightarrow \pi^*$ band intensity and a build-up of the $n \rightarrow \pi^*$ band, which was slightly shifted toward shorter wavelengths. This indicated that the isomerization was taking place. We considered the process successful when we could not observe any further change by comparing two consecutive UV-visible spectra (see Figure 3.8). This typically required between 10 and 24 hours, depending on the azo-derivative concentration. After the ESR measurements of the samples doped with the *cis* azo-derivatives, a further UV-visible absorption spectrum was taken and compared to the one taken immediately before the ESR measurements. In all the cases, these spectra were essentially identical, indicating that the *cis* isomers did not significantly reverse to the *trans* configuration during the ESR spectra acquisition.

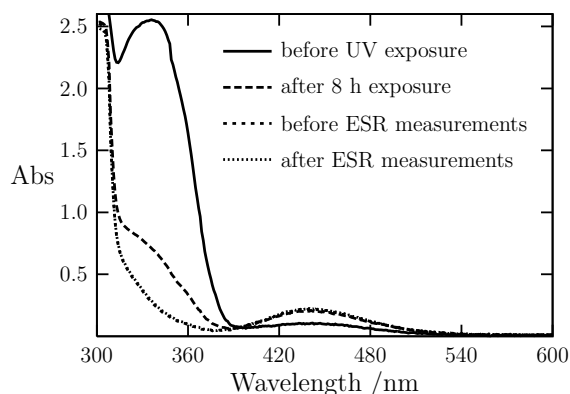


Figure 3.8: Typical absorption spectra recorded after different times of UV exposure. Example relative to 5CB doped with 4-*Ot*-Bu-phenylazobenzene dissolved in cyclohexane (see text for details).

The presence of non-mesomorphic solutes in a nematic LC can lead, in a temperature range close to the T_{NI} , to the appearance of a biphasic region, consisting of both N and I phases which coexist in equilibrium [58–60]. This actually seemed to be the case for some of the samples doped with the *cis* azo-derivatives, whose ESR spectra exhibited a line shape that could be attributed to the superposition of two different spectra, one characteristic of a nematic phase and the other of an isotropic environment. To verify for all the samples the existence and the limits of the biphasic region, if any, we also performed a series of polarizing microscope observations under crossed polarizers. Every LC mixture was held in a flat quartz cell with 25 μm spacing. The inner surface of the cell was coated with polyvinyl formal and then rubbed to achieve homogeneous alignment of the LC molecules parallel to the rubbing direction. The sample was then irradiated with UV-light ($\lambda = 365 \text{ nm}$) to cause the isomerization, when needed, and examined with a ORTHOPLAN Leitz polarizing microscope equipped with a thermostating stage, placing the cell with the LC director at 45° with respect to the polarizers. For each system, the temperature range explored was the same considered in the ESR measurements. These investigations

confirmed that pure 5CB and samples doped with *trans* isomers completely turned, at the transition, into the I phase, while mixtures containing *cis* isomers exhibited, close to the T_{NI} , a biphasic region in which both N and I phases coexisted (see Figure 3.9 for an example relative to 5CB doped with *cis* 4-*On*-Bu-phenylazobenzene at 7% mole fraction).

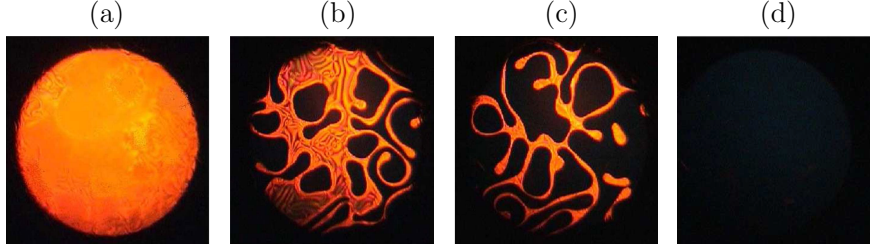


Figure 3.9: Pictures of 5CB doped with *cis* 4-*On*-Bu-phenylazobenzene at 7% mole fraction, taken with the cell between crossed polarizers (see text for details). Bright and dark areas correspond to the nematic and the isotropic phases, respectively. We show the sample at the highest temperature at which it is still completely nematic (a: $T = 286.7$ K), in the biphasic region (b: $T = 289.8$ K; c: $T = 290.8$ K) and at a temperature at which it is completely isotropic (d: $T = 292.2$ K).

3.3.2 Fitting Procedure for ESR Spectra

The ESR spectra of the spin probe showed the expected features for CSL moving in a fluid environment with a certain degree of order, similar to those observed in previous studies of cyanobiphenyl nematics or similar materials [27, 61].

The ESR line shapes were simulated in a global-target-analysis, i. e. optimizing the fit parameters for a series of spectra at the same time, using the method described in Section 2.3.2 and assuming a monodomain model.

In a series of preliminary fits we considered as temperature dependent variable parameters the order parameter $\langle P_2 \rangle$, the perpendicular component of the rotational diffusion tensor R_{\perp} , the inhomogeneous line width T_2^{*-1} and the ratio of spinning and tumbling diffusion coefficients $R_r = R_{\parallel}/R_{\perp}$ (introduced to minimize the correlation among some of the parameters [27]). The results obtained from this preliminary analysis showed that the dynamics seemed to be essentially independent of the nature, the configuration and the concentration of the different azo-derivatives. In particular, the R_{\perp} behavior could be described, for all the N or I phases, by a simple Arrhenius-type temperature dependence

$$R_{\perp}^{(i)} = R_0^{(i)} \exp[-E^{(i)}/RT] \quad (3.1)$$

where $i = N$ or I . Furthermore, R_r was found to be essentially temperature independent, with values very close to those obtained for the pure 5CB, that is, $R_r^{(N)} = 7.1$ and $R_r^{(I)} = 9.9$. Therefore, in the final fits, it appeared reasonable to assume, for all the different nematic or isotropic regions, a common temperature dependence of

the dynamic parameters and the globalization scheme adopted can be summarized as follows:

1. Nematic Phase

ESR spectra relative to the N phase were analyzed considering as variable parameters the order parameter $\langle P_2 \rangle$, the inhomogeneous line width T_2^{*-1} and the coefficients $R_0^{(N)}$ and $E^{(N)}$ describing the Arrhenius behavior of $R_{\perp}^{(N)}$. $R_r^{(N)}$ was kept fixed to the value obtained in the preliminary fits to further reduce the correlations between the parameters.

2. Isotropic Phase

To model the line shapes in the I phase, $\langle P_2 \rangle$ was kept fixed to zero and, similarly to the N phase, $R_r^{(I)}$ was kept fixed to the value obtained in the preliminary fits. The variable parameters were then the inhomogeneous line width, $R_0^{(I)}$ and $E^{(I)}$.

3. Coexistence Region

ESR spectra of samples that showed, at the polarizing microscope, a biphasic region in a certain range of temperatures, were fitted to a weighted sum of two spectra, one for each phase, both modeled with the same set of parameters described above. The weight of each spectrum was assumed to be proportional to the fraction of the nematic (f_N) or isotropic (f_I) phase present in the sample, with $f_N + f_I = 1$.

In Figure 3.10 we show typical experimental ESR spectra and fits of a sample doped with *cis* 4-CH₃-phenylazobenzene at 7% mole fraction at temperatures representative of the N phase, of the I phase and of the biphasic region. The very good fits obtained confirmed the validity of the model.

The fraction of each phase could be estimated by using the lever rule in a temperature-composition phase diagram [54]. We illustrate the method employed in Figure 3.11, where we report, as an example, the phase diagram of 5CB doped with 4-*On*-Bu-phenylazobenzene in its *cis* form.

By inspection of the ESR line shapes we have detected the biphasic region limits, marked in Figure 3.11 as dots on the isopleth lines at 1% and 7% mole fraction, and we have then identified the α and β lines (assumed to be straight lines at low solute concentration) [52, 59], which represent the composition of the N and the I coexisting phases, respectively. Considering for example the heating process of the nematic system at 7% mole fraction, at T_{α} the I phase begins to appear while at T_{β} the N phase completely vanishes. At every temperature T_j inside the coexistence range, we drew the corresponding tie line (of total length $l_N + l_I$) and applied the lever rule: $l_I f_N = l_N f_I$. We thus calculated the values of $f_N = l_N / (l_N + l_I)$ and $f_I = l_I / (l_N + l_I)$, which represent the relative amount of N and I phase in equilibrium within the biphasic region. Moreover, the intersection between the α and β lines with the tie line allowed to find out the composition of the nematic, $x^{(N)}$, and isotropic, $x^{(I)}$, coexisting phases, respectively.

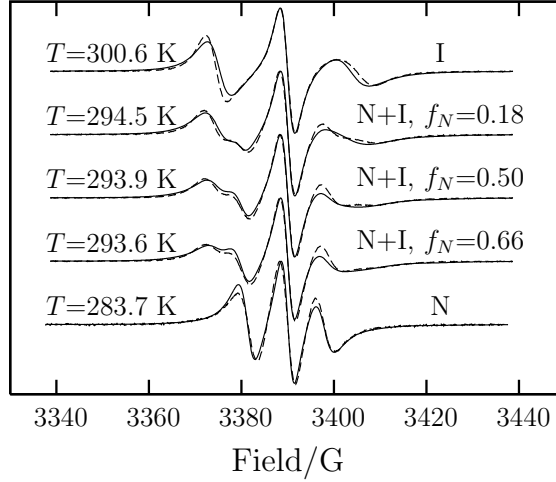


Figure 3.10: Experimental ESR spectra (dashed line) and fits (solid line) of 5CB doped with *cis* 4-CH₃-phenylazobenzene at 7% mole fraction. For each spectrum, the temperature and the corresponding phases are indicated. For the spectra recorded in the biphasic region the fraction of the nematic phase f_N is also reported.

3.3.3 Results: T_{NI} , order and dynamics

To establish a uniform notation for the different samples, hereafter we shall refer to T_{NI} as to the highest temperature at which the N phase is still present in the sample, to ΔT_{NI} as to the difference between the T_{NI} of the system considered and that of the pure 5CB and to ΔT_{coex} as to the range of the biphasic region of the mixtures containing the *cis* isomers.

We found, in particular, ΔT_{NI} values for the *trans* isomers in the range -0.2 to -1.6 K at 1% mole fraction, increasing, in absolute value, at 7% to the range -0.7 to -8.0 K and, for the *cis* isomers, in the range -1.7 to -3.7 K and -7.9 to -19.5 K at 1% and 7% mole fraction, respectively. The ΔT_{coex} of the *cis*-doped samples, also shown in Table 3.1, increased with the azo-derivative concentration from 0.2 to 0.6 K at 1% to the range 0.4 to 8.3 K at 7% and was wider in samples with larger ΔT_{NI} .

In Figure 3.12 (a) we show our results for the order parameter $\langle P_2 \rangle$ of the spin probe against reduced temperature $T^* = T/T_{NI}$ in samples containing the *trans* isomers at 1% mole fraction. As we can see, the values are nearly identical to those relative to the pure 5CB and this can be also observed at the higher 7% mole fraction (Figure 3.12 (b)), with only a very small decrease of the $\langle P_2 \rangle$ values in the samples containing the *Ot*-Bu and F substituted azo-derivatives.

For the *cis* isomers, the deviations are relatively larger. As shown in Figure 3.13 (a), even at 1% mole fraction all the samples show a degree of order lower than that of the pure 5CB and this decrease becomes even more evident at 7% mole fraction for all the azo-derivatives (see Figure 3.13 (b)) and is particularly large in samples containing the *On*-Bu and *Ot*-Bu substituted azo-derivatives. The $\langle P_2 \rangle$ temperature dependence, in this latter case (Figure 3.13 (b)), seems to have

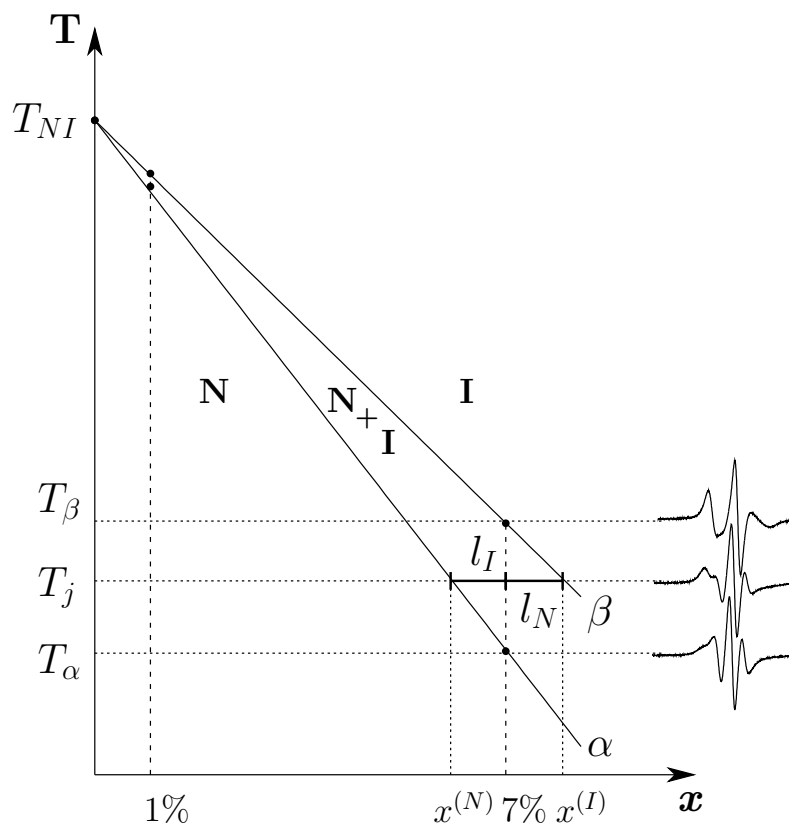


Figure 3.11: Temperature-composition phase diagram of 5CB, doped with *cis* 4-*On*-Bu-phenylazobenzene, showing the nematic–isotropic coexistence region. Also shown are the experimental ESR spectra, at 7% mole fraction, acquired at the limiting temperatures (T_{α} and T_{β}) and approximately in the middle (T_j) of the biphasic region.

a peculiar trend. In the temperature range far from the corresponding T_{NI} , the order parameter of the various samples decreases with increasing temperature but, approaching the T_{NI} , the degree of order exhibits a small increase and then it decreases again, eventually showing the discontinuity characteristic of the N–I phase transition, once the T_{NI} is reached. The reason for this behavior is related to the formation of the biphasic region and on the consequent partition of the *cis* azo-derivatives within the two phases. To clarify this point, it is useful to refer again to the phase diagram in Figure 3.11, considering the isopleth at 7% and a heating process raising the system temperature from T_{α} to T_{β} . Within the biphasic region ($T_{\alpha} < T < T_{\beta}$), the solute is distributed between the N and the I phase in different proportions. At the generic temperature T_j , for instance, the *cis* azo-derivative mole fraction dissolved into the N phase, $x^{(N)}$, is smaller than the nominal concentration of 7%. Thus, in the coexistence region, the order of the N phase present in the system is the result of the competition of two opposite temperature-related processes. On the one hand, in fact, increasing the temperature causes a higher

Table 3.1: Effect of the *trans* and *cis* *p*-azobenzene derivatives at 1% and 7% mole fraction on the nematic phase stability^a.

R	T_{NI} /K				ΔT_{NI} /K				ΔT_{coex} /K		
	<i>trans</i>		<i>cis</i>		<i>trans</i>		<i>cis</i>		<i>cis</i>		
	1%	7%	1%	7%	1%	7%	1%	7%	1%	7%	
O <i>t</i> -Bu	307.3	301.3	304.8	289.0	-1.2	-7.2	-3.7	-19.5	0.6	8.3	
OCH ₃	308.3	307.5	306.0	289.5	-0.2	-1.0	-2.5	-19.0	0.4	6.0	
O <i>n</i> -Bu	308.1	307.8	304.9	291.9	-0.4	-0.7	-3.6	-16.6	0.6	5.2	
CH ₃	308.1	306.4	305.6	294.5	-0.4	-2.1	-2.9	-14.0	0.5	1.9	
F	307.4	302.7	305.8	295.6	-1.1	-5.8	-2.7	-12.9	0.3	0.8	
H	306.9	300.5	305.7	295.7	-1.6	-8.0	-2.8	-12.8	0.2	0.7	
CF ₃	307.5	302.0	306.8	299.5	-1.0	-6.5	-1.7	-9.0	0.2	0.4	
Br	308.0	305.2	305.9	300.6	-0.5	-3.3	-2.6	-7.9	0.2	0.5	
5CB	308.5										

^a Abbreviations:

T_{NI} , nematic-isotropic transition temperature; $\Delta T_{NI} = T_{NI,5CB+azo} - T_{NI,5CB}$, shift of the T_{NI} relative to the pure 5CB;

ΔT_{coex} , nematic-isotropic coexistence range.

disorder of the N phase and a lower order parameter but, on the other hand, it is the driving force for the diminishing of the *cis* isomer concentration in the nematic fraction, resulting in a smaller perturbation of the system and thus in an increase in the degree of order. The $\langle P_2 \rangle$ behavior shown in Figure 3.13 (b) is then the result of these two contributions. The recovery of meaningful and uncorrelated values of the nematic parameters from the fit was not possible when the nematic contribution to the biphasic ESR spectrum became too weak. Therefore, in Figure 3.13 (b), the $\langle P_2 \rangle$ values of samples with a fraction f_N lower than about 0.15 are not shown.

Such a peculiar trend of the order parameter is similar to that obtained by Polson and Burnell [62] in a Monte Carlo simulation study, investigating the $\langle P_2 \rangle$ behavior at the beginning of the nematic-isotropic coexistence region of a binary LC mixture with a Lebwohl-Lasher model. Experimentally not much is available. However, in an NMR study of 5CB deuterated in different positions, Beckmann *et al.* [63] found that, in the presence of an unknown impurity at low concentration (traces), the nematic order parameter was almost constant in a portion of a relatively narrow coexistence region. It is not too surprising that, in that case [63], in the two-phase region the order parameter has been found to be a universal function of T/T_{NI} . However, in our case, at 7% of the *cis* isomer (Figure 3.13 (b)), it is no longer possible to assume the order parameter as a universal function of T/T_{NI} , since it is quite evident that, already before the occurrence of the two-phase region, the order parameter is depressed by the presence of the azo-derivative beyond the expected value.

As previously discussed, the spin probe dynamics in the presence of the azo-derivative is essentially unchanged with respect to that observed in the pure 5CB. In particular, it was found to have a different trend in the N and in the I phase,

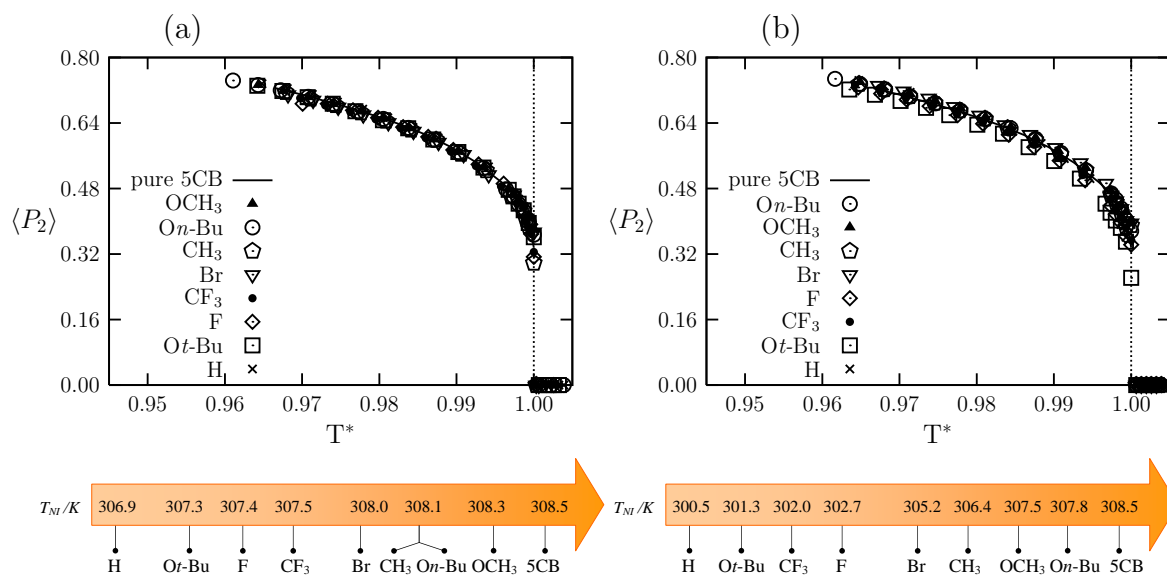


Figure 3.12: Order parameter $\langle P_2 \rangle$ of the spin probe against reduced temperature T^* for the samples doped with the *trans* azo-derivatives at (a) 1% and (b) 7% mole fraction, compared to the pure 5CB. The sequence of the substituents, from bottom to top in the key, is in order of increasing T_{NI} , as listed also in the arrow-shaped scheme.

which can be summarized as follows:

- Nematic Phase

The temperature range considered for the N phases was 274.2 to 308.5 K. The best fit parameters of the $R_{\perp}^{(N)}$ Arrhenius-type temperature dependence are $R_0^{(N)} = (6 \pm 2) \times 10^7 \text{ ns}^{-1}$ and $E^{(N)} = 53 \pm 2 \text{ kJ/mol}$. $R_r^{(N)} = 7.1$.

- Isotropic Phase

For the I phases, the temperature range was 280.7 to 320.5 K, with $R_r^{(I)} = 9.9$ and best fit parameters $R_0^{(I)} = (3 \pm 1) \times 10^5 \text{ ns}^{-1}$ and $E^{(I)} = 41 \pm 2 \text{ kJ/mol}$.

3.3.4 Discussion

It is interesting to try and relate the changes induced by the solute on $\langle P_2 \rangle$ and T_{NI} from those observed for the pure 5CB to the solute-solvent interactions occurring between the different azo-derivatives and the LC host and here we wish at least to start tackling the problem. We begin discussing the overall effect of the various solutes on the ΔT_{NI} and the $\langle P_2 \rangle$ dependence on T^* . We then offer a detailed comparison of the differences in the ΔT_{NI} , due to the type of azo-derivative, for each isomer configuration and at the two mole fractions studied. Considerations based on solute shape and size (essentially “short-range” interactions) that are able to rationalize, at least in part, the N phase stability sequence of the various *cis* isomers are not valid for the *trans*, which exhibit quite a different sequence. To investigate the role of interactions at longer range, we then proceed to compare the

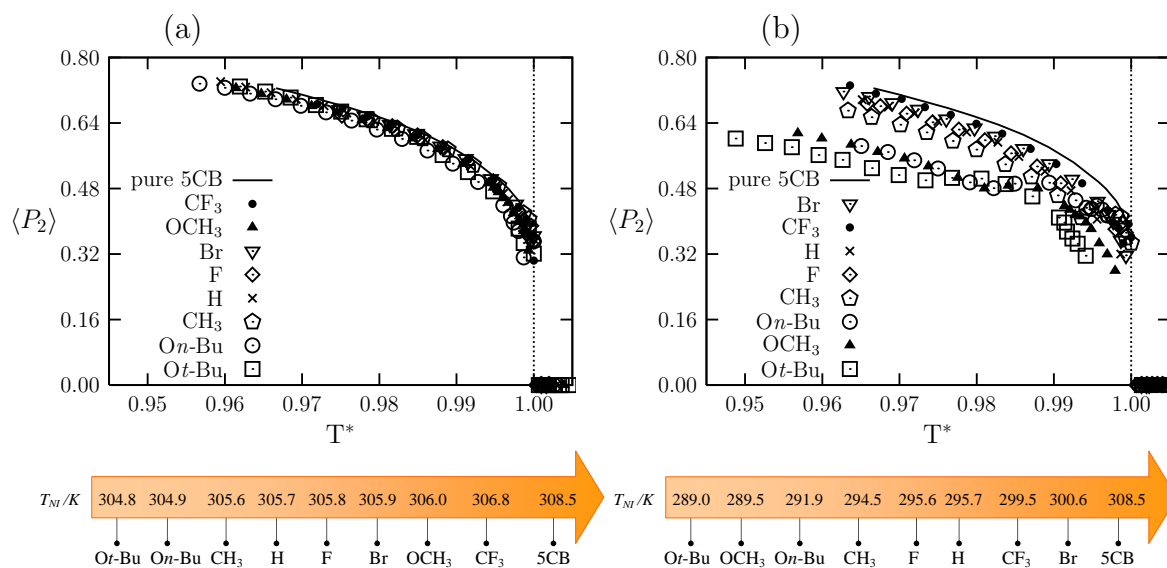


Figure 3.13: Order parameter $\langle P_2 \rangle$ of the spin probe against reduced temperature T^* for the samples doped with the *cis* azo-derivatives at (a) 1% and (b) 7% mole fraction, compared to the pure 5CB. The sequence of the substituents, from bottom to top in the key, is in order of increasing T_{NI} , as listed also in the arrow-shaped scheme.

electrostatic properties of the solutes with those of the solvent, beginning with the molecular dipole and quadrupole and then performing a qualitative comparison of the electrostatic potential at the molecular surface.

By recalling the results presented in the previous section, a first, general observation is that the *cis* isomers (V-shaped) always produce a shift of the nematic–isotropic transition to a lower temperature larger than that of the *trans* (rod-like).

At 1% and 7% *trans* and at 1% *cis*, the destabilization causes only a T_{NI} shift while the $\langle P_2 \rangle$ dependence on T^* is either completely unaffected (*trans* isomers at both mole fractions, Figure 3.12), or shows only a small decrease (*cis* isomers at 1%, Figure 3.13 (a)). At 7% *cis*, instead, the shift to a lower temperature is no longer able to “compensate” the destabilization introduced by the azo-derivatives so that also the order of the phase is significantly depressed, compared to that of the pure 5CB, with relatively large differences among the $\langle P_2 \rangle$ vs. T^* plots (Figure 3.13 (b)). By listing the derivatives, starting from the one which causes the largest decrease of $\langle P_2 \rangle$, we have the following sequence: *Ot*-Bu, *OCH*₃, *On*-Bu, *CH*₃, *F*, *H*, *Br* and *CF*₃. Interestingly, if we consider the T_{NI} shifts, again starting from the largest one, we have almost the same sequence, apart from the inversion of *CF*₃ with *Br*. At 1% *cis*, we also observe a quite similar result: *Ot*-Bu, *On*-Bu, *CH*₃, *H*, *F*, *Br*, *OCH*₃ and *CF*₃. The sequence of stability of the *trans* isomers is, instead, quite different from that of the *cis*. At 7% it is: *H*, *Ot*-Bu, *CF*₃, *F*, *Br*, *CH*₃, *OCH*₃ and *On*-Bu and it remains similar at 1%: *H*, *Ot*-Bu, *F*, *CF*₃, *Br*, *CH*₃, *On*-Bu and *OCH*₃.

We can now summarize the above observations. The *cis* isomers determine an overall larger destabilization and, within the *cis* series, it seems that the destabiliz-

ing effect due to the bulkiness of the substituent is dominant (*O**t*-Bu, *O**n*-Bu and OCH₃) and, at 7% mole fraction, it affects not only the shift of the T_{NI} but also the order of the phase in a very similar way. This is compatible with the idea that the main influence on the N phase stability is played by the solute molecular shape and is also in agreement with experimental studies and simulations dealing with the orientational ordering of solutes in nematic LC and hinting that the short-range interactions, which depend on the size and on the molecular shape, strongly influence the orientational behavior of molecules in nematic solvents [56, 64]. Clearly, these considerations of size are not sufficient by themselves to account for the sequence of stability observed, otherwise the unsubstituted azobenzene and the 4-F-phenylazobenzene, in the sequence of the *cis* at 7%, would have occupied the last position and the CH₃ azo-derivative, having approximately the same size as the Br or the CF₃, would have shown a similar behavior. Moreover, in the case of the *trans* isomers, it seems that the destabilizing contribution due to the larger substituents is less important since, e.g., the unsubstituted azobenzene and the *O**t*-Bu azo-derivative affect the T_{NI} in a similar way. We also observe that, since the solute has a size and shape approximately corresponding to that of the solvent, the N phase is almost unaffected by its presence: indeed at both the concentrations studied, the *trans* *O**n*-Bu-phenylazobenzene induces only a small T_{NI} shift.

Another relevant contribution to the orientational ordering involves long-range, solute-solvent electrostatic interactions [56, 64–66]. To investigate their role, we have calculated and compared the dipole moment and the principal components of the quadrupole tensor of both the solvent and the solute molecules. For all the compounds studied, we performed a preliminary quantum mechanical DFT B3LYP/6-31G** geometry optimization and vibrational frequency calculation. Then, by using this optimized geometry, we determined, using the more extended “augmented correlation-consistent polarized valence orbital basis set of triple zeta quality” (AUG-cc-PVTZ), the dipole and quadrupole moments and the atomic point charges with the Merz-Singh-Kollman scheme, considering the additional constraint of reproducing the total molecular dipole moment [67]. The results of these calculations are reported in Table 3.2 and Table 3.3. Unfortunately, it was not possible to find a simple correlation between the degree of destabilization caused by the various azo-derivatives and their dipole moments or quadrupole tensor principal values, also when comparing them to those of the 5CB liquid crystal. In a way this is not surprising, since for molecules in close contact like those in a condensed phase, the full charge distribution should be considered [68] and it is not sufficient to simplify the electrostatic host-guest interactions using low rank multipole terms.

Table 3.2: Dipole moment (μ) and dipole components (μ_i) of the various molecular species used in this study^a

R	<i>trans</i>				<i>cis</i>			
	μ	μ_x	μ_y	μ_z	μ	μ_x	μ_y	μ_z
<i>Ot</i> -Bu	1.66	-0.96	-0.11	1.35	3.26	-2.24	-2.37	0.15
OCH ₃	1.88	1.43	-1.23	0.00	3.89	-2.55	-2.85	0.71
<i>On</i> -Bu	2.50	2.27	-1.05	0.00	4.39	3.61	2.44	0.55
CH ₃	0.81	-0.81	-0.06	0.00	3.63	-1.10	-3.45	0.21
F	1.52	-1.51	0.21	0.00	2.34	0.69	-2.23	0.23
H	0.00	0.00	0.00	0.00	3.17	0.00	-3.17	0.00
CF ₃	3.64	3.63	0.19	-0.08	2.66	-1.96	-1.78	-0.24
Br	1.89	-1.89	0.14	0.00	2.39	0.54	-2.31	0.31
5CB	6.32	6.26	0.61	0.64				

^aValues calculated at B3LYP/6-31G** – AUG-cc-PVTZ level in the molecular inertial frame and expressed in Debye.

Table 3.3: Quadrupole components Q_{ii} of the various molecules used in this study^a

R	<i>trans</i>			<i>cis</i>		
	Q_{xx}	Q_{yy}	Q_{zz}	Q_{xx}	Q_{yy}	Q_{zz}
<i>Ot</i> -Bu	13.7	0.2	-13.9	13.4	-15.8	2.4
OCH ₃	13.6	-0.1	-13.5	12.2	-11.3	-0.9
<i>On</i> -Bu	15.1	-2.4	-12.7	16.8	-16.2	-0.6
CH ₃	12.9	-0.3	-12.6	9.8	-8.8	-1.0
F	1.1	6.6	-7.6	11.5	-12.7	1.2
H	10.9	1.1	-12.0	9.3	-7.8	-1.5
CF ₃	0.0	7.3	-7.3	-17.0	13.4	3.6
Br	5.9	3.7	-9.6	12.2	-14.0	1.8
5CB	-35.8	24.1	11.7			

^aValues calculated at B3LYP/6-31G** – AUG-cc-PVTZ level in the quadrupolar frame and expressed in Debye Å.

The importance of the role played by long-range interactions on the molecular orientation mechanism in nematics has been discussed in several works, particularly by Burnell *et al.* (see e.g. [66] and refs. therein), and it has been related to the average electric field arising from the charge distribution of the solvent molecules surrounding the solute and to the corresponding field gradient, experienced by the solute. Here, for each molecular species studied, we have calculated the electrostatic potential at the molecular surface (EP map) defined by the overlap of the Van der Waals spheres centered on each atom, using the simple Coulombic relation

$$V(\mathbf{r}) = \sum_i q_i \frac{1}{|\mathbf{r} - \mathbf{r}_i|} \quad (3.2)$$

where \mathbf{r} is the position on the molecular surface and q_i is the point charge located on the i -th atom at \mathbf{r}_i .

We now wish to perform a qualitative comparison between the EP map of 5CB and the map of each azo-derivative looking for features which could hint at a favorable or disruptive short-range arrangement of the solute-solvent pair and thus indirectly be related to a higher or a lower degree of destabilization for that derivative.

In Figure 3.14, we compare the potential map of 5CB with the *trans* isomers and we consider the two extreme azo-derivatives in the sequence of stability. We see that the EP map of 5CB (Figure 3.14 (a)) exhibits a strong negative site located on the CN group and a positively charged region on the alkyl chain. The EP map of the 4-*n*-Bu-phenylazobenzene (lowest destabilization, Figure 3.14 (b)) also exhibits quite a well defined positive region on the *n*-Bu group and a negative region centered on the azoic group. The similarity of shapes and EP maps hints that the introduction of this solute should be relatively innocuous on the local environment. The EP map of the unsubstituted azobenzene (highest destabilization, Figure 3.14 (c)) appears instead to be quite different from that of 5CB, being symmetrical and without distinct regions of opposite charge, suggesting a local perturbation of the solvent-solvent interactions. By considering these two compounds as the “limiting” cases for the *trans* azo-derivatives and by ordering all the other derivatives according to the intermediate features of their map, it is actually possible to recover the same sequence of stability observed experimentally, thus confirming our assumption that azo-derivatives with an EP map more similar to that of 5CB will introduce a lower degree of destabilization.

This qualitative argument is tenable only for molecules of similar shape, where the electrostatic contribution can operate a second level selection. Thus a direct comparison of the EP map of 5CB with the maps of the *cis* azo-derivatives (Figure 3.14 (d) and 3.14 (e)) would be more difficult due to their bent shape. However, it is still possible to observe analogous features among the *cis* azo-derivatives EP maps which can be consistently related to the different degrees of destabilization introduced in the N phase. The EP maps of the *cis* azo-derivatives responsible of the lowest and the highest degree of destabilization at 7% mole fraction are shown in Figure 3.14 (d) and 3.14 (e). In the first case (Br azo-derivative), the substituent exhibits EP values close to zero, while the atoms closest to the azoic group have

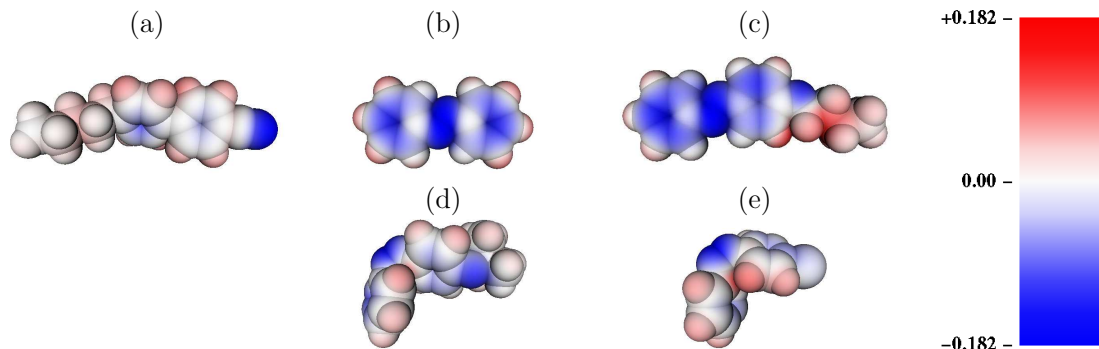


Figure 3.14: Electrostatic potential at the molecular surface for the 5CB (a), *trans* 4-*O**n*-Bu-phenylazobenzene (b), *trans* azobenzene (c), *cis* 4-Br-phenylazobenzene (d) and *cis* 4-*O**t*-Bu-phenylazobenzene (e). Color coded according to the palette (units $4\pi\epsilon_0e/\text{\AA}$). Geometry and charges obtained at B3LYP/6-31G** – AUG-cc-PVTZ level.

strongly positive values. In the second (*O**t*-Bu azo-derivative), we observe a strong negative site on the *tert*-butoxy group and a relatively neutral region on the aromatic carbons bound to the azoic group. Also in this case, we ordered the other *cis* azo-derivatives according to their map and we obtained the same sequence of stability observed experimentally.

3.3.5 Conclusions

We have studied a series of eight closely related azobenzene derivatives, in their *trans* and *cis* form, dissolved at a mole fraction of 1% and 7% in the nematic 5CB liquid crystal. One of the aims of our study was to investigate if *trans* and *cis* azo-derivatives simply act on a nematic solvent by shifting T_{NI} [44, 47] or if more subtle effects come into play [24, 25]. We have found that the presence of the azo-derivative caused, in all the present cases, a depression of the T_{NI} . The *cis* isomers reduced the order of the 5CB nematic phase and induced a larger T_{NI} shift with respect to the *trans* isomers. At higher mole fraction, we observed an analogous behavior with larger effects. At both concentrations of the *trans* isomers and at 1% of the *cis*, the T^* dependence of our spin probe order parameter remained unchanged by the addition of the solute with respect to that of the pure 5CB. At 7% *cis* isomers, instead, the $\langle P_2 \rangle$ decreased significantly, indicating a more unexpected and profound change of the functional dependence of $\langle P_2 \rangle$ on the temperature and on the chemical nature of the azo-derivative. In the presence of the *cis* isomers the samples showed a region of phase separation which was almost negligible at 1% but became quite evident at 7% and was found to be wider in samples with larger T_{NI} shifts.

The $\langle P_2 \rangle$ recovered after suitable allowance for the biphasic region in simulating the probe spectra showed a peculiar dependence on T^* with the order parameter slightly increasing as the system enters the biphasic region. It is important to notice that, even setting aside the region very close to T_{NI} , the order parameter of

the *cis* isomers showed marked changes for the different substituents, with a more pronounced effect for the alkoxy groups.

Surprisingly, the rotational dynamics of the probe, and thus indirectly the local rotational microviscosity, appeared to be unaffected by the nature, the isomer type or the concentration of the different azo-derivatives.

We discussed also the possibility of relating the different degrees of destabilization to long-range electrostatic interactions of 5CB with the different azo-derivatives. No simple correlation was found with the low rank electrostatic terms (molecular dipole or quadrupole). However, interesting structure-stability correlations were found considering the full electrostatic potential maps of 5CB and of the different solutes, indicating that, at least for comparable shapes and sizes, an azo-derivative with a potential map more similar to that of the 5CB will introduce a lower degree of destabilization in the phase.

Even without this full understanding of the effects of the solute structure on the nematic solvent, we believe that our findings, i.e. that (i) the changes in order induced by the *cis* isomers go beyond a simple shift in transition and that (ii) it is possible to obtain substituent dependent differences of up to 25% in the ordering, should be of interest in photonic applications based on the azobenzene photoresponsive properties.

3.4 *p,p'*-disubstituted Azobenzene Derivatives

We have extended the study presented in the previous section to disubstituted mesogenic azo-benzenes having a structure similar to that of the 4-*O**n*-Bu-phenylazobenzene (Figure 3.7). This choice is based on the findings reported in Section 3.3.3, that is, that the 4-*O**n*-Bu-phenylazobenzene is the compound that in its *trans* configuration induces only a slight destabilization of the N phase without affecting the $\langle P_2 \rangle$ behavior, whereas its *cis* isomer induces large and profound changes both in the T_{NI} and in the nematic order. The chemical structure of the two azo-compounds (AB_2R , with $R = NO_2$ and OCH_3 [69, 70]) used in this investigation is shown in Figure 3.15.

These derivatives have been synthesized by our colleagues of the Department of Organic Chemistry at the University of Barcelona.

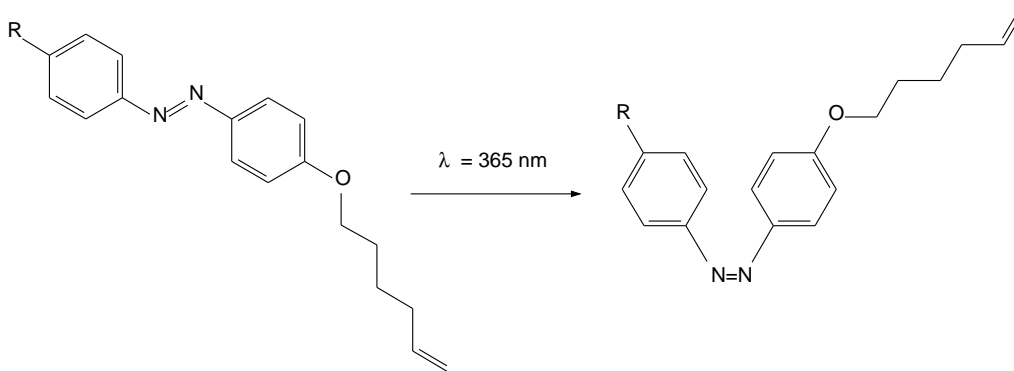


Figure 3.15: Chemical structure of the disubstituted photoactive units ($R = NO_2$, OCH_3) together with the *trans-cis* photoisomerization scheme.

The samples were prepared by adding in turn one of the two azo-derivatives, at 3% and 8% mole fraction, to a solution of 5CB/CSL ($g_{CSL}/g_{5CB} = 6 \times 10^{-4}$), following the method already described in Section 3.3.1. In summary, we performed the *trans-cis* isomerization by exposing the samples to UV-light and monitored the process with UV-visible absorption spectra (Figure 3.16). Both for the *trans* and for the *cis* doped samples, the ESR spectra were acquired on a heating stage from the N to the I phase. An additional UV-vis spectrum of the *cis* doped samples was taken after the ESR measurements and it indicated that in all the cases the inverse isomerization reaction did not take place (Figure 3.16).

Polarizing microscope observations, performed in a temperature range consistent with the one explored during the ESR measurements, confirmed the presence of a biphasic region in the samples doped with *cis* AB_2OCH_3 , whereas no coexistence region was observed in the other cases.

The fitting procedure adopted followed the globalization scheme proposed in Section 3.3.2. Also in this case, to model the ESR spectra relative to the two-phase region, we used f_N and f_I as weighting parameters for the nematic and isotropic contribution, respectively. The values of f_N and f_I were obtained from the temperature-composition phase diagram in Figure 3.17 by using the lever rule.

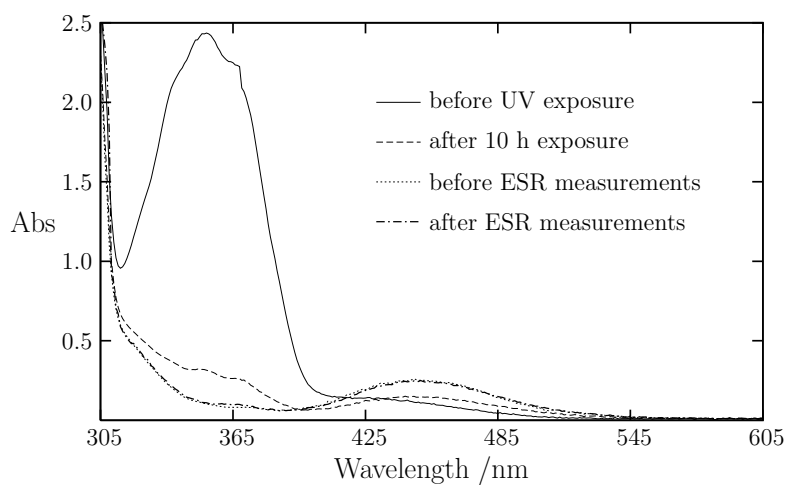


Figure 3.16: UV-visible absorption spectra for checking both the photoisomerization process before the ESR measurements and the stability of the *cis* configuration after the ESR measurements. Exemple relative to 5CB doped with AB₂OMe (8%) dissolved in cyclohexane.

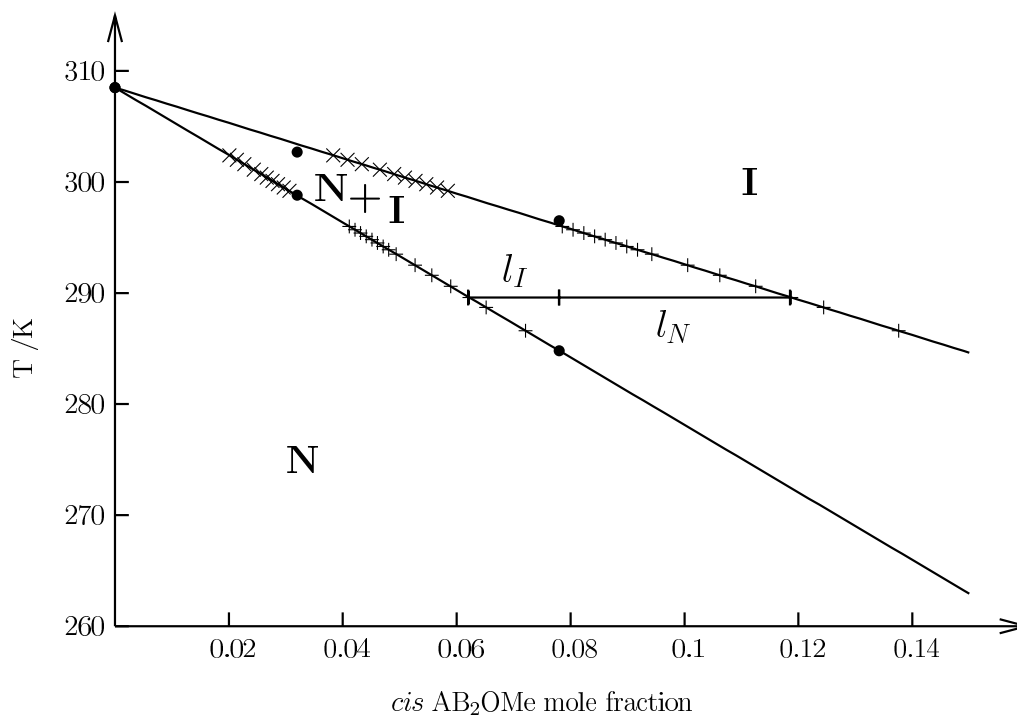


Figure 3.17: Temperature-composition phase diagram of 5CB, doped with *cis* AB₂OMe, showing the nematic–isotropic coexistence region.

3.4.1 Results and Discussion: T_{NI} , order and dynamics

In Table 3.4, the temperature transition of the various samples studied are reported. Accordingly to the definition given in Section 3.3.3, we shall refer to T_{NI} as to the highest temperature at which the N phase is still present in the sample, to ΔT_{NI} as to the difference between the T_{NI} of the system considered and that of the pure 5CB and to ΔT_{coex} as to the range of the biphasic region of the mixtures containing *cis* AB₂OCH₃.

We observe that *trans* AB₂NO₂ does not affect the N phase stability independently of its concentration and that *trans* AB₂OCH₃ induces a clear stabilization of the ordered phase, which increases with the azo-derivative concentration. This behavior is found to be common in LC mixtures containing mesogenic solutes [71–74].

As expected, the *cis* form of AB₂OCH₃ destabilizes the N phase, leading to a lowering of the T_{NI} , with ΔT_{NI} values increasing (in absolute value) as the solute concentration is raised. This behavior is comparable to that observed for the *cis* 4-*O*-*n*-Bu-phenylazobenzene (see Table 3.1). The occurrence of a biphasic region, in which the N and the I phase coexist in equilibrium, is also observed near the T_{NI} (see also Figure 3.17). What is actually unexpected is the effect on the T_{NI} played by the *cis* isomer of AB₂NO₂. The N phase stability is, in fact, essentially unaffected by the presence of this solute at both concentrations. Moreover, since both the *trans* and *cis* forms of AB₂NO₂ do not induce any change in the T_{NI} , it follows that it is not possible to drive an order-disorder transition by photoisomerizing this compound in a 5CB matrix.

Table 3.4: Effect of the *trans* and *cis* *p-p'*azobenzene derivatives at 3% and 8% mole fraction on the nematic phase stability^a.

R	T_{NI} /K				ΔT_{NI} /K				ΔT_{coex} /K	
	<i>trans</i>		<i>cis</i>		<i>trans</i>		<i>cis</i>		<i>cis</i>	
	3%	8%	3%	8%	3%	8%	3%	8%	3%	8%
NO ₂	308.5	308.4	308.5	308.4	–	–0.1	–	–0.1	–	–
OCH ₃	309.1	310.8	302.1	296.3	0.6	2.3	–6.4	–12.2	3.2	10.1
5CB	308.5									

^a Abbreviations:

T_{NI} , nematic-isotropic transition temperature; $\Delta T_{NI} = T_{NI,5CB+azo} - T_{NI,5CB}$, shift of the T_{NI} relative to the pure 5CB;

ΔT_{coex} , nematic–isotropic coexistence range.

The results relative to the order parameter $\langle P_2 \rangle$ against the reduced temperature $T^* = T/T_{NI}$ for all the samples containing the *trans* isomers are shown in Figure 3.18 (a). All the values are found to be slightly lower than those relative to the pure 5CB, with the 8% AB₂OCH₃ doped sample showing the largest deviation.

A very interesting $\langle P_2 \rangle$ behavior is observed when the two azo-compound are transformed into their *cis* form (Figure 3.18 (b)). The results show that the role played by AB₂NO₂ in affecting the $\langle P_2 \rangle$ trend is concentration independent and, furthermore, we notice that there is no significant difference between the effects in-

duced by the *trans* and *cis* isomers on the nematic order (compare Figure 3.18 (a) with Figure 3.18 (b)). The presence of AB_2OCH_3 , instead, strongly depresses the orientational order of the LC matrix and the lowering of the $\langle P_2 \rangle$ values is enhanced when the solute concentration is increased from 3% to 8% mole fraction. In the coexistence range, the order parameter follows the peculiar trend, which has been already observed for some of the *cis* *p*-substituted azo (Section 3.3.3), due to the different solute partitioning within the N and the I phases. To summarize, we found that *cis* AB_2OCH_3 acts on the nematic order in similar way as the *cis* 4-R-azobenzenes having an alkoxy substituent.

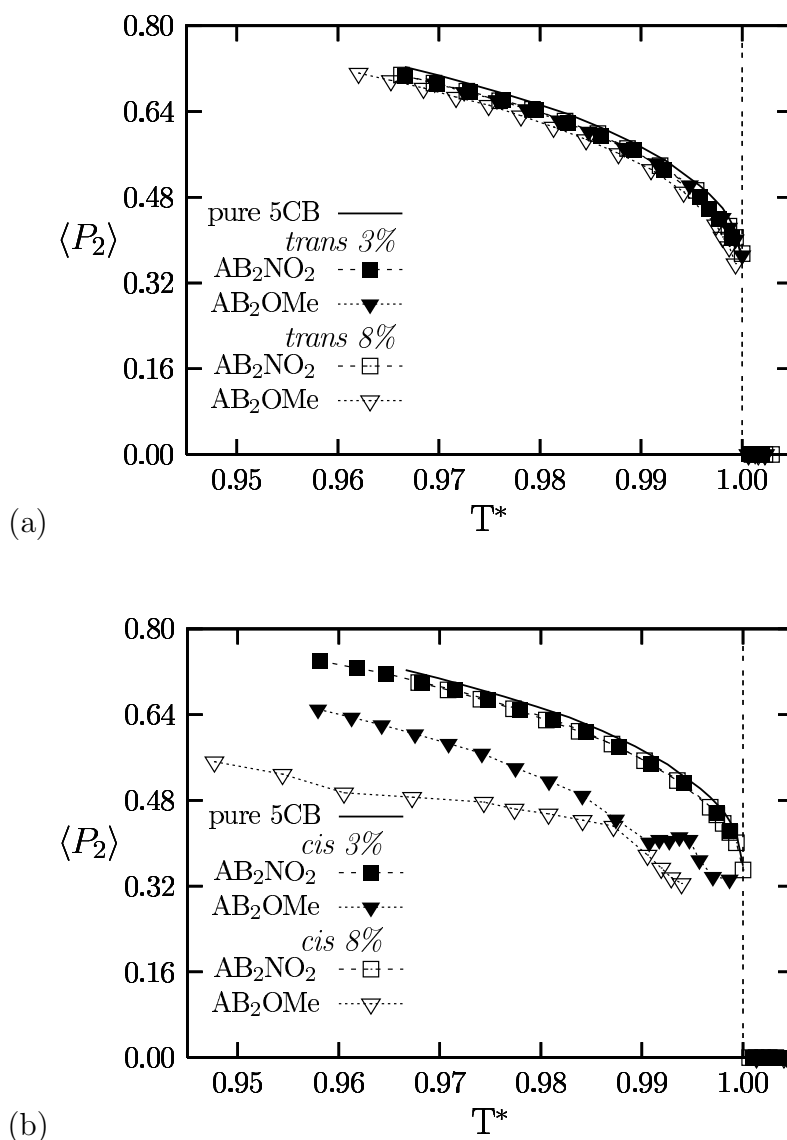


Figure 3.18: Order parameter $\langle P_2 \rangle$ of the spin probe against reduced temperature T^* for the samples doped with (a) the *trans* and (b) the *cis* azo-derivatives compared to the pure 5CB.

We found that the probe dynamics agrees with the trend observed for the 4-R-azo doped samples, being unchanged with respect to that of the pure 5CB and

showing an Arrhenius-type temperature dependence in the N and in the I phases:

- Nematic Phase

The temperature range considered for the N phases was 280.8 to 310.8 K. The best fit parameters of the $R_{\perp}^{(N)}$ Arrhenius-type temperature dependence are $R_0^{(N)} = (6 \pm 2) \times 10^7 \text{ ns}^{-1}$ and $E^{(N)} = 55 \pm 2 \text{ kJ/mol}$. $R_r^{(N)} = 7.1$.

- Isotropic Phase

For the I phases, the temperature range was 286.2 to 320.3 K with $R_r^{(I)} = 9.9$ and best fit parameters $R_0^{(I)} = (3 \pm 1) \times 10^5 \text{ ns}^{-1}$ and $E^{(I)} = 41 \pm 2 \text{ kJ/mol}$.

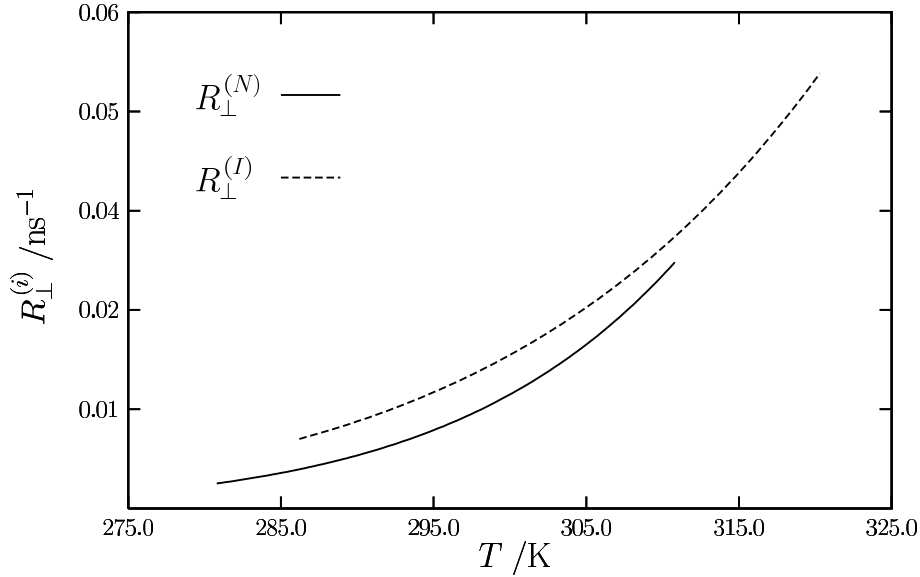


Figure 3.19: Arrhenius behavior of the tumbling diffusion coefficient $R_{\perp}^{(i)}$ (with $i = \text{N}$ or I) in the N and in the I phase (see text for details).

3.4.2 Conclusions

We have compared the behavior of a 5CB matrix doped with two azoderivatives having similar size and shape and we have found profound differences in their way of affecting the LC properties, in terms of T_{NI} and $\langle P_2 \rangle$. This result provides a clear evidence for the relevant role played on the solute-solvent interaction by the long-range contribution. We found, in fact, that simple considerations based on the solute size and shape, which are often considered as the main factors acting on the solvent ordering and stability, are not always sufficient to explain the N phase stability.

In particular *trans* AB_2NO_2 and AB_2OCH_3 were found to stabilize the N phase, but in different extent. *cis* AB_2OCH_3 and *cis* AB_2NO_2 showed, instead, opposite effects with the first strongly depressing while the second stabilizing the ordered phase. Furthermore, the LC matrix was found to be essentially insensitive to the

AB₂NO₂ configuration.

We have therefore investigated the electrostatic properties of the solutes, performing quantum mechanical calculations to obtain the dipole moment (Table 3.5), the quadrupole principal components (Table 3.6) and the EP-maps (Figure 3.20), following the method described in Section 3.3.4. Also in this case, no correlation between the N phase stability and the solute dipole and quadrupole were found. However, some qualitative considerations on the EP-maps, in agreement with the findings in Section 3.3.4, can be done.

A comparison of the EP-maps shows marked similarities between 5CB (Figure 3.20 (a)) and AB₂NO₂ (Figure 3.20 (c)). We observe, in fact, in both the cases a positively charged region on the alkyl chain, a nearly neutral region on the aromatic rings and a strongly negative site located on the cyano group of 5CB and on the nitro group of AB₂NO₂, respectively. It seems therefore reasonable that the introduction of this solute in the LC matrix does not induce any relevant changes in its properties. The geometry and the steric hindrance of *trans* AB₂OCH₃ is similar to AB₂NO₂, but some differences in the EP-map can be observed. In particular, in Figure 3.20 (b) we observe two well defined positive regions located on the alkyl chain and on the methoxy group, respectively, and a negative region centered on the azoic group. This EP-map, apart from the positive region on the methoxy group, is quite similar to that of 4-*On*Bu-azobenzene (Figure 3.14 (c)), which was found to introduce only a small degree of destabilization. *trans* AB₂OCH₃, however, acts favorably on the N phase leading to a clear stabilization, thus one can hypothesize that the positive region on the methoxy group play an important role on the solute-solvent interactions.

As mentioned in Section 3.3.4, a direct comparison between the EP-maps of 5CB and the *cis* isomers is more difficult because of the bent shape of the azoderivatives. We have therefore analyzed the main features among the *cis* isomers and found that the solute with a strong positive EP values on the atoms closest to the azoic group, AB₂NO₂ (Figure 3.20 (e)) is responsible for a lower perturbation of the N phase. Even if naive, this argument is consistent with the findings relative to the 4-R-azobenzene.

Far from a rigorous representation of the solute-solvent interactions, we have highlighted the importance of the long-range contributions in affecting the properties of the LC host. We believe that further, more quantitative advances will be obtainable only with realistic Molecular Dynamics simulations of the guest-host interactions, together with predictions of the nematic–isotropic transition temperature that are now starting to become feasible [75]. A similar approach goes well beyond the scope of this thesis and it should represent a complete new study in itself.

Table 3.5: Dipole moment (μ) and dipole components (μ_i) of the various molecular species used in this study^a

R	<i>trans</i>				<i>cis</i>			
	μ	μ_x	μ_y	μ_z	μ	μ_x	μ_y	μ_z
AB ₂ NO ₂	8.84	8.75	-1.10	-0.53	7.05	-7.01	0.66	0.18
AB ₂ OCH ₃	0.24	-0.07	-0.12	0.19	3.73	1.17	3.00	1.87
5CB	6.32	6.26	0.61	0.64				

^aValues calculated at B3LYP/6-31G** – AUG-cc-PVTZ level in the molecular inertial frame and expressed in Debye.

Table 3.6: Quadrupole components Q_{ii} of the various molecules used in this study^a

	<i>trans</i>			<i>cis</i>		
	Q_{xx}	Q_{yy}	Q_{zz}	Q_{xx}	Q_{yy}	Q_{zz}
AB ₂ NO ₂	-30.5	14.9	15.5	-11.9	-6.0	17.9
AB ₂ OCH ₃	27.3	-13.7	-13.6	20.6	-12.9	-7.7
5CB	-35.8	24.1	11.7			

^aValues calculated at B3LYP/6-31G** – AUG-cc-PVTZ level in the quadrupolar frame and expressed in Debye Å.

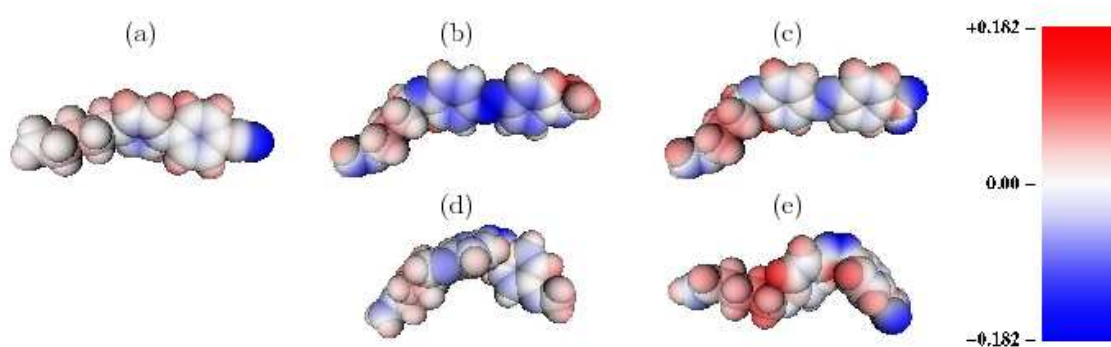


Figure 3.20: Electrostatic potential at the molecular surface for the 5CB (a), *trans* AB₂OCH₃ (b), *trans* AB₂NO₂ (c), *cis* AB₂OCH₃ (d) and *cis* AB₂NO₂ (e). Color coded according to the palette (units $4\pi\epsilon_0 e/\text{\AA}$). Geometry and charges obtained at B3LYP/6-31G** – AUG-cc-PVTZ level.

groups on the surface of these aggregates can form hydrogen bonds between different particles which lead to the formation of agglomerates (Figure 4.2). Compared to covalent bonds, the energy of hydrogen bonds is relatively low so that they can be unlocked by mechanical interaction and are subsequently available for the formation of bonds, thus fixing a new spatial arrangement of the aggregates.

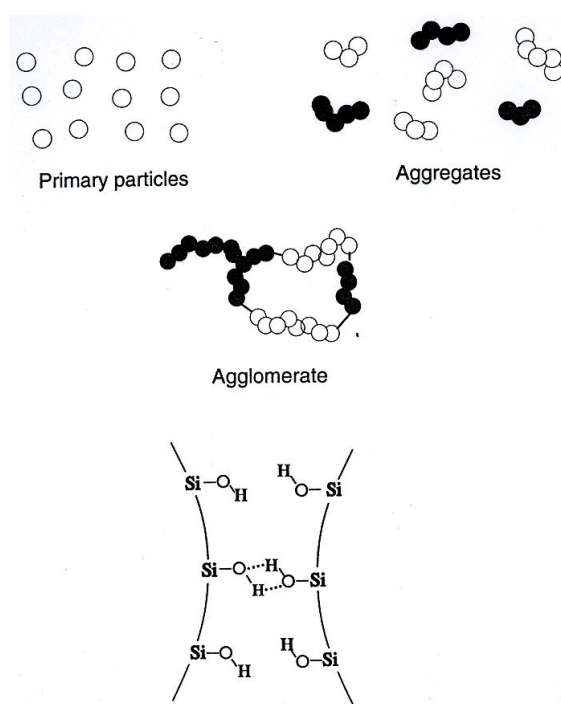


Figure 4.2: Building principle of the solid network of fumed silica depicting the formation of hydrogen bonds between the aggregates [76].

When the silica is dispersed in nematics by ordinary stirring, the resulting framework can be depicted as in Figure 4.3, where it is evident the partition in domains of different director orientations. Through the application of an electric field, this stable arrangement can be turned into another stable structure in which the nematic directors are uniformly aligned along the field direction.

From a technological point of view, these systems are particularly interesting for the development of scattering displays with memory [76], that is devices that permit to switch between a transparent and a scattering state, both of which are stable without an electric field. In these displays, the nematic “filled” with a small concentration (up to a few percent) of aerosil strongly scatters light in its field-off state because of the large optical anisotropy of the macroscopically disordered nematic. Application of an electric field aligns the nematic domains yielding a transparent state, and for appropriate combinations of aerosil type and liquid crystal, this clear state remains even after removal of the field (“memory effect”). The display can be easily switched back to its scattering state in various ways, for example, thermally by application of a focused laser beam [76, 77]. Notice that the small concentration of silica does not change the optical properties of the liquid crystal by itself; indeed no optical matching between liquid crystal and aerosil is needed.

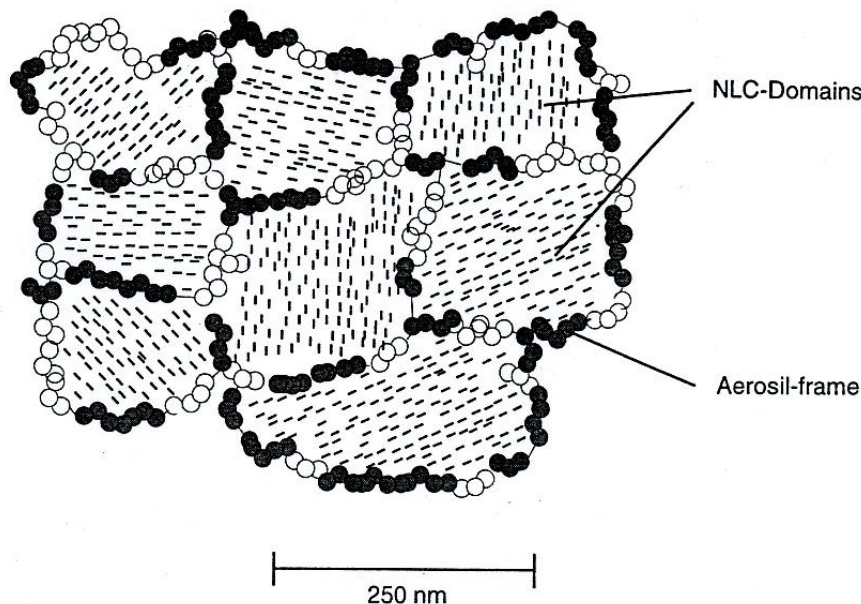


Figure 4.3: Fictional three-dimensional framework with nematic domains of randomly oriented director [76].

Eidenschink and de Jeu explained the electro-optical behavior assuming the formation of a network of aerosil particles and liquid crystal [78, 79]. There is a strong anchoring between the nematic director at the surfaces of the particles forming the network, so that not only the surfaces act elastically on the directors, but also the directors act on the surfaces and, therefore, on the particles. The reorientation of the directors in an external electric field lead to a rearrangement: in this process hydrogen bonds may be broken and new ones are formed with the agglomerate surface adjusted to the aligned director. This process is more understandable in hydrophilic aerosils with dangling silanol groups in which hydrogen bonding can lead to diffusion-limited aggregation, however the effect is obtained also with hydrophobic aerosils.

4.2 Glass-like behavior

From a more fundamental point of view, the memory effect can be considered as a manifestation of the macroscopic glass-like state of these systems. In order to investigate the origin of the memory effect and of the glassy behavior of FNs, during the last years, dynamics studies aiming at understanding the relationships between the macroscopic and the molecular level have received a growing attention.

Collective dynamics, associated with director fluctuations, appears to be strongly influenced by the aerosil concentration and by the chemistry of its surface [80]. Hydrogen bonds among the aerosil surface SiOH and between these and the LC are conceivably the main interactions holding together the network which can break, under shear stress, and then reform when the stress is removed or relieved. The

effect of H-bonds on the properties of a FN was studied by several authors by comparing dispersions of aerosils with high (hydrophilic) or low (hydrophobic) density of free OH groups on their surface. In principle, large differences in the static and dynamic observables, both at macroscopic and molecular level, are expected, due to the different surface chemistry. Glushchenko *et al.* [81] compared the residual optical transmittance, after the removal of the field, of field-aligned dispersions of hydrophobic R812 or hydrophilic A300 aerosil in various liquid crystals with different ability to create H-bonds. The maximum of the memory effect was found using the 5CB LC with a dispersion of 3 wt% of the hydrophilic A300 aerosil or between 8 and 12 wt% of the hydrophobic R812 aerosil where only a small fraction of the surface hydroxyl groups are free. This result indicated, at least for low aerosil concentrations, a clear, even though not simply proportional, relation between the magnitude of the memory effect and the number of surface OH groups available to form H-bonds with the LC. The authors concluded that the anchoring strength of the LC at the aerosil surface is a fundamental “ingredient” for the memory effect to take place (no effect was observed in a LC which can not form H-bonds).

It might be argued that the glassy behavior obtained from macroscopic and mesoscopic investigations could be observed also at molecular level or, alternatively, that it was a reflection, on a larger scale, of the slowing down of the dynamics originating directly at molecular level. Using dynamic light scattering, Aliev and Sinha [82] observed, in fact, a glass-like relaxation behavior in a dispersion of a type 200 hydrophilic aerosil in 5CB LC. Molecular and collective dynamics in dispersions of hydrophobic and hydrophilic aerosil, studied by Aliev *et al.* [80], using broadband dielectric spectroscopy (BDS) and photon correlation spectroscopy (PCS), showed that the situation is more complex. BDS provides information on molecular reorientational motion while PCS probes dynamics of collective modes associated with director fluctuations. The authors found that the treatment of the aerosil surface has a strong influence on the collective modes but it is less important for the molecular dynamics which was found to be essentially bulk-like. More recently, turbidity experiments, performed by Bellini *et al.* [83] using dispersions of A380 hydrophilic aerosil in 8CB and R812 hydrophobic aerosil in 6CB, also revealed a complex dynamic behavior with relaxation features extending from 10^{-2} up to 10^4 s and above. The authors concluded that this slow dynamics is related to nonlocal, multidomain motions, whereas the local dynamics remains unaffected. A recent study of the tumbling motion of a stearic spin probe in a dispersion of R812 hydrophobic aerosil in 8CB [61], added further details to the description of the dynamics in filled nematics. By increasing the aerosil concentration from 1 to 10 wt%, the macroscopic viscosity of the dispersions increased by several orders of magnitude, from that of a liquid to that of a gel but the microscopic dynamics was only reduced, approximately, by a factor of two, remaining, in agreement with Aliev *et al.* [80], essentially bulk-like. Interestingly, above 3 wt% aerosil concentration, this locally fluid dynamics exhibited a temperature dependence typical of a fragile glass forming system.

To investigate this very rich dynamic behavior and to examine how general it is, we have studied here a slightly different nematic in dispersions of both hydrophobic and hydrophilic aerosils across the gelation threshold (0.01 g/cm^3). We want to

study the influence of the aerosil surface chemistry on the transition to a glass-like state at molecular level and, in particular, we want to characterize the temperature dependence of the molecular dynamics to further shed light on the occurrence of this state in a nematic LC upon the introduction of random disorder, which represents still an open question [83].

4.3 Hydrophobic and Hydrophilic Aerosil in 5CB

4.3.1 Experimental Section

Hydrophilic and hydrophobic aerosils were employed to “fill” the 5CB LC. The aerosils employed were the Degussa type A380, hydrophilic, and the type R812, a modified hydrophobic aerosil where about 90% of the surface SiOH is protected by methyl groups with a density of only 0.29 free OH groups/nm². Both aerosil primary particles have a size of the order of 7 nm and do not exist in isolation but form aggregates and agglomerates with a very large specific surface area (380 m²/g for the A380 and 260 m²/g for the R812) which is almost entirely external and is not derived from any porosity.

The 5CB-aerosil samples were prepared according to the solvent method described by Iannacchione *et al.* [84] and Haga *et al.* [85] with some modifications. The aerosil was dried under vacuum at 150°C for 24 hours, weighted in dry atmosphere, and mixed with HPLC grade acetone to obtain a 0.01 g/cm³ suspension, which is not stable and forms a visible sediment in a few minutes. To avoid this problem and achieve a better suspension, the aerosil stock solution was treated for 20 min at maximum power with an ultrasonic homogenizer (Vibracell VCX 750 ultrasonic homogenizer, Sonics), which operates by immersion via a titanium transducer tip. In this way, we were able to obtain a stable aerosil dispersion, which did not form any sediment over a period of months. A CSL/5CB stock solution in HPLC-grade acetone was prepared, typically at a 5CB concentration of 0.1-0.3 g/cm³ with a spin probe concentration of 3×10^{-4} g_{CSL}/g_{5CB}. Individual samples were prepared by mixing in acetone the required volume of the CSL/5CB stock solution and of the aerosil stock solution to a final [5CB] typically of 0.02 g/cm³. Because of the very good dispersion of the aerosil stock solution, the samples were then only mechanically mixed but not further sonicated, thus avoiding potential drawbacks due to the interaction of the material of the tip with the spin probe. After stripping of the solvent in an anhydrous nitrogen stream at a temperature of 333 K, the samples were placed in a vacuum system at 10⁻² mbar and pumped on for 6 hours at 323 K. The final samples appeared uniform upon visual inspection, showing no agglomeration when checked with a microscope. However, an “aging” effect was still present in the samples, irrespective of the aerosil type employed (hydrophobic or hydrophilic), and became evident after about two weeks. It was not apparent by visual inspection of the samples but it could be readily monitored by a typical line shape of its ESR spectrum indicating that aged samples did not reform a monodomain in the same

conditions used for the fresh samples but a stronger magnetic field (up to 6300 G, which is the maximum allowed in our instrument) and a slower and longer thermalization was required. To minimize this problem and ensure the best reproducibility, all data presented here were obtained using fresh samples which were thoroughly thermalized at 6300 G, as described later in this section.

Three set of samples were studied in the nematic (N) and isotropic (I) phases: without aerosil, with R812 (at 0.3, 1, 3 and 10 wt%) and with A380 (at concentration 0.3, 1 and 3%wt). An on-scale schematic representation of the aerosil dispersion in the liquid crystal is shown in Figure 4.4.

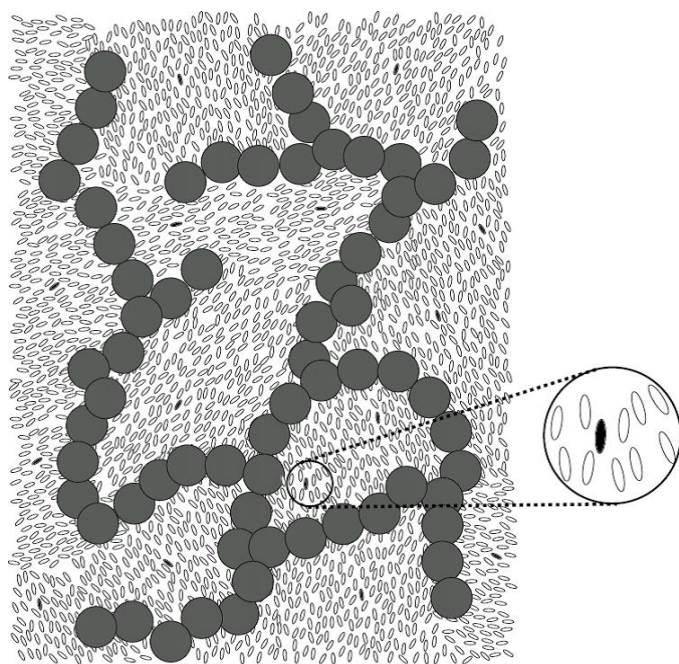


Figure 4.4: On scale schematic representation of the aerosil dispersion showing probe molecules (black particles, see inset) dissolved in the liquid crystal local ordered domains (white particles) and the silica network (gray circles).

For each sample, ESR spectra were recorded at 26 different temperatures on heating and then at the same temperatures on cooling during a continuous run at the rate of one spectra every 5-10 min, depending upon the time required to reach the equilibrium at each new temperature. The details relative to the experimental set up used to perform the ESR measurements are given in Section 2.3.1. Before a typical run, each filled nematic sample was treated with a field (FC) cooling procedure in order to anneal the initial isotropic, three-dimensional distribution of the local LC domains. The 5CB/aerosil samples were then placed in the cavity under the action of a magnetic field of 6300 G, which is the highest field available in our instrument, and were subjected to the same programmed temperature cycle taking it from 298.2 K (N phase) to 343.2 K (I phase) and then cooling it down slowly to 298.2 K at an average rate of 12 K/min which was reduced to 0.1-0.2 K/min across the phase transition. As monitored from a typical ESR line shape, this FC

procedure successfully formed a monodomain in all samples, except in the case of the 10% wt R812 sample, where the annealing treatment only had a partial effect.

4.3.2 Fitting Procedure for ESR Spectra

Because of the heterogeneous behavior of the samples after the FC procedure, the simulation of the ESR spectra required the use of two different fitting models (see Section 2.3.2 for a general description of the method). In particular, the 10% wt R812 sample, which was not annealed to a monodomain state, was analyzed assuming a polydomain model, while a monodomain was the appropriate model for the simulation of the spectra relative to the remaining samples.

For each sample, the experimental data corresponding to different temperatures within the same stage of a measurement run (heating or cooling) and within the same phase (N or I), were fitted simultaneously in a global analysis.

In a first series of fits, the principal components R_{\perp} and R_{\parallel} of the rotational diffusion tensor were considered as independent variables, but the results exhibited a certain correlation between the parameters and relatively large errors. To minimize this correlation $R_r^{(i)} = R_{\parallel}/R_{\perp}$ (with $i = \text{N or I}$) was introduced as a variable global parameter [27] and it was assumed to be temperature independent in the I phase and to have, in the N phase, a temperature dependence of Haller-type [86–88]

$$R_r^{(N)} = R_r^0 (1 - T/T_c)^{\nu} + R_r^{(I)} \quad (4.1)$$

where T_c is the temperature at which the local $\langle P_2 \rangle$ drops to zero according to the ESR spectra, $R_r^{(I)}$ was kept fixed to the value of the diffusion coefficient ratio found in the I phase whereas ν and R_r^0 , the limiting deviation of $R_r^{(N)}$ from the isotropic value at zero temperature, are adjustable parameters. Finally, the diffusion coefficient R_{\perp} was considered as an independent fit parameter for each temperature. This globalization improved significantly the analysis of the monodomain spectra reducing the correlation and the errors on the recovered parameters.

Typical experimental spectra and fits are shown in Figure 4.5 for samples at the various concentrations of the R812 aerosil in the N and I phase and the fitting strategy can be then schematically described as follows:

1. Isotropic Phase

ESR spectra in the I phases were modeled keeping $\langle P_2 \rangle$ fixed to zero and $R_r^{(I)}$ to the value obtained from the preliminary fits, while R_{\perp} and the inhomogeneous line width T_2^{*-1} were considered as temperature dependent variable parameters.

2. Nematic Phase

- Monodomain state

To model the line shapes of the samples aligned by the FC procedure, the local order parameter $\langle P_2 \rangle$, the inhomogeneous line width T_2^{*-1} and the coefficients R_r^0 and ν , describing the Haller-type behavior of $R_r^{(N)}$, were assumed as variable parameters.

- Polydomain state

In addition to the parameters employed in the simulation of monodomain spectra, the fit of a polydomain spectrum requires an extra parameter to describe the orientational distribution of the domains, that is $\langle P_2 \rangle_d$.

By comparing the ESR spectra of the 10% wt R812 sample acquired at the same temperatures on heating and on cooling, we noticed small but clear differences (see Figure 4.5 (b)). This was assumed to be due to a different distribution of the nematic directors, which depend on the magnetic field intensity and which is likely to be broader after cooling from the I phase, with respect to the initial distribution achieved with the FC procedure. The annealing procedure, in fact, was done with a magnetic field of 6300 G, whereas during the measurements the field sweep was set between 3340 and 3440 G. The degree of order within each domain, instead, can be assumed to be only dependent on the temperature and on the aerosil concentration, thus it should be the same for corresponding temperatures on heating and on cooling. Since in a preliminary analysis, the fit of the polydomain spectra presented certain correlation between the local order parameter $\langle P_2 \rangle$ and $\langle P_2 \rangle_d$, we improved the globalization scheme according to the above assumption. We have therefore assumed that the spectra obtained at corresponding temperatures, on heating and on cooling, have the same degree of order within each domain, i. e. the same $\langle P_2 \rangle$ value, but a different director distribution. In practice, one $\langle P_2 \rangle_d$ was used as global variable parameter for the spectra of the heating stage and a different one for the spectra of the cooling stage. Best fit values of $\langle P_2 \rangle_d$ are shown in Figure 4.5 (b).

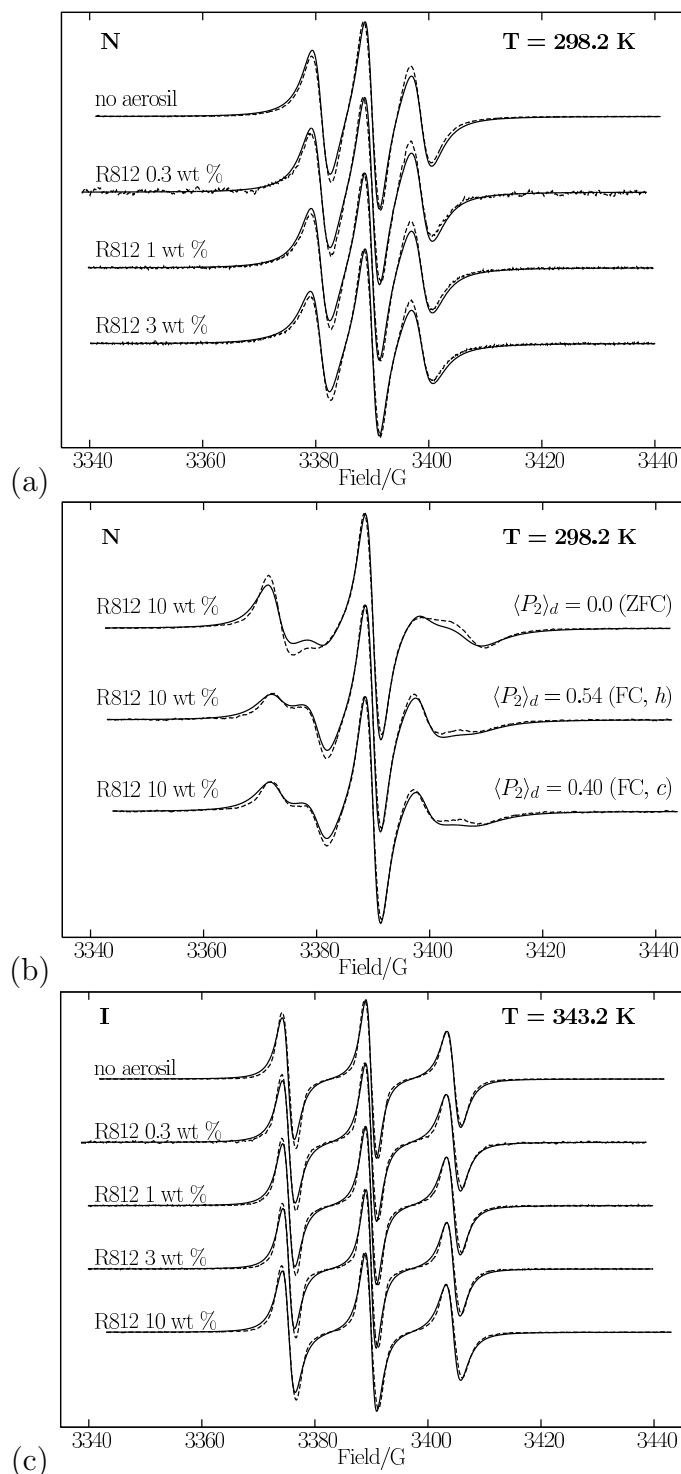


Figure 4.5: Typical experimental spectra (dashed lines) and fits (solid lines) of the samples in the nematic (a, b: $T=298.2$ K) and isotropic (c: $T=343.2$ K) phase at various R812 aerosil concentration. (a) Monodomain spectra obtained for the pure (“no aerosil”), 0.3, 1 and 3% wt samples after the field cooling (FC) procedure. (b) The 10% sample in the nematic phase was only partially aligned and remained in a polydomain state: sample before the field cooling (ZFC), field cooled sample at the beginning of the heating stage (FC, h) and FC sample after cooling from the I phase (FC, c).

4.3.3 Results and Discussion: Order and Dynamics

The N-I transition temperature observed for the pure sample is in agreement with the value declared by the manufacturer of 308.5 K and it remains essentially unchanged in the presence of the aerosil at the concentrations studied.

The $\langle P_2 \rangle$ behavior of the pure sample (“no aerosil”) in the heating and the cooling stage was essentially identical, therefore in Figure 4.6 we only report the values relative to the heating stage. Furthermore, the $\langle P_2 \rangle$ trend we have recovered is in good agreement with previous values for 5CB reported in the literature (see [89] and refs. therein). This result indicates, as expected, that the CSL spin probe is a suitable probe to monitor the order of the 5CB host.

The temperature dependence of the local orientational order parameter $\langle P_2 \rangle$ of the spin probe in the samples containing the hydrophobic and hydrophilic aerosil are presented in Figure 4.6 (a) and Figure 4.6 (b), respectively. In both the cases, we observe that, except for a few temperatures very close to the N-I transition, the $\langle P_2 \rangle$ show no hysteresis, being the values at corresponding temperatures in the heating and the cooling stages essentially identical. This result confirms the validity of our assumption of assuming, in the polydomain model, a common $\langle P_2 \rangle$ value to the spectra acquired at corresponding temperatures on the heating and cooling stages (see Section 4.3.2).

The absence of hysteresis, found instead by Marinelli and co-workers [90, 91] in thermal conductivity measurements in similar systems, can thus be ascribed to the presence of the ESR magnetic field. At least at these aerosil concentrations, in fact, it is strong enough to completely anneal the elastic strains arising in the LC, at the N-I transition, from the presence of the aerosil particles.

The decrease of the orientational order parameter with increasing aerosil concentration appears to be roughly linear in the range studied. In addition, the $\langle P_2 \rangle$ behavior is strongly affected by the aerosil type, with the hydrophilic having a larger effect. In fact, we notice that the local nematic order in the 3% wt A380 sample is lower in the whole nematic range than that observed in the case of the sample containing the highest hydrophobic aerosil concentration (10 % wt R812).

Qualitatively, the behavior of the R812 samples is similar to that observed in a previous study [61]. For the A380 samples, our results are in contrast with those obtained by Jin and Finotello [92, 93] for a type 300 hydrophilic aerosil dispersion in 8CB, where they found that the order parameter of the bulk LC was almost independent of the aerosil concentration up to ~ 10 wt%.

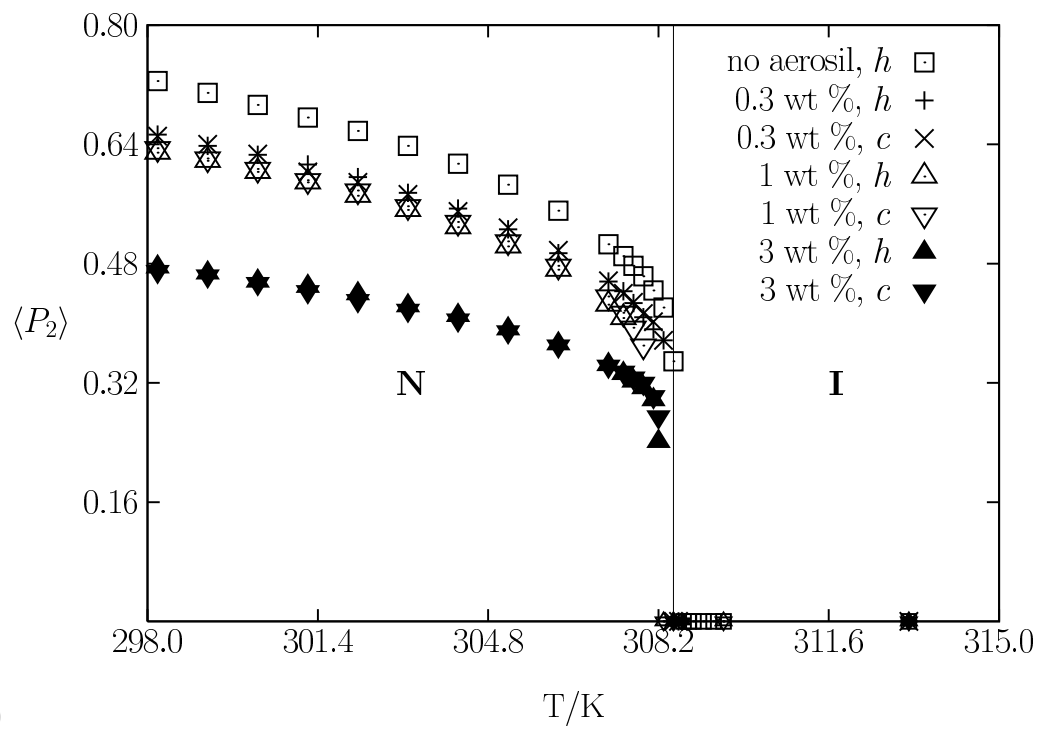
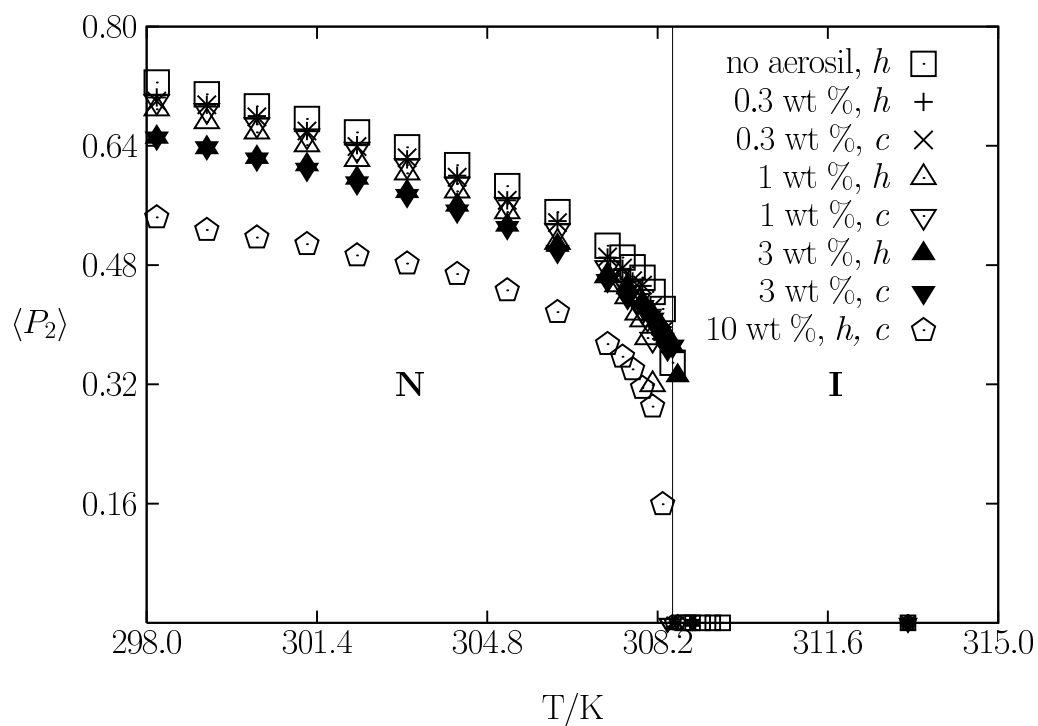


Figure 4.6: Temperature dependence of the orientational order parameter $\langle P_2 \rangle$ of the spin probe at various aerosil concentrations on heating (h) and on cooling (c); (a) hydrophobic (R812) aerosil, (b) hydrophilic (A380) aerosil.

The temperature dependence of the tumbling diffusion coefficient R_{\perp} of the spin probe at various concentrations of the R812 aerosil is shown in Figure 4.7. At all the aerosil concentrations, the values of R_{\perp} in the cooling stage (not shown) were identical to those in the heating stage and are consistent with the values of R_{\perp} obtained for CSL in similar LC systems [29, 28]. As in our previous work [61] we observe that the local rotational dynamics is only slightly affected by the presence of the aerosil.

The data in the I phase were fitted to both an Arrhenius-type equation,

$$R_{\perp} = R_0 \exp[-E/RT] \quad (4.2)$$

and to the Vogel-Fulcher-Tammann (VFT) equation,

$$R_{\perp} = R_0 \exp[-B/(T - T_0)] \quad (4.3)$$

where B is a temperature corresponding to an activation energy RB in the limiting case of an Arrhenius behavior ($T_0 = 0$ K) and T_0 is the temperature of apparent divergence of viscosity. The quantity T_0/B can be used as a material-specific parameter to quantify the kinetic fragility [94]. We found the Arrhenius model always appropriate to describe the temperature dependence of R_{\perp} in the I phase (Figure 4.7 (a), solid lines). In all the cases the VFT model, which has an extra adjustable parameter, did not improve the Arrhenius fit and was therefore rejected. Best fit values for the activation energy E are shown in Table 4.1 (upper and middle section).

A comparison between the Arrhenius and the VFT model in the N phase is presented in Figure 4.7 (b). We found that the data for the pure (“no aerosil”) sample obey the Arrhenius model (solid line) and the VFT model did not improve the fit. Interestingly, at increasing aerosil concentrations, the data consistently deviate from the Arrhenius model (solid lines) and are better described by the VFT model (dashed lines). This deviation is very small for the 0.3 and 1 wt% samples, but becomes clear at 3% wt and even more evident at 10% wt. Best fit values for the activation energy E are shown in Table 4.1 together with the VFT fit parameters B and T_0 .

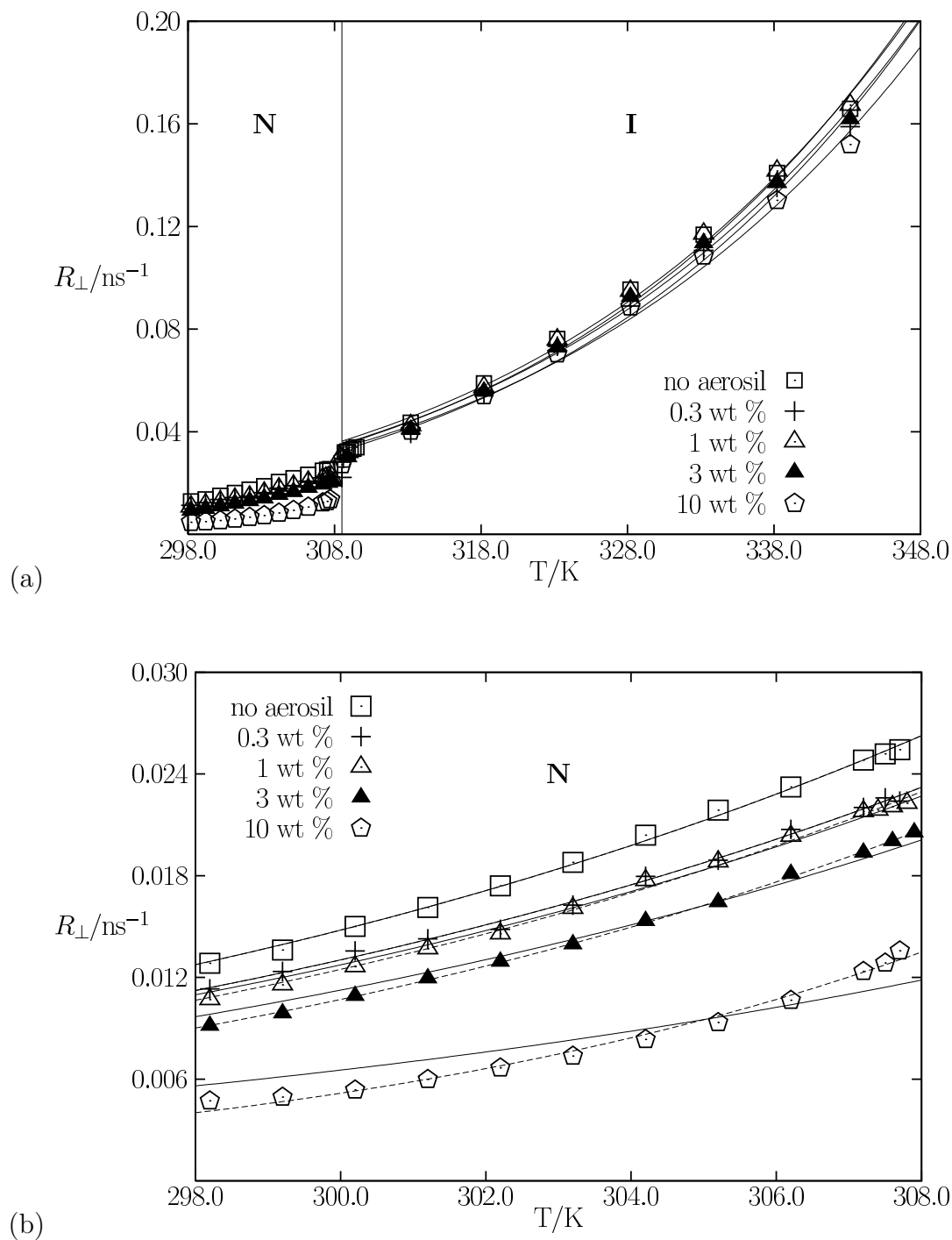


Figure 4.7: Temperature dependence of the tumbling diffusion coefficient R_{\perp} of the spin probe at various concentrations of the hydrophobic (R812) aerosil. Data in the isotropic phase (a) obey a simple Arrhenius-type equation (solid lines). (b) Detail of the nematic region shown above. Experimental data points in the vicinity of T_{NI} (above $T = 308.0$ K) have been removed. Solid lines: fit to the Arrhenius equation; dashed lines: fit to the Vogel-Fulcher-Tammann (VFT) equation (see text for details). Best fit values for the activation energy E (Arrhenius fit) or for the B and T_0 parameters (VFT fit) are shown in Table 4.1.

In Figure 4.8, we show the temperature dependence of the tumbling diffusion coefficient R_{\perp} of the spin probe at various concentrations of the A380 aerosil. Also in this case, no hysteresis was observed between the heating and the cooling stage and the local rotational dynamics, in the I phase, appears to be essentially unaffected by the presence of the aerosil and well represented by an Arrhenius-type law (solid lines). Best fit values for the activation energy E in the I phase are shown in Table 4.1 (lower section).

A comparison between the Arrhenius and the VFT model in the N phase, for the A380 samples, is presented in Figure 4.8 (b). We notice that the deviation from the Arrhenius model (solid lines) of the experimental data, which are better described by the VFT model (dashed lines), is clearly larger than that observed for the R812 samples (Figure 4.7 (b)). Best fit values for the various parameters are shown in Table 4.1 (lower section).

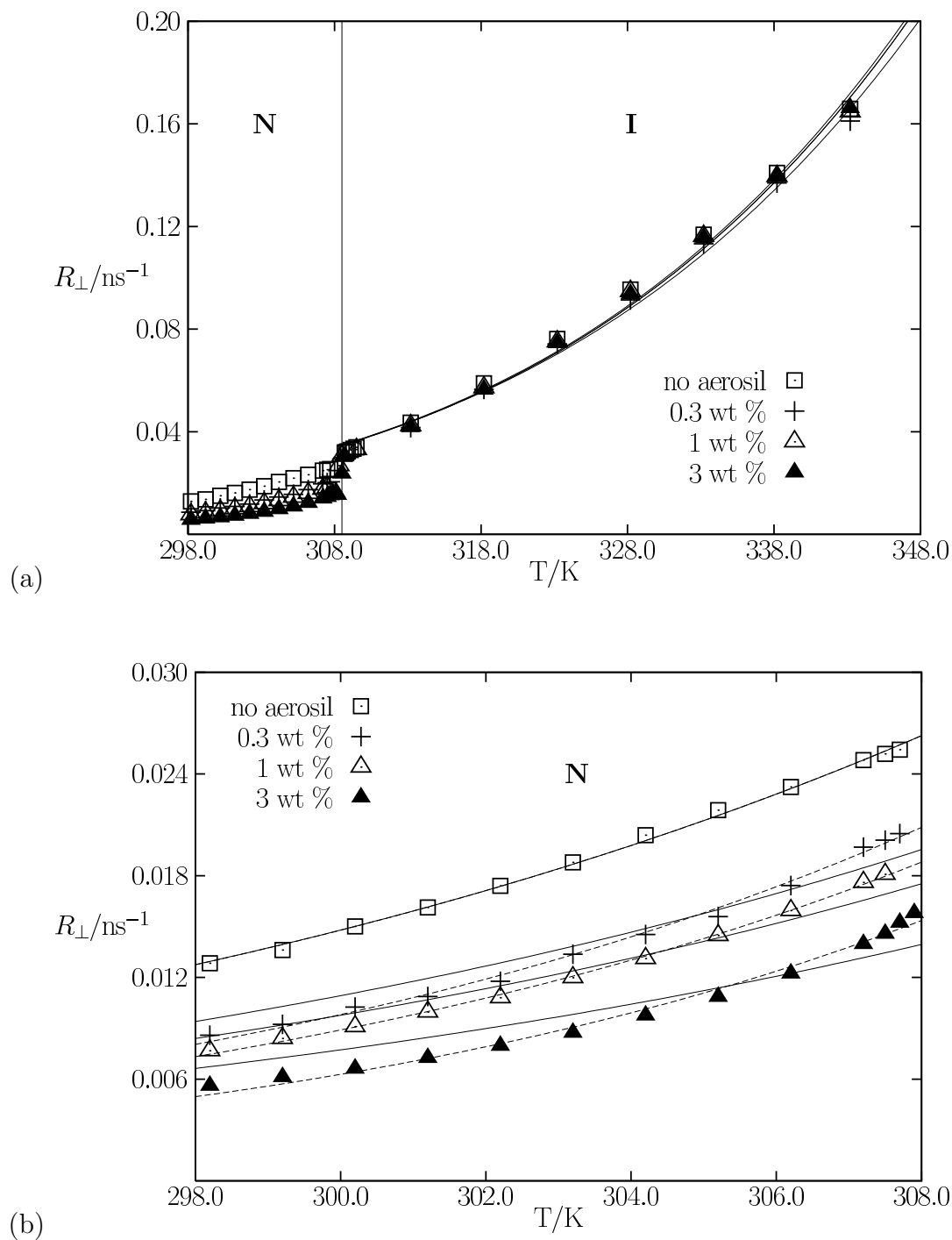


Figure 4.8: Temperature dependence of the tumbling diffusion coefficient R_{\perp} of the spin probe at various concentrations of the hydrophobic (A380) aerosil. Data in the isotropic phase (a) obey a simple Arrhenius-type equation (solid lines). (b) Detail of the nematic region shown above. Experimental data points in the vicinity of T_{NI} (above $T = 308.0$ K) have been removed. Solid lines: fit to the Arrhenius equation; dashed lines: fit to the Vogel-Fulcher-Tammann (VFT) equation (see text for details). Best fit values for the activation energy E (Arrhenius fit) or for the B and T_0 parameters (VFT fit) are shown in Table 4.1.

The values of E for the I phase, reported in Table 4.1, are essentially concentration- and aerosil-type-independent and are smaller than the value observed in the N phase for the pure (“no aerosil”) sample.

In the N phase, the deviation from an Arrhenius-type behavior is well described by the VFT parameters B and T_0 . In particular, for both the R812 and the A380 samples, we observe an increase of the VFT temperature T_0 , indicating the onset of a glass-like behavior at molecular level. In our previous work [61], this onset was observed at a concentration of R812 aerosil of 3 wt%, whereas here it is visible already at 1 wt% of hydrophobic and at 0.3 wt% of hydrophilic aerosil.

Table 4.1: Best fit values of the activation energy E (Arrhenius model) and of the parameters B and T_0 (VogelFulcherTammann model) obtained from the analysis of the temperature dependence of the tumbling diffusion coefficient R_{\perp} (see text for details).

Phase		E (kJ/mol)	B (10^3 K)	T_0 (K)
N	no aerosil	55.1 ± 1.6		
I	no aerosil	40.5 ± 2.1		
	R812 conc. (% wt)	E (kJ/mol)	B (10^3 K)	T_0 (K)
N	0.3	55.4 ± 2.2		
N	1		6.3 ± 0.2	16 ± 4
N	3		5.9 ± 0.1	37 ± 4
N	10		4.3 ± 0.3	115 ± 14
I	0.3	41 ± 4		
I	1	39 ± 3		
I	3	39 ± 3		
I	10	39 ± 3		
	A380 conc. (% wt)	E (kJ/mol)	B (10^3 K)	T_0 (K)
N	0.3		5.3 ± 0.1	66 ± 6
N	1		5.2 ± 0.2	69 ± 10
N	3		4.5 ± 0.3	102 ± 14
I	0.3	39 ± 3		
I	1	40 ± 3		
I	3	40 ± 4		

All the analyses were done separately for the nematic (N) or isotropic (I) phase. Upper section, “no aerosil” sample; middle section, R812 samples; lower section, A380 samples.

The value of the diffusion coefficient ratio R_r for all the samples in the I phase was found to be 7.1 ± 2.4 which is in reasonable agreement with the value of 4.7 expected in the Stokes-Einstein limit [28]. The temperature dependence of R_r in the N phase is shown in Figure 4.9. The ratio is always larger than in the I phase, it increases with the aerosil concentration and the deviations are larger for the hydrophilic aerosil.

The temperature dependence of R_{\parallel} , obtained as the product of R_r and R_{\perp} , is presented in Figure 4.10. Despite the quite large uncertainties, it appears evident

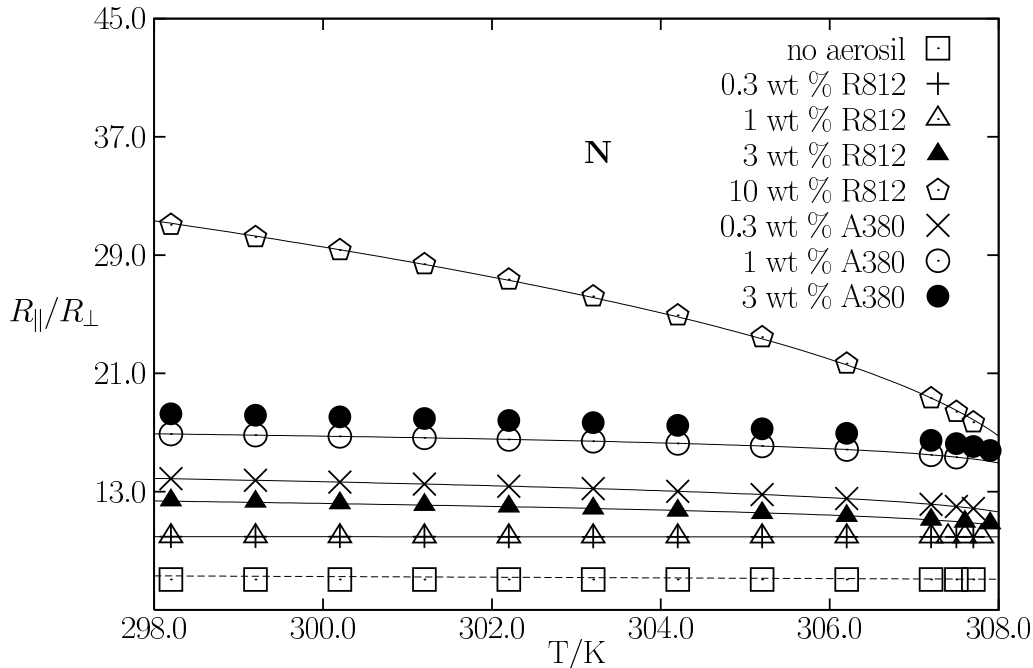


Figure 4.9: Temperature dependence of the spin probe diffusion coefficient ratio $R_r = R_{\parallel}/R_{\perp}$, for all the nematic samples studied, obtained via the globalization scheme described in the text.

that all the behaviors are very similar, indicating that the presence of the aerosil has mainly the effect of decreasing the tumbling motion of the spin probe (and hence of the LC host), whereas the rotation around the main molecular axis remains almost unaffected. Such behavior could be explained by the interaction, via H-bonds formation, between the liquid crystal cyano group and the hydroxy groups on the aerosil surface.

Our results are not in agreement with Ewiss *et al.* [95] who studied the dynamics of 5CB with aerosil using dielectric spectroscopy and obtaining significantly different values of the activation energy E . This could be due only in part to the different aerosil employed. In particular, in the N phase, they observed a decrease of E , from 75 kJ/mol for the pure 5CB to 50 kJ/mol for the 5 wt% aerosil sample. This is a large change in the molecular rotational dynamics and it goes in the opposite direction compared to our findings and also to what could be reasonably expected. In fact, it seems quite strange that the aerosil will “ease” the dynamics (and with such a large effect) instead of impairing it. Unfortunately, an explanation for this behavior was not provided.

We notice that the preparation of their aerosil dispersions has been done without using a solvent, which has been reported (and verified by us) to affect the reproducibility of the sample preparations due to aggregation and non optimal mixing of the components (see, e. g. [61] and refs. therein). The aerosil aggregation level, and not only its concentration, is likely to be very important in determining the properties of FN samples and specific studies on the effects of aggregation are still lacking in the literature. Aggregation is difficult to control since it is only partially deter-

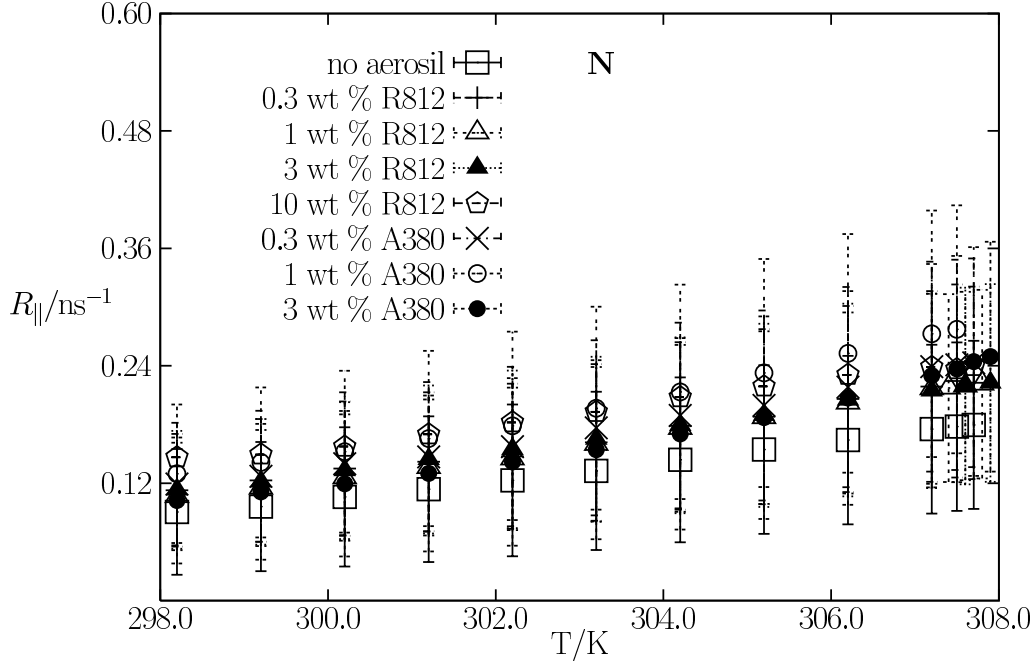


Figure 4.10: Temperature dependence of the spin probe diffusion coefficient R_{\parallel} of the spin probe for all the nematic samples studied.

mined by the aerosil concentration and depends also from the sample preparation method: mechanical mixing, sonication, thermal treatments, “aging”, etc.

4.3.4 Conclusions

By using the ESR spin probe technique, we have studied the order and the dynamics of the 5CB liquid crystal in dispersions of both hydrophobic and hydrophilic aerosils across the gelation threshold (0.01 g/cm^3). We have found that, by increasing the aerosil concentration up to 10 wt%, the order parameter $\langle P_2 \rangle$ of the spin probe in the FN systems is depressed and that the effect is larger for the hydrophilic aerosil. When the system is no longer to form a monodomain, the dependence of the degree of alignment of the local nematic domains on the annealing conditions (field intensity, aerosil type, etc.) can be observed providing information on the reorganization of the aerosil network which is considered to be crucial in the memory effect.

The molecular reorientation rate is, instead, only slightly dependent on the aerosil type. The differences are less evident than what could be expected considering the large variation in the chemical properties of the surface of the two aerosils.

The small influence of the aerosil concentration on the molecular dynamics is also quite surprising considering that the macroscopic viscosity of the system changes considerably, with increasing the aerosil concentration, from that of a fluid (pure LC) to that of a gel (3% wt A380 and 10% wt R812). A simple explanation for these results, in agreement with other authors [96], is that, at the concentrations

used in this work, only a small fraction of the LC molecules is in direct contact with the aerosil surface so that its effects are quickly lost as we move away from it. Therefore, on the average, the spin probe will sample the bulk of large “pools” of LC where the surface effects are relatively weak. In particular, we observed that only the molecular tumbling motion is affected by increasing aerosil concentration whereas the rotation around the main molecular axis is essentially concentration and aerosil-type independent.

Despite this, we were able to detect a fundamental difference between the pure LC and the aerosil dispersions in the nematic phase. This is represented by a deviation from the Arrhenius behavior of the temperature dependence of the rotational diffusion coefficient R_{\perp} . The deviation is well represented by a Vogel-Fulcher-Tammann type law and, as expected, is larger for the hydrophilic aerosil. In fact, this non-Arrhenius behavior can be appreciated at 1 wt% of hydrophobic and already at 0.3 wt% of hydrophilic aerosil, suggesting that a glass-like state can be induced in a nematic by a very small amount of random disorder.

Chapter 5

Holographic Polymer-Dispersed LCs

5.1 Introduction to HPDLC

Interest in liquid crystalline materials confined to curve geometries has expanded greatly in recent years because of their important role in new and emerging electro-optic technologies and their richness in physical phenomena [97]. One of the most fascinating developments of LCs in complex geometries has been originated by the marriage of two polymer-related technologies: photopolymer holography and polymer dispersed liquid crystals (PDLC). The result is a new type of material known as the holographic PDLC (H-PDLC).

HPDLC consist of periodic LC rich layers separated by pure polymer layers [98]. The holographic exposure of a syrup containing monomer and LC is used to photopolymerize the monomer while selectively placing the LC in well-defined periodic planes. The LC domains inside the planes are confined in droplets with typical size in the range of 200-500 nm and with random director distribution. The resulting structure is similar to that depicted in Figure 5.1 (a). In this field-off state, owing to the periodically modulated refractive index, generated by the layered structure, the HPDLC behaves as a transmissive or reflective spatial diffraction grating. The great advantage of using LCs as “filling material” relies on the modulation of the diffraction efficiency which can be performed by applying an electric field across the film. As the LC directors reorient along the electric field direction, the ordinary refractive index of the LC matches that of the surrounding polymer leading to a transparent state, thus cancelling the the refractive index profile (Figure 5.1 (b)).

Switchable hologram are under active consideration for a number of applications, such as optical communication, panel display, information storage and integrated optics and since the properties of the HPDLC materials strongly depends on the photopolymer-LC formulation [99–101], the main interest in these systems is currently focused on the study of the structure-properties relations. In this regard, the polymer morphology has been detailed investigated using optical microscopy [102–104] and electron microscopy techniques [105–107], therefore information on droplet size, droplet shape, Bragg periods and interfacial roughness are available. Very little

is known, however, about the properties of the LC inside the nano-droplets. Due to the confinement, the T_{NI} of the LC in the HPDLC systems is found to be lower than that observed in the bulk. The first study dealing with the orientational order of the LC enclosed into the droplets was performed on a HPDLC system containing 5CB as active matrix and showed that a radial director structure is most likely present at the polymer interface with trapped defects that should resemble a line-segment [108]. A recent NMR investigation on a HPDLC containing the commercial mixture BL038 and deuterated 5CB showed a quite complex behavior, revealing a wide spread in the T_{NI} , that is the occurrence of a gradual transformation from the nematic to the isotropic phase, instead of a sharp transition [109]. The authors concluded that this behavior was due to both to the polydispersity of the nano-droplets and to the difference in the composition inside the various droplets. This broadened transition avoided the recovering of meaningful values of the order parameter, however, a strong orienting effect played by the polymer surface was apparent even in the I phase.

It is clear that further efforts are needed to better understand the actual state of the liquid crystalline order in a standard HPDLC material. Therefore, working in collaboration with the Electrical and Computer Engineering Department of the Drexel University, we have recently start to investigate an HPDLC system analogous to that studied by Vilfan *et al.* [109] employing the ESR spectroscopy. In the following we describe the system that we are currently studying and the first results obtained from the preliminar analysis performed.

5.2 Experimental Section

5.2.1 HPDLC film preparation

The HPDLC samples were prepared by our colleagues at the Drexel University. Here it is briefly reported the method employed to produce the HPDLC films.

A homogeneous mixture containing prepolymer, BL038 LC, a photosensitive-dye and, of course, the ESR spin probe CSL was placed between glass slides and illuminated by two coherent laser beams forming an interference fringe pattern within the sample, as shown in Figure 5.2 (a). In bright fringes the polymerization takes place more rapidly than in the dark regions. Consequently, the polymer molecules concentrate in the bright regions whereas the LC molecules, together with the spin probe, presumably diffuse into dark regions, where they separate from the polymer in the form of nano-droplets. The structure of the resulting HPDLC is schematically shown in Figure 5.2 (b).

The mixture composition is given in Table 5.1. The HPDLC syrup was placed between two glass slides with 50 μm spacing and the grating was written with a laser line at 546 nm.

5.2.2 ESR measurements of the HPDLC film

In order to compare the behavior of the mesogenic molecules inside the nano-

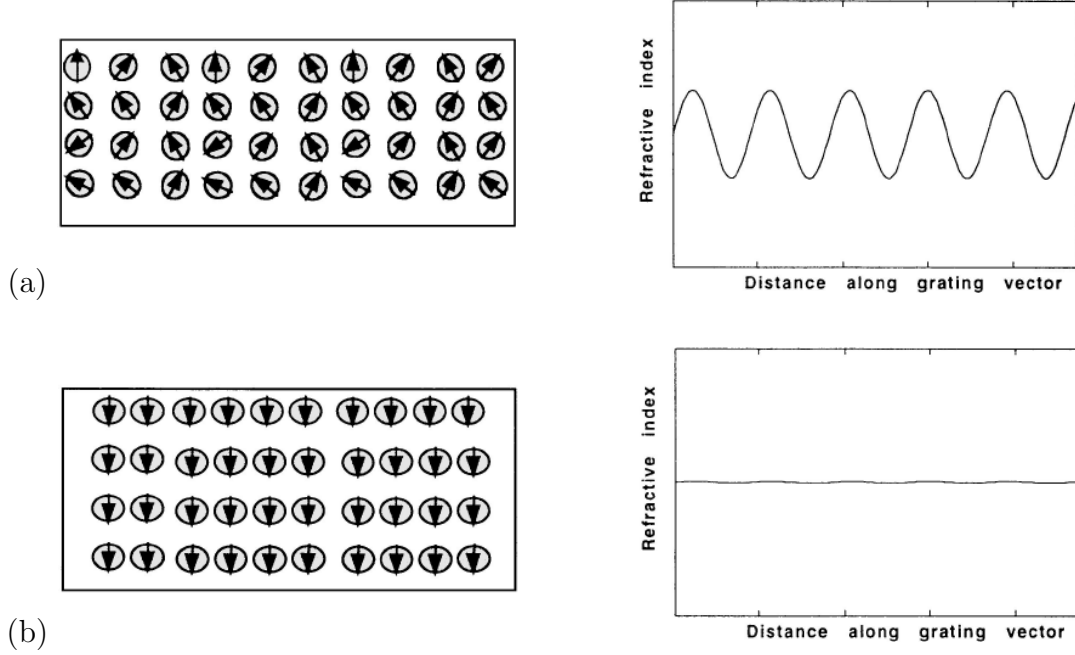


Figure 5.1: Schematic of grating structure consisting of polymer planes and LC nano-droplets. (a) In the field-off state the directors (arrows) are randomly oriented and this results into a periodic refractive index profile in the vertical direction. (b) When an electric field is applied along the grating vector, all the directors align causing a disappearance of the refractive index profile [98].

droplets to that relative to the bulk state, we have performed a series of measurements on the BL038 LC. This is a commercially available mixture which contains 5CB and 5OCB (see Table 5.1), therefore it seems reasonable that the CSL spin probe is suitable to mimic the mesogen behavior. The nominal phase sequence of BL038 is:

- Crystal-Nematic: > 273 K
- Nematic-Isotropic: 373 K

We have therefore performed the ESR measurements inserting the BL038/CSL mixture ($g_{CSL}/g_{BL038} = 6 \times 10^{-4}$) into a glass capillar and exploring, on a heating stage, a wide temperature range, from 290 K to 400 K.

To perform the ESR measurements on the HPDLC film, we carefully inserted the whole cell into the instrument so that only the portion of the sample irradiated by the laser was placed in the resonant cavity. Due to the low amount of probe in the sample, in order to achieve a good signal/noise ratio, for each spectrum 50 accumulations were required. The temperature range considered was consistent with that investigated for the BL038 in the bulk.

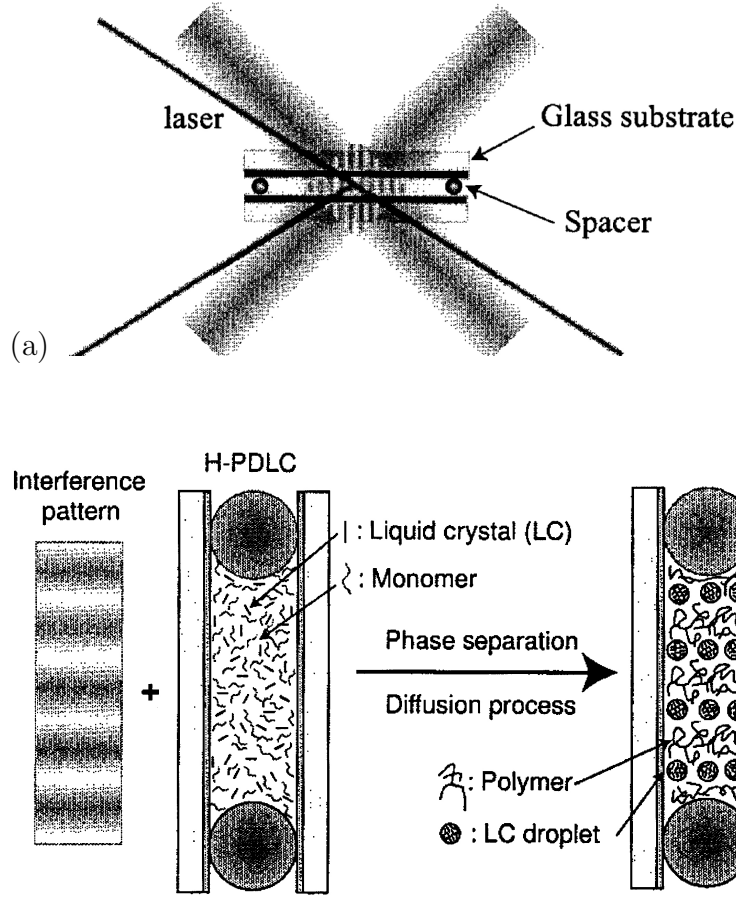


Figure 5.2: (a) Experimental set up used for recording the transmission holographic grating. (b) Illustration of the diffusion process occurring when the HPDLC cell is illuminated with an interference pattern.

5.3 Fitting Procedure for ESR Spectra

The fitting model used to simulate the ESR spectra of the pure BL038 LC in the bulk is based on the reasonable assumption that the nematic domain directors are perfectly aligned by the magnetic field, that is a monodomain model (see Section 2.3.2). The relevant parameters involved in the simulation of the ESR spectra are:

- $\langle P_2 \rangle$, the order parameter of the spin probe, which is temperature dependent, was optimized in the N phase and kept fixed to zero in the I phase
- $R_r^{(i)} = R_{\parallel}^{(i)} / R_{\perp}^{(i)}$ (with $i = N$ or I), the ratio of spinning and tumbling diffusion coefficients of the spin probe, which was assumed to be temperature independent both in the N and in the I phase. Best fit values are: $R_r^{(N)} = 6.2$ and $R_r^{(I)} = 6.9$.
- R_{\perp} , the tumbling diffusion coefficient of the spin probe, which is temperature

Table 5.1: Chemical composition of the homogeneous mixture used to prepare the HPDLC films.

Component	Product name	% wt
LC	BL038	36
ESR Spin probe	CSL	<0.01
Monomeric urethan resin	UCB Radcure 4866	25
	UCB Radcure 4833	25
Photoinitiator	Rose Bengal	0.56
Coinitiator	n-phenylglycine	1.4
Chain Terminator	n-vinyl-pyrrolidinone	12.04

BL038 is an LC commercial mixture with main components are 4-cyano-4'-*n*-pentylbiphenyl (5CB) (from 25% wt to 50% wt) and 4-cyano-4'-*n*-pentylxybiphenyl (5OCB) (from 10% to 25%), as reported by the manufacturer.

dependent, which was optimized both in the N and in the I phase

By visual inspection of the line shapes, we noticed that the magnetic field of the instrument does not align the nematic directors of the nano-droplets. Therefore, a polydomain model (see Section 2.3.2) was instead used to fit the spectra of the HPDLC sample. We have assumed a 3D isotropic distribution of the nematic director and used the following fitting scheme:

- $\langle P_2 \rangle_d = 0$, expressing the isotropic director distribution
- $\langle P_2 \rangle$ was optimized in the N phase and kept fixed to zero in the I phase
- $R_r^{(i)} = R_{\parallel}^{(i)} / R_{\perp}^{(i)}$ (with $i = N$ or I) was assumed to be temperature independent both in the N and in the I phase. Best fit values: $R_r^{(N)} = 13.4$ and $R_r^{(I)} = 14.8$.
- R_{\perp} , temperature dependent, optimized

In Figure 5.3 some of the ESR spectra relative to the HPDLC sample are reported together with the simulated spectra obtained by the fitting procedure described above. We found a good agreement between the experimental and the simulated spectra.

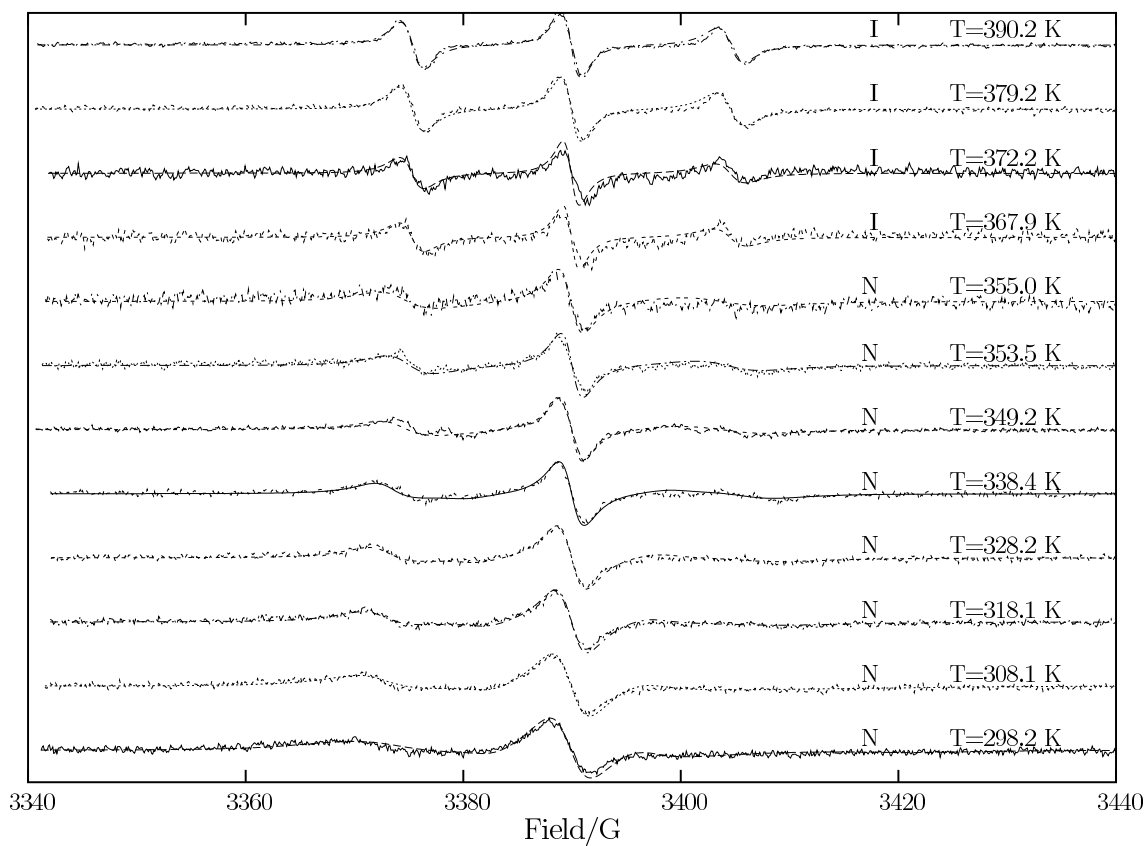


Figure 5.3: Experimental ESR spectra (dashed line) and fits (solid line) of the HPDLC sample. For each spectrum, the temperature and the corresponding phase are indicated.

5.4 Results: T_{NI} , order and dynamics

In this section the preliminary results relative to the first HPDLC sample studied are reported and these are compared with the behavior found in the bulk.

The nematic-isotropic transition in the bulk occurs at $T_{NI} = 374.0$ K and in a range of about 3 K we observed the coexistence of the N and the I phase. A lowering in the T_{NI} with respect to the bulk is recovered in the HPDLC sample, where the transition occurs at 355.0 K. A decrease in the T_{NI} was also observed by Vilfan *et al.* [109], with a downshift of about 40 K. The stronger variation found in that case is probably due to the different chemical composition of the LC mixture.

The temperature dependence of the local order parameter in the HPDLC droplets is compared with the trend relative to the bulk state. The $\langle P_2 \rangle$ values of the nematic phase in the coexistence region of BL038 in the bulk are not shown. We found that the orientational order of the LC confined into the nano-droplets is higher than that in the bulk until $T^* = 0.91$. At higher temperatures the $\langle P_2 \rangle$ values of the LC inside the droplets, instead, is found to be lower to those in the bulk BL038. A reason for such behavior may be an inhomogeneous distribution of the droplet size and of the droplet composition, however, further investigations are necessary to shed light on this point. We will, therefore, perform SEM and Raman investigations to study the polymer morphology and additional HPDLC samples containing as LC a pure compound, instead of a mixture will be considered.

Our findings on the order parameter are in contrast with the results obtained by Vilfan *et al.* [109]. They found, in the whole temperature range explored, that the orientational order in the nano-droplets is lower than that in the bulk and this result was explained in terms of disorienting effect played by the polymer surface.

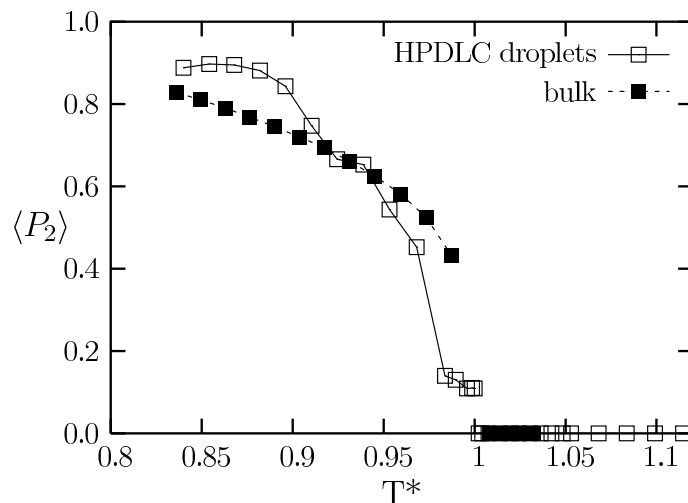


Figure 5.4: Local order parameter $\langle P_2 \rangle$ against reduced temperature T^* of BL038 LC inside the nano-droplets of the HPDLC sample (open squares) and in the bulk (filled squares).

In Figure 5.5 is reported the dynamic behavior recovered in the bulk and in the confined system. As expected, the spin probe in the nano-droplets reports a slowing

in the tumbling motion both in the N and in the I phase. This could be due both to confinement effects and to interactions between the LC molecules in the surface layer and the polymer.

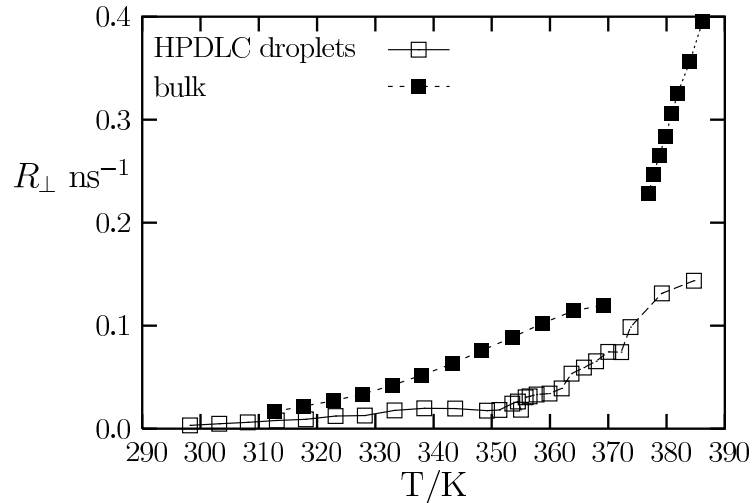


Figure 5.5: Temperature dependence of the spin probe diffusion coefficient R_{\perp} in the HPDLC sample (open squares) and in the bulk.

5.5 Conclusion

To our knowledge, the ESR spectroscopy, combined with the spin probe technique, has never been applied to the HPDLCs and our preliminary results show that this method is well-suited for a molecular level investigation of the properties of the nano-confined LC.

Of course, further experiments are necessary to deepen our knowledge of the LC-polymer interaction and to eventually confirm the observed behavior.

Appendix A

Euler Angles

The orientation of a rigid body in three-dimensional space can be described by the Euler angles. To give an object a specific orientation it may be subjected to a sequence of rotations. According to Euler's rotation theorem, any rotation may be described using three angles. If the rotations are written in terms of rotation matrices B, C, and D, then a general rotation A can be written as

$$A = BCD \quad (\text{A.1})$$

The three angles giving the three rotation matrices are called Euler angles and they are a means of representing rotations and, therefore, the spatial orientation of any frame of the space as rotation from a reference frame.

There are several conventions for Euler angles, depending on the axes about which the rotations are carried out. Here the convention proposed by Rose [4] is presented.

In Figure A.1 the laboratory frame is identified by the XYZ frame, while the molecular reference frame is xyz and the two coordinate systems have a common origin. It is possible to bring the two system to coincide, by operating the following three sequential rotations:

1. rotate around Z by the angle α
2. rotate around the new Y axis by the angle β
3. rotate around the new Z axis by the angle γ

Thus to rotate a generic matrix \mathbf{T} defined in the reference frame xyz to the XYZ axis the following rotations should be applied:

$$\mathbf{T}' = \begin{bmatrix} t_{XX} & t_{XY} & t_{XZ} \\ t_{YX} & t_{YY} & t_{YZ} \\ t_{ZX} & t_{ZY} & t_{ZZ} \end{bmatrix} = \begin{bmatrix} r_{Xx} & r_{Xy} & r_{Xz} \\ r_{Yx} & r_{Yy} & r_{Yz} \\ r_{Zx} & r_{Zy} & r_{Zz} \end{bmatrix} \begin{bmatrix} t_{xx} & t_{xy} & t_{xz} \\ t_{yx} & t_{yy} & t_{yz} \\ t_{zx} & t_{zy} & t_{zz} \end{bmatrix} \begin{bmatrix} r_{Xx} & r_{Xy} & r_{Xz} \\ r_{Yx} & r_{Yy} & r_{Yz} \\ r_{Zx} & r_{Zy} & r_{Zz} \end{bmatrix} \quad (\text{A.2})$$

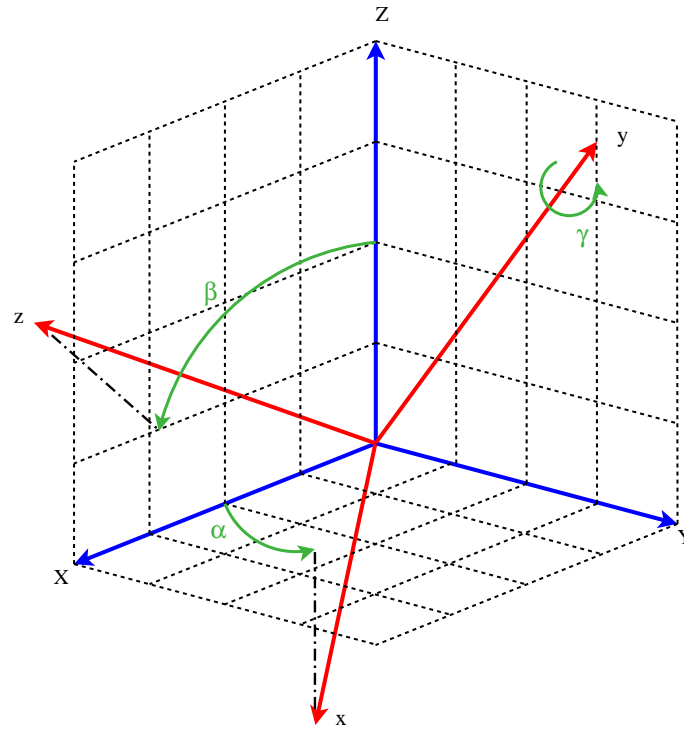


Figure A.1: Euler angles representation.

where

$$\begin{aligned}
 r_{Xx} &= \cos\alpha \cos\beta \cos\gamma - \sin\alpha \sin\gamma \\
 r_{Yx} &= \sin\alpha \cos\beta \cos\gamma + \cos\alpha \sin\gamma \\
 r_{Zx} &= -\sin\beta \cos\gamma \\
 r_{Xy} &= -\cos\alpha \cos\beta \sin\gamma - \sin\alpha \cos\gamma \\
 r_{Yy} &= -\sin\alpha \cos\beta \sin\gamma + \cos\alpha \cos\gamma \\
 r_{Zy} &= \sin\beta \cos\gamma \\
 r_{Xz} &= \cos\alpha \sin\beta \\
 r_{Yz} &= \sin\alpha \sin\beta \\
 r_{Zz} &= \cos\beta
 \end{aligned}$$

Appendix B

Synthesis of 4-*Ot*-Bu-phenylazobenzene

Following the standard Mills reaction [57], a solution of nitrosobenzene (0.02 mol) and 4-(*tert*-butoxy)aniline (0.015 mol) in acetic acid was refluxed for 1 hour at 90°C. 4-(*tert*-butoxy)aniline was synthesized as described [110] and nitrosobenzene was obtained from Aldrich. The excess of acetic acid was removed in vacuo, the residue was neutralized with an aqueous sodium carbonate solution (10%) and then extracted three times with diethyl ether. The solvent excess was removed in vacuo and the resulting red solid was purified on a silica column by elution with petroleum ether and an increasing diethyl ether content. This procedure gave rise to the desired 1-[4-(*tert*-butoxy)phenyl]-2-phenyldiazene (4-*Ot*-Bu-phenylazobenzene) with a yield of 80%. Melting points were determined on a Kofler hot-stage apparatus. ¹H and ¹³C-NMR spectra were recorded on a Varian Gemini 300. Mass spectra were recorded using a ESI Waters ZQ-4000 instrument. 1-[4-(*tert*-butoxy)phenyl]-2-phenyldiazene: m.p. 46 – 47°C; δ_C (75.4 MHz; CDCl₃) 29.3 (q), 79.9 (s), 123.0 (d), 124.1 (d), 124.2 (d), 129.4 (d), 130.9 (d), 148.8 (s), 153.1 (s), 158.9 (s); δ_H (300 MHz; CDCl₃) 7.89 (2H, m, Ar.), 7.87 (2H, d, J 9.0 Hz A₂B₂), 7.49 (4H, m, Ar.), 7.12 (2H, d, J 9.0 Hz A₂B₂), 1.42 (9H, s); m/z 293 (M + K), 277 (M + Na), 255 (M + H), 221, 199.

List of Figures

1.1	Molecular organization of a nematic liquid crystal. The mesogens molecules are on average parallel one to each other and they tend to align with respect to a preferred direction (\mathbf{n}), called the director.	4
1.2	Molecular organization of (a) smectic A phase with every layer lying perpendicular to the director (\mathbf{n}) and (b) smectic C phase with the director (\mathbf{n}) tilted with respect to the layer normal (\mathbf{a}).	4
1.3	(a) Molecular organization of a cholesteric phase and (b) the chiral twisting of the director.	5
1.4	Phase transitions of (a) thermotropic and (b) lyotropic liquid crystals.	6
1.5	Example of technological application in the field of liquid crystals: scheme of a twisted nematic cell.	7
1.6	Example of technological application in the field of liquid crystals: picture of a cholesteric thermoeter.	7
2.1	Zeeman splitting of an $S = 1/2$ state.	13
2.2	Plot of a Lorentzian curve and of its first derivative.	18
2.3	Chemical structure of a generic nitroxide free radical.	18
2.4	Energy level scheme for a nitroxide radical. The Zeeman splitting and the corresponding hyperfine levels are displayed together with the three allowed ESR transitions (dashed blue arrows).	19
2.5	Dependence of the energy levels on the field strength for a nitroxide. The allowed transitions, indicated with blue arrows, give rise to a three line ESR spectrum.	19
2.6	Angular dependence of the ESR spectrum features.	20
2.7	Molecular structure of 5CB LC.	30
2.8	The CSL spin probe together with the chosen ordering and magnetic molecular frames (see text for details).	31
3.1	Azobenzene photoisomerization. The <i>trans</i> form (left) and the <i>cis</i> form (right) can be interconverted using light with an appropriate wavelength.	35
3.2	Typical absorption spectra of azocompounds showing the high-intensity π - π^* band in the UV region and the low-intensity $n - \pi^*$ band in the visible region.	36

3.3	Directed bending of a polymer film by light [43]. a, Chemical structures of the liquid-crystal , monomer (molecule 1) and crosslinker (molecule 2) used for preparation of the film; b, Precise control of the bending direction of a film by linearly polarized light.	36
3.4	Two types of photomodulation of orientation of LC molecules [44]. A), Change in LC directors orientation (order-order change); B), Change in phases (phase transition, order-disorder change).	37
3.5	Order-disorder change: phase diagram of the photochemical phase transition of azobenzene/LC systems. N, nematic; I, isotropic.	38
3.6	Order-disorder change: mechanism of photochemical phase transition in azobenzene/LC systems [44]. The mesogens and the azo-dyes are depicted as white and black ellipsoids, respectively.	39
3.7	Chemical structure of the photoactive units 4-R-azobenzene (R = H, F, Br, CH ₃ , CF ₃ , OCH ₃ , <i>On</i> -Bu, <i>Ot</i> -Bu) together with the <i>trans-cis</i> photoisomerization scheme.	40
3.8	Typical absorption spectra recorded after different times of UV exposure. Example relative to 5CB doped with 4- <i>Ot</i> -Bu-phenylazobenzene dissolved in cyclohexane (see text for details).	41
3.9	Pictures of 5CB doped with <i>cis</i> 4- <i>On</i> -Bu-phenylazobenzene at 7% mole fraction, taken with the cell between crossed polarizers (see text for details). Bright and dark areas correspond to the nematic and the isotropic phases, respectively. We show the sample at the highest temperature at which it is still completely nematic (a: $T = 286.7\text{ K}$), in the biphasic region (b: $T = 289.8\text{ K}$; c: $T = 290.8\text{ K}$) and at a temperature at which it is completely isotropic (d: $T = 292.2\text{ K}$).	42
3.10	Experimental ESR spectra (dashed line) and fits (solid line) of 5CB doped with <i>cis</i> 4-CH ₃ -phenylazobenzene at 7% mole fraction. For each spectrum, the temperature and the corresponding phases are indicated. For the spectra recorded in the biphasic region the fraction of the nematic phase f_N is also reported.	44
3.11	Temperature-composition phase diagram of 5CB, doped with <i>cis</i> 4- <i>On</i> -Bu-phenylazobenzene, showing the nematic–isotropic coexistence region. Also shown are the experimental ESR spectra, at 7% mole fraction, acquired at the limiting temperatures (T_α and T_β) and approximately in the middle (T_j) of the biphasic region.	45
3.12	Order parameter $\langle P_2 \rangle$ of the spin probe against reduced temperature T^* for the samples doped with the <i>trans</i> azo-derivatives at (a) 1% and (b) 7% mole fraction, compared to the pure 5CB. The sequence of the substituents, from bottom to top in the key, is in order of increasing T_{NI} , as listed also in the arrow-shaped scheme.	47
3.13	Order parameter $\langle P_2 \rangle$ of the spin probe against reduced temperature T^* for the samples doped with the <i>cis</i> azo-derivatives at (a) 1% and (b) 7% mole fraction, compared to the pure 5CB. The sequence of the substituents, from bottom to top in the key, is in order of increasing T_{NI} , as listed also in the arrow-shaped scheme.	48

3.14	Electrostatic potential at the molecular surface for the 5CB (a), <i>trans</i> 4- <i>On</i> -Bu-phenylazobenzene (b), <i>trans</i> azobenzene (c), <i>cis</i> 4-Br-phenylazobenzene (d) and <i>cis</i> 4- <i>Ot</i> -Bu-phenylazobenzene (e). Color coded according to the palette (units $4\pi\epsilon_0e/\text{\AA}$). Geometry and charges obtained at B3LYP/6-31G** – AUG-cc-PVTZ level.	52
3.15	Chemical structure of the disubstituted photoactive units (R = NO ₂ , OCH ₃) together with the <i>trans-cis</i> photoisomerization scheme.	54
3.16	UV-visible absorption spectra for checking both the photoisomerization process before the ESR measurements and the stability of the <i>cis</i> configuration after the ESR measurements. Exemple relative to 5CB doped with AB ₂ OMe (8%) dissolved in cyclohexane.	55
3.17	Temperature-composition phase diagram of 5CB, doped with <i>cis</i> AB ₂ OMe, showing the nematic–isotropic coexistence region.	55
3.18	Order parameter $\langle P_2 \rangle$ of the spin probe against reduced temperature T^* for the samples doped with (a) the <i>trans</i> and (b) the <i>cis</i> azo-derivatives compared to the pure 5CB.	57
3.19	Arrhenius behavior of the tumbling diffusion coefficient $R_{\perp}^{(i)}$ (with $i = N$ or I) in the N and in the I phase (see text for details).	58
3.20	Electrostatic potential at the molecular surface for the 5CB (a), <i>trans</i> AB ₂ OCH ₃ (b), <i>trans</i> AB ₂ NO ₂ (c), <i>cis</i> AB ₂ OCH ₃ (d) and <i>cis</i> AB ₂ NO ₂ (e). Color coded according to the palette (units $4\pi\epsilon_0e/\text{\AA}$). Geometry and charges obtained at B3LYP/6-31G** – AUG-cc-PVTZ level.	60
4.1	Schematic process for the synthesis of hydrophilic and hydrophobic aerosil.	61
4.2	Building principle of the solid network of fumed silica depicting the formation of hydrogen bonds between the aggregates [76].	62
4.3	Fictional three-dimensional framework with nematic domains of randomly oriented director [76].	63
4.4	On scale schematic representation of the aerosil dispersion showing probe molecules (black particles, see inset) dissolved in the liquid crystal local ordered domains (white particles) and the silica network (gray circles).	66
4.5	Typical experimental spectra (dashed lines) and fits (solid lines) of the samples in the nematic (a, b: T=298.2 K) and isotropic (c: T=343.2 K) phase at various R812 aerosil concentration. (a) Monodomain spectra obtained for the pure (“no aerosil”), 0.3, 1 and 3% wt samples after the field cooling (FC) procedure. (b) The 10% sample in the nematic phase was only partially aligned and remained in a polydomain state: sample before the field cooling (ZFC), field cooled sample at the beginning of the heating stage (FC, <i>h</i>) and FC sample after cooling from the I phase (FC, <i>c</i>).	69

4.6	Temperature dependence of the orientational order parameter $\langle P_2 \rangle$ of the spin probe at various aerosil concentrations on heating (h) and on cooling (c); (a) hydrophobic (R812) aerosil, (b) hydrophilic (A380) aerosil.	71
4.7	Temperature dependence of the tumbling diffusion coefficient R_{\perp} of the spin probe at various concentrations of the hydrophobic (R812) aerosil. Data in the isotropic phase (a) obey a simple Arrhenius-type equation (solid lines). (b) Detail of the nematic region shown above. Experimental data points in the vicinity of T_{NI} (above $T = 308.0$ K) have been removed. Solid lines: fit to the Arrhenius equation; dashed lines: fit to the Vogel-Fulcher-Tammann (VFT) equation (see text for details). Best fit values for the activation energy E (Arrhenius fit) or for the B and T_0 parameters (VFT fit) are shown in Table 4.1.	73
4.8	Temperature dependence of the tumbling diffusion coefficient R_{\perp} of the spin probe at various concentrations of the hydrophobic (A380) aerosil. Data in the isotropic phase (a) obey a simple Arrhenius-type equation (solid lines). (b) Detail of the nematic region shown above. Experimental data points in the vicinity of T_{NI} (above $T = 308.0$ K) have been removed. Solid lines: fit to the Arrhenius equation; dashed lines: fit to the Vogel-Fulcher-Tammann (VFT) equation (see text for details). Best fit values for the activation energy E (Arrhenius fit) or for the B and T_0 parameters (VFT fit) are shown in Table 4.1.	75
4.9	Temperature dependence of the spin probe diffusion coefficient ratio $R_r = R_{\parallel}/R_{\perp}$, for all the nematic samples studied, obtained via the globalization scheme described in the text.	77
4.10	Temperature dependence of the spin probe diffusion coefficient R_{\parallel} of the spin probe for all the nematic samples studied.	78
5.1	Schematic of grating structure consisting of polymer planes and LC nano-droplets. (a) In the field-off state the directors (arrows) are randomly oriented and this results into a periodic refractive index profile in the vertical direction. (b) When an electric field is applied along the grating vector, all the directors align causing a disappearance of the refractive index profile [98].	83
5.2	(a) Experimental set up used for recording the transmission holographic grating. (b) Illustration of the diffusion process occurring when the HPDLC cell is illuminated with an interference pattern.	84
5.3	Experimental ESR spectra (dashed line) and fits (solid line) of the HPDLC sample. For each spectrum, the temperature and the corresponding phase are indicated.	86
5.4	Local order parameter $\langle P_2 \rangle$ against reduced temperature T^* of BL038 LC inside the nano-droplets of the HPDLC sample (open squares) and in the bulk (filled squares).	87
5.5	Temperature dependence of the spin probe diffusion coefficient R_{\perp} in the HPDLC sample (open squares) and in the bulk.	88

LIST OF FIGURES

97

A.1 Euler angles representation. 90

List of Tables

2.1	Magnetic parameters for a nitroxide free radical.	20
2.2	Magnetic parameters for the CSL nitroxide radical.	31
3.1	Effect of the <i>trans</i> and <i>cis</i> <i>p</i> -azobenzene derivatives at 1% and 7% mole fraction on the nematic phase stability ^a	46
3.2	Dipole moment (μ) and dipole components (μ_i) of the various molec- ular species used in this study ^a	50
3.3	Quadrupole components Q_{ii} of the various molecules used in this study ^a	50
3.4	Effect of the <i>trans</i> and <i>cis</i> <i>p-p'</i> azobenzene derivatives at 3% and 8% mole fraction on the nematic phase stability ^a	56
3.5	Dipole moment (μ) and dipole components (μ_i) of the various molec- ular species used in this study ^a	60
3.6	Quadrupole components Q_{ii} of the various molecules used in this study ^a	60
4.1	Best fit values of the activation energy E (Arrhenius model) and of the parameters B and T_0 (VogelFulcherTammann model) obtained from the analysis of the temperature dependence of the tumbling diffusion coefficient R_{\perp} (see text for details).	76
5.1	Chemical composition of the homogeneous mixture used to prepare the HPDLC films.	85

Bibliography

- [1] de Gennes, P. G.; Prost, J. *The Physics of Liquid Crystals*; Clarendon Press: Oxford, 1993.
- [2] Chandrasekhar, S. *Liquid Crystals, 2nd edition*; Cambridge University Press: Cambridge, 1992.
- [3] Vertogen, G.; de Jeu, W. H. *Thermotropic Liquid Crystals, Fundamentals*; Springer-Verlag: Berlin Heidelberg, 1988.
- [4] Rose, M. E. *Elementary Theory of Angular Momentum*; Wiley, 1957.
- [5] Bersohn, M.; Baird, J. C. *An Introduction to Electron Paramagnetic Resonance*; W. A. Benjamin, Inc.: New York, 1966.
- [6] Nordio, P. L. In *Spin Labeling. Theory and Applications*; Academic Press: New York, 1976; chapter 1.
- [7] Meier, G.; Sackman, E.; Grabmaier, J. G. *Applications of Liquid Crystals*; Springer-Verlag: Berlin Heidelberg, 1975.
- [8] Yamada, B.; Westmoreland, D. G.; Kobatake, S.; Konosu, O. *Prog. Polym. Sci.* **1999**, *24*, 565.
- [9] Veregin, R. P. N.; Georges, M. K.; Kazmaier, P. M.; Hamer, G. K. *Macromolecules* **1993**, *26*, 5316.
- [10] Asano-Someda, M.; Ichino, T.; Kaizu, Y. *J. Phys. Chem. A* **1997**, *101*, 4484.
- [11] Morrisett, J. D. In *Spin Labeling. Theory and Applications*; Academic Press: New York, 1976; chapter 8.
- [12] Smith, I. C. P.; Butler, K. W. In *Spin Labeling. Theory and Applications*; Academic Press: New York, 1976; chapter 11.
- [13] Seeling, J. In *Spin Labeling. Theory and Applications*; Academic Press: New York, 1976; chapter 10.
- [14] Berliner, L. J. *Spin Labeling. Theory and Applications*; Academic Press: New York, 1976.

- [15] Kutsumizu, S.; Schlick, S. *J. Mol. Struct.* **2005**, *739*, 191.
- [16] Frezzato, D.; Kothe, G.; Moro, G. J. *J. Phys. Chem. B* **2004**, *108*, 9505.
- [17] Mangels, M. L.; Cardon, T. H.; Harper, A. C.; Howard, K. P.; Lorigan, G. A. *J. Am. Chem. Soc.* **2000**, *122*, 7052.
- [18] Liang, A.; Freed, J. H. *J. Phys. Chem. B* **1999**, *103*, 6384.
- [19] Ionescu, D.; Luckhurst, G. R.; Silva, D. S. D. *Liq. Cryst.* **1997**, *6*, 833.
- [20] Freed, J. H. In *Spin Labeling. Theory and Applications*; Academic Press: New York, 1976; chapter 3.
- [21] Freed, J. H.; Nayeem, A.; Rananavare, S. B. In *The Molecular Dynamics of Liquid Crystals*; Kluwer Academic Publishers: Dordrecht, 1994; chapter 15.
- [22] Freed, J. H.; Bruno, G. V.; Polnaszek, C. F. *J. Phys. Chem.* **1971**, *75*, 3385.
- [23] Freed, J. H. *J. Chem. Phys.* **1964**, *41*, 2077.
- [24] Vecchi, I.; Arcioni, A.; Bacchiocchi, C.; Tiberio, G.; Zanirato, P.; Zannoni, C. *Mol. Cryst. Liq. Cryst.* **2007**, *465*, 271.
- [25] Vecchi, I.; Arcioni, A.; Bacchiocchi, C.; Tiberio, G.; Zanirato, P.; Zannoni, C. *J. Phys. Chem. B* **2007** (*In Press*).
- [26] Arcioni, A.; Bacchiocchi, C.; Vecchi, I.; Zannoni, C. *Mol. Cryst. Liq. Cryst.* **2005**, *429*, 213.
- [27] Arcioni, A.; Bacchiocchi, C.; Vecchi, I.; Venditti, G.; Zannoni, C. *Chem. Phys. Lett.* **2004**, *396*, 433.
- [28] Meirovitch, E.; Freed, J. H. *J. Phys. Chem.* **1984**, *88*, 4995.
- [29] Rao, K. V. S.; Polnaszek, C. F.; Freed, J. H. *J. Phys. Chem.* **1977**, *81*, 449.
- [30] Carr, S. G.; Khoo, S. K.; Luckhurst, G. R.; Zannoni, C. *Mol. Cryst. Liq. Cryst.* **1976**, *35*, 7.
- [31] Freed, J. H. In *Electron Spin Relaxation in Liquids*; Plenum Press: New York, 1972; chapter 14.
- [32] Schneider, D. J.; Freed, J. H. In *Biological Magnetic Resonance. Spin Labeling*; Plenum Press: New York, 1989; chapter 1.
- [33] Zannoni, C.; Pedulli, G. F.; Masotti, L.; Spisni, A. *J. Magn. Reson.* **1981**, *43*, 141.
- [34] Arcioni, A.; Tarroni, R.; Zannoni, C. *J. Chem. Soc. Faraday Trans.* **1993**, *89*, 2815.

- [35] Bevington, P. R. *Data Reduction and Error Analysis for the Physical Sciences*; McGraw-Hill: New York, 1969.
- [36] Rau, H. In *Photochemistry and Photophysics*; CRC Press: Boca Raton, 1990; Vol. 2; chapter 4.
- [37] Crecca, C. R.; Roitberg, A. E. *J. Phys. Chem. A* **2006**, *110*, 8188.
- [38] Chang, C. W.; Lu, Y.-C.; Wang, T. T.; Diao, E. W. G. *J. Am. Chem. Soc.* **2004**, *126*, 10109.
- [39] Ciminelli, C.; Granucci, G.; Persico, M. *Chem. Eur. J.* **2004**, *10*, 2327.
- [40] Cembran, A.; Bernardi, F.; Garavelli, M.; Gagliardi, L.; Orlandi, G. *J. Am. Chem. Soc.* **2004**, *126*, 3234.
- [41] Cattaneo, P.; Persico, M. *Phys. Chem. Chem. Phys.* **1999**, *1*, 4739.
- [42] Hubert, C.; Rumyantseva, A.; Lerondel, G.; Grand, J.; Kostcheev, S.; Billot, L.; Vial, A.; Bachelot, R.; Royer, P.; Chang, S. H.; Gray, S. K.; Wiederrecht, G. P.; Schatz, G. C. *Nanoletters* **2005**, *5*, 615.
- [43] Yu, Y.; Nakano, M.; Ikeda, T. *Nature* **2003**, *425*, 145.
- [44] Ikeda, T. *J. Mater. Chem.* **2003**, *13*, 2037.
- [45] Finkelmann, H.; Nishikawa, E.; Pereira, G.; Warner, M. *Phys. Rev. Lett.* **2001**, *87*, 015501(4).
- [46] Ichimura, K. *Chem. Rev.* **2000**, *100*, 1847.
- [47] Tsutsumi, O.; Shiono, T.; Ikeda, T.; Galli, G. *J. Phys. Chem. B* **1997**, *101*, 1332.
- [48] Ikeda, T. *Mol. Cryst. Liq. Cryst.* **2001**, *364*, 187.
- [49] Ikeda, T.; Kanazawa, A. *Bull. Chem. Soc. Jpn.* **2000**, *73*, 1715.
- [50] Kurihara, S.; Nomiyama, S.; Nonaka, T. *Chem. Mater.* **2000**, *12*, 9.
- [51] Schadt, M.; Mueller, F. *J. Chem. Phys.* **1976**, *65*, 2224.
- [52] DasGupta, S.; Chattopadhyay, P.; Roy, S. K. *Phys. Rev. E* **2001**, *63*, 041703/1.
- [53] Syvitski, R. T.; Pau, M.; Burnell, E. E. *J. Chem. Phys.* **2002**, *117*, 376.
- [54] Martire, D. E. In *The Molecular Physics of Liquid Crystals*; Academic Press: London, 1979.
- [55] Sigaud, G.; Achard, M. F.; Hardouin, H.; Gasparoux, H. *Chem. Phys. Lett.* **1977**, *48*, 122.

- [56] Burnell, E. E.; de Lange, C. A. *Chem. Rev.* **1998**, *98*, 2359.
- [57] Boyer, J. In *The Chemistry of the Nitro and Nitroso Groups*; Interscience: New York, 1969.
- [58] Humphries, R. L.; Luckhurst, G. R. *Proc. R. Soc. London Ser. A* **1976**, *352*, 41.
- [59] Martire, D. E.; Oweimreen, G.; Agren, G.; Ryan, S.; Peterson, H. *J. Chem. Phys.* **1976**, *64*, 1456.
- [60] Oweimreen, G. *J. Phys. Chem. B* **2001**, *105*, 8410.
- [61] Arcioni, A.; Bacchiocchi, C.; Grossi, L.; Nicolini, A.; Zannoni, C. *J. Phys. Chem. B* **2002**, *106*, 9245.
- [62] Polson, J. M.; Burnell, E. E. *Chem. Phys. Lett.* **1997**, *281*, 207.
- [63] Beckmann, P. A.; Emsley, J. W.; Luckhurst, G. R.; Turner, D. L. *Mol. Phys.* **1986**, *59*, 97.
- [64] Syvitski, R. T.; Pau, M.; Burnell, E. E. *J. Chem. Phys.* **2000**, *113*, 3452.
- [65] Dingemans, T.; Photinos, D. J.; Samulski, E. T.; Terzis, A. F.; Wutz, C. *J. Chem. Phys.* **2003**, *118*, 7046.
- [66] Syvitski, R. T.; Pau, M.; Burnell, E. E. *Chem. Phys. Lett.* **1997**, *281*, 199.
- [67] Cornell, W. D.; Cieplak, P.; Bayly, C. I.; Gould, I. R.; Merz, J. K.; Ferguson, D. M.; Spellmeyer, D. C.; Fox, T.; Caldwell, J. W.; Kollman, P. A. *J. Am. Chem. Soc.* **1995**, *117*, 5179.
- [68] Berardi, R.; Muccioli, L.; Orlandi, S.; Ricci, M.; Zannoni, C. *Chem. Phys. Lett.* **2004**, *389*, 373.
- [69] Stone, P. J. W.; Miller, L. S.; Sethi, R. S. *Royal. Soc. Chem.* **1993**, *137*, 88.
- [70] Lee, R. H.; Hsiue, G. H.; Jeng, R. J. *J. Polym. Res.* **1998**, *5*, 37.
- [71] Sung, J. H.; Hirano, S.; Tsutsumi, O.; Kanazawa, A.; Shiono, T.; Ikeda, T. *Chem. Mater.* **2002**, *14*, 385.
- [72] Zalar, B.; Lavrentovich, O. D.; Zeng, H.; Finotello, D. *Phys. Rev. E* **2000**, *62*, 2252.
- [73] Nair, G. G.; Prasad, S. K.; Yelamaggad, C. V. *J. Appl. Phys.* **2000**, *87*, 2084.
- [74] Legge, C. H.; Mitchell, G. R. *J. Phys. D: Appl. Phys.* **1991**, *25*, 492.
- [75] Berardi, R.; Muccioli, L.; Zannoni, C. *Chem. Phys. Chem.* **2004**, *5*, 104.

- [76] Kreuzer, M.; Eidenschink, R. In *Liquid Crystals in Complex Geometries*; Talyor and Francis: London, 1996.
- [77] Kreuzer, M.; Tschudi, T.; Eidenschink, R. *Mol. Cryst. Liq. Cryst.* **1992**, *223*, 219.
- [78] Kreuzer, M.; Tschudi, T.; de Jeu, W. H.; Eidenschink, R. *Appl. Phys. Lett.* **1993**, *62*, 1712.
- [79] Eidenschink, R.; de Jeu, W. H. *Electron. Lett.* **1991**, *27*, 1195.
- [80] Aliev, F. M.; Shina, G. P.; Kreuzer, M. *Mol. Cryst. Liq. Cryst.* **2001**, *359*, 217.
- [81] Glushchenko, A.; Kresse, H.; Reshetnyak, V.; Reznikov, Y.; Yaroshchuk, O. *Liq. Cryst.* **1997**, *23*, 241.
- [82] Aliev, F. M.; Shina, G. P. *Mol. Cryst. Liq. Cryst.* **2001**, *364*, 435.
- [83] Bellini, T.; Buscaglia, M.; Chiccoli, C.; Mantegazza, F.; Pasini, P.; Zannoni, C. *Phys. Rev. Lett.* **2002**, *88*, 245506.
- [84] Iannacchione, G. S.; Garland, C. W.; Mang, J. T.; Rieker, T. P. *Phys. Rev. E* **1998**, *58*, 5966.
- [85] Haga, H.; Garland, C. W. *Phys. Rev. E* **1997**, *56*, 3044.
- [86] Bender, M.; Holstein, P.; Geschke, D. *Liq. Cryst.* **2001**, *28*, 1813.
- [87] Canlet, C.; Fung, B. M. *Liq. Cryst.* **2001**, *28*, 1863.
- [88] Sun, H.; Roth, M. D.; Fung, B. M. *Liq. Cryst.* **2001**, *28*, 1469.
- [89] Marinelli, M.; Mercuri, F.; Zammit, U.; Scudieri, F. *Phys. Rev. E* **1998**, *58*, 5860.
- [90] Marinelli, M.; Ghosh, A. K.; Mercuri, F. *Phys. Rev. E* **2001**, *63*, 061713.
- [91] Mercuri, F.; Ghosh, A. K.; Marinelli, M. *Phys. Rev. E* **1999**, *60*, 6309.
- [92] Jin, T.; Finotello, D. *Phys. Rev. E* **2004**, *69*, 041704.
- [93] Jin, T.; Finotello, D. *Phys. Rev. Lett.* **2001**, *86*, 818.
- [94] Sastry, S. *Nature* **2001**, *409*, 164.
- [95] Ewiss, M. A. Z.; Nabil, G.; Stoll, B.; Herminghaus, S. *Liq. Cryst.* **2003**, *30*, 1241.
- [96] Hourri, A.; Bose, J.; Thoen, J. *Phys. Rev. E* **2001**, *63*, 051702.

- [97] Crawford, G. P.; Zumer, S. *Liquid Crystals in Complex Geometries*; Talyor and Francis: London, 1996.
- [98] Bunning, T. J.; Natarajan, L. V.; Tondiglia, V. P.; Sutherland, R. L. *Annu. Rev. Mater. Sci.* **2000**, *30*, 83.
- [99] Jung, J. A.; Kim, B. K. *Optics Communications* **2005**, *247*, 125.
- [100] Klosterman, J.; Natarajan, L. V.; Tondiglia, V. P.; Sutherland, R. L.; White, T. J.; Guymon, C. A.; Bunning, T. J. *Polymer* **2004**, *45*, 7213.
- [101] Liu, Y. J.; Jia, B. Z. Y.; Xu, K. S. *Optics Communications* **2003**, *218*, 27.
- [102] Duca, D.; Sukhov, A. V.; Umeton, C. *Liq. Cryst.* **1999**, *26*, 931.
- [103] Caputo, R.; Sukhov, A. V.; Tabiryan, N. V.; Umeton, C. *Chem. Phys.* **1999**, *245*, 463.
- [104] DeRosa, M. E.; Tondiglia, V. P.; Natarajan, L. V. *J. Appl. Polym. Sci.* **1998**, *68*, 523.
- [105] Pogue, R. T.; Natarajan, L. V.; Siwecki, S. A.; Tondiglia, V. P.; Sutherland, R. L.; Bunning, T. J. *Polym. Sci. Polym. Phys.* **2000**, *41*, 733.
- [106] Bunning, T. J.; Natarajan, L. V.; Tondiglia, V. P.; Dougherty, G.; Sutherland, R. L. *Polym. Sci. Polym. Phys.* **1997**, *35*, 2825.
- [107] Bunning, T. J.; Natarajan, L. V.; Sutherland, R. L.; Vezie, D. L.; Adams, W. W. *Polymer* **1995**, *36*, 2699.
- [108] Iannacchione, G. S.; Finotello, D.; Natarajan, L. V.; Sutherland, R. L.; Tondiglia, V. P.; Bunning, T. J.; Adams, W. W. *Europhys. Lett.* **1996**, *36*, 425.
- [109] Vilfan, M.; Zalar, B.; Fontecchio, A. K.; Vilfan, M.; Escuti, M. J.; Crawford, G. P.; Zumer, S. *Phys. Rev. E* **2002**, *66*, 1710.
- [110] Ramlall, P.; McClelland, R. *J. Chem. Soc. Perkin Trans. 2* **1999**, page 225.